VIBRATIONAL PROPERTIES AND PHASE STABILITY OF DISORDERED ALLOY

THESIS SUBMITTED FOR THE DEGREE OF

DOCTOR OF PHILOSOPHY (SCIENCE)

IN

PHYSICS

BY

RAJIV KUMAR CHOUHAN

DEPARTMENT OF PHYSICS

UNIVERSITY OF CALCUTTA

APRIL, 2013

To my father (love you papa).....

ACKNOWLEDGMENTS

The first person I want to gratefully acknowledge is Prof. Abhijit Mookerjee. I have been under his guidance since my M.Sc days and he consistently guided me to carry on the research so smoothly. His patience care and insight of various problem made it possible for me to carry out and complete the investigation. He gave me enough freedom in thinking and choosing my own problems during my research carrier. Whenever I had a problem without any hesitation I went him and he make me understand the topic crystal clear. He is the one who is more than a supervisor to me a friend, a colleague in my life.

I am glad to thank Dr. Subhradip Ghosh of Indian Institute of Technology, Guwahati, Assam for helpful discussion in the beginning of my Ph.D. I am thankful to Dr. Aftab Alam (now at Ames Laboratory, Iowa, USA) with whom I did major of my work. He was the person with who I discussed much and he never said no to my stupid questions. I would also like to thanks Dr. Alfè of University College London (UK), who make my doubts clear during my phonon study using *small displacement method*. My discussions with Dr. Bipul Raskit and Dr. Biswanath Dutta were always helpful and pleasant.

I would like to thanks S.N. Bose centre for providing the research fellowship and facilities without which it was impossible for me to carry my research. I would like to thank Department of Science and Technology (DST) for providing me financial support during my visit to Universit du Qubec Chicoutimi for conference 31st ITCC and 19th ITES (2011).

I must thank to our Hydra group members Shreemoyee di and Mitali di (senior

cum elder sister), Rudra da, Moshiur da, Mukul da, Manoj da, Soumendu da, Kartick da, Prashant and Jena (with whom I have lots of valuable discussion) and Tanmoy who made the working environment vibrant and cheerful.

S.N. Bose Centre was like my second home where I did my Integrated Ph.D and few of my seniors and friends have akin to family members during my stay; specially Abhinav bhaiya (elder brother) with whom I shared lots of moments. Niraj bhaiya, Debraj and Garain were very supportive and close to me. Seniors (Navin bhaiya, Abhishek bhaiya, Venkat da, Hemant bhaiya, Shailesh bhaiya, Roby da, Vikas bhaiya, and Manish bhaiya), friends (Chinmay, Majhi, Sujoy, Somyajit, Kapil, Hirak, Abhijit, Sumit and Bisu) made my stay cheerful. I was always being a kind of perturbation between Agarwal and Singh and three of us together were the leg pulling group within ourselves. Wasim, Rajasree, Manish, Shailesh, and Kamal were always a good friend of mine. Juniors (Saikat, Ruma D., Ruma M., Ashu, Pandey, Basu, Himani, Vineeta) were very kind and cheerful specially Tukun, Debolina and friends of GD (Priya and others).

My sincerest thanks to my parents and specially to my father who is no more. He was the person who believed first my dreams before me. He always encouraged me whenever I got diverted from my goal. Finally I thank to my brother (Amit) who consistently encourages me to achieve my destination.

Rajiv Kumar Chouhan

S.N.Bose National Centre for Basic Sciences,

Kolkata, India.

Publications

1. **Ab-initio study of the phonon spectrum, entropy and lattice heat capacity of disordered Re-W alloys**

   Rajiv Kumar Chouhan, Aftab Alam, Subhradip Ghosh and Abhijit Mookerjee

   J. Phys.: Condens. Matter **24** 375401 (2012).

2. **Thermal conductivity and diffusion-mediated localization in $Fe_{1-x}Cr_x$ alloys**

   Aftab Alam, Rajiv K. Chouhan and Abhijit Mookerjee

   Phys. Rev. **B 84**,224309 (2011).

3. **Phonon modes and vibrational entropy of disordered alloys with short-range order: A first principles calculation**

   Aftab Alam, Rajiv Kumar Chouhan, and Abhijit Mookerjee

   Phys. Rev. **B 83**, 054201 (2011).

4. **Magnetic phase stability of CuMn**

   Rajiv Kumar Chouhan, Abhijit Mookerjee

   J. Magn. Magn. Mater., **323**, 868-873 (2011).

5. **Lattice Thermal Properties of Disordered Alloys: A Theoretical Approach**

   Rajiv Kumar Chouhan, Aftab Alam and Abhijit Mookerjee

   Conference Proceedings of the 31st ITCC and 19th ITES (2011) (*in press*)

6. **Interplay of force constants in the lattice dynamics of disordered alloys : An ab-initio study**

   Rajiv K. Chouhan, Aftab Alam and Abhijit Mookerjee

   manuscript under preparation

Contents

List of Figures

List of Tables

Chapter 1

Introduction and Overview

The content of this thesis is focused on two aspects of disordered alloys: Vibrational (phononic) properties and magnetic phase transition study. In our day today life we come across disordered systems like glass, amorphous silicon, brass (Cu-Zn) jewellery (i.e. alloys like Au-Cu, Au-Ag) so on. By introducing randomness we may tune the physical and chemical properties (like ductility, tensile strength, elasticity etc) of materials. The study of the electronic and vibrational (phononic) properties is the key to the understanding of the behavior of such systems. Recent advance in technology gives us a insight into the physical and chemical properties of these materials, so the onus lies on us theoretician to formulate theories to understand and predict experimental behavior.

Disorder in alloys may be of various types like, topological, substitutional, interstitial and so on. However, in this work we shall confine ourselves to substitutional disorder. This type of disordered alloys have underlying lattice structure but each lattice point is occupied randomly by the constituent atoms as shown in schematic diagram (Fig. 1.1). Thus conventional lattice translational symmetry breaks down.

Few mean-field theories [1, 2, 3] were proposed to overcome this problem. In these

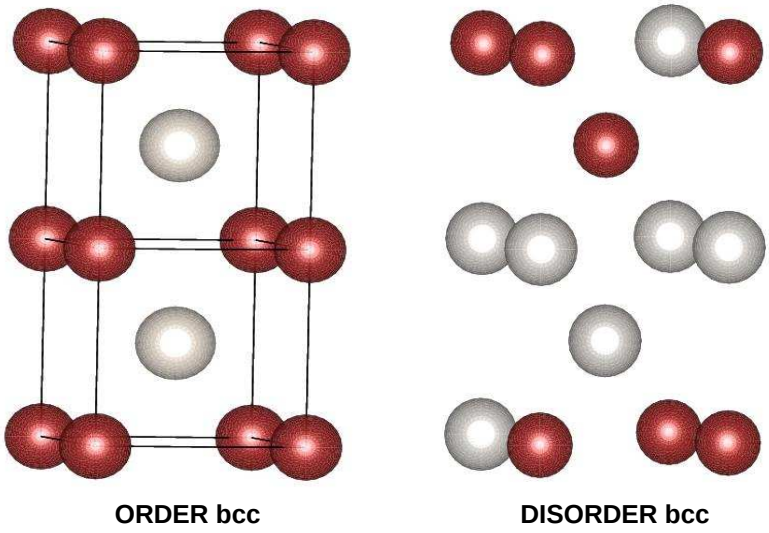

Figure 1.1: Schematic diagram of bcc (left) ordered and (right) substitutional disordered structure.

approaches, the disordered system is replaced by a lattice periodic effective medium, with effective atoms occupying lattice sites. Coherent potential approximation (CPA) [5] emerged as most successful mean-field approximation, however when environment effects become important: like short ranged ordering (SRO), chemical affinity driven local clustering it fails. Although further generalization of CPA [6] exists in the literature, most of these are limited to either very special type of off-diagonal disorder, or violated the lattice translational symmetry and Herglotz analytic properties of the configuration averaged Green function. Out of various such methods, one approach emerged out to be somewhat promising namely the non-local coherent potential approximation (NL-CPA) [7] & [8]. As CPA is averaging technique so it is impossible to implement structure relaxation, which contrasts with the experimental observations because bond distance between atomic pairs (e.g. A-A, B-B and A-B in a binary al-

loy) are generally different. Another method proposed by Zunger *et.al.*[9] the Special Quasi-random Structure (SQS), in which the distribution of distinct local environments (e.g. A or B surrounded by the various A_mB_{8-m} coordination shells with m between 0 to 8 in body-centered cubic (bcc) $A_{1-x}B_x$ alloys) is maintained. In particular SQS is an ordered super-cell which is constructed in such a way to mimic the most relevant pair and multi-site correlation functions of the disordered phase. The above mentioned approximation by mean-field theories is overcome by Augmented Space Recursion (ASR) introduced by Mookerjee (1973)[10]. ASR is one of the powerful tool available to deal with substitutional disorder. It goes beyond standard mean-field approximation to consider randomness not only at onsite but also in its nearest neighborhood. In Chapter 4, we integrate a first-principles SQS method with the augmented space formalism to demonstrate the interplay of force constants within a disorder environment.

We will focus our study to binary disordered alloys. For the study of lattice vibrational properties of disordered alloys, when two constituent atoms in a substitutional alloy have different masses and force constant matrices then there are in general three sources of disorder : (a) diagonal disorder, arising from the mass difference $m_A - m_B$; (b) off-diagonal ϕ_{ij} (where j is a neighboring site of i) which can take values ϕ_{ij}^{AA}, ϕ_{ij}^{AB} or ϕ_{ij}^{BB}; and (c) environmental disorder at a site which arises from the sum rule $\phi_{ii} = -\sum \phi_{ij}$. The problem becomes even more complicated if we look into the short-range features of atomic arrangements. We have carried out a detailed first-principles study for the short-range ordering (or local atomic configuration), thermal transport properties, and vibrational entropy of several alloy systems.

Another important physical property we studied is the Phase stability. Here the disorder depends on the potential difference between the constituent ion-cores: $V_A -$

V_B. To study magnetic phase we obtained the pair energy for different compositions using orbital peeling technique of Burke[11], based on tight-binding linear muffin-tin orbital and Augmented space recusrion.

1.1 Overview of lattice dynamics

Starting with the many-body Hamiltonian, let us consider a system consisting of N_c ion cores in a solid having N_e valence electrons

$$H = \sum_{k=1}^{N_c} \frac{{P_k}^2}{2M_k} + \sum_{l=1}^{N_e} \frac{{p_l}^2}{2m_l} + V_{ee}(\vec{r}) + V_{ei}(\vec{r}, \vec{R}) + V_{ii}(\vec{R}) \tag{1.1}$$

where P_k, M_k and p_l, m_l are momentum and masses of ions and electrons. While V_{ee}, V_{ii}, and V_{ee} are electron-electron, ion-ion and electron-ion interactions. Equation 1.1 can be rewritten as

$$H = H_e + H_i + H_{ei}$$

Now we focus on the ionic motion part of Hamiltonian (H), and use the Born-Oppenheimer (adiabatic) approximation to reduce the electronic Hamiltonian to one electron Hamiltonian. According to Born-Oppenheimer approximation massive ions are assumed to be frozen or stationary compare to dynamical movement of electrons. After a tedious implementation of the Born-Oppenheimer approximation, the ion-Hamiltonian becomes

$$H_i \cong \sum_k \frac{{P_k}^2}{2M_k} + E_{eff}(R_1, R_2, ..., R_n) \tag{1.2}$$

where E_{eff} = average total energy for all ions at positions R_k. E_{eff} acts as an effective potential energy for the ion motion. Since E_{eff} depends on the electronic states of all electron and position of all ions, hence one has to perform electronic calculation

to calculate E_{eff} with high degree of accuracy (as function of R_k).

Now as a result of thermal fluctuation at finite temperature, the constituent atoms in a crystal lattice oscillates about its equilibrium positions. Let the displaced position of each vibrating ion is

$$R_k = R_{k_0} + \delta R_k$$

where R_{k_0} is equilibrium ion position and δR_k is vibrational displacement amplitude. Expanding E_{eff} in eq. 1.2 in a Taylor's series about R_{k_0},

$$E_{eff}(R_k) = E_{eff}(R_{j_0}) + E'(\delta R_j)$$

Expanding $E'(\delta R_j)$ for small δR_j, the first-order term canceled (i.e. $\frac{\partial E_e}{\partial R_k} = 0$). Neglecting the higher terms of expansion expression for effective potential will looks like

$$E_{eff}(R_k) = E_{eff}(R_{j_0}) + \frac{1}{2}\sum_{kl}\sum_{\mu\nu}\frac{\partial^2 E_{eff}}{\partial u_\mu(R_k)\partial u_\nu(R_l)}u_\mu(R_k)u_\nu(R_l) \tag{1.3}$$

The above eqn. 1.3 is known as harmonic approximation and now the equation of motion takes the form

$$M_k\ddot{u}_\mu(R_k) = -\frac{\partial E_{eff}}{\partial u_\mu(R_k)} = \sum_{k\nu}\Phi_{\mu\nu}^{R_k R_l}u_\nu(R_l) \tag{1.4}$$

where $\Phi_{\mu\nu}^{R_k R_l}$ are the force constant having expression,

$$\Phi_{\mu\nu}^{R_k R_l} = -\frac{\partial^2 E_{eff}}{\partial u_\mu(R_k)\partial u_\nu(R_l)}$$

Now let us choose an oscillatory solution of eqn. (1.4) as:

$$u(R,t) = \frac{1}{\sqrt{N}}e^{i(\mathbf{k}.\mathbf{R}-\omega t)}\epsilon$$

which leads to the equation

$$[M\omega^2 - D(\mathbf{k})]\epsilon = 0 \tag{1.5}$$

where D is dynamical matrix (Hermitian) whose elements are

$$D_{\mu\nu}(\mathbf{k}) = \sum_{R} \Phi_{\mu\nu}^{R_k R_l} e^{i\mathbf{k}.\mathbf{R}}$$

Eqn.1.5 represents three linear homogeneous equations for three unknown $\epsilon_\nu(\nu = 1, 2, 3)$. The three solutions $\omega_p(\mathbf{k})$ (p=1,2,3) for each value of $\mathbf{k}$ are obtained by finding roots of the secular equation $det(M\omega^2 - D) = 0$. The relation between the frequency ω and the wave-vector k gives the dispersion relation.

The basic problem in phonon theory is to solve the secular eqn. (1.5). To do so we use Green's function technique followed by recursion method of Haydock *et.al.*[12]. The Green's function corresponding to the displaced vector ϵ is given as

$$G_{ss}(\mathbf{k}, \omega^2) =< s|(\omega^2 I - A(\mathbf{k}))^{-1}|s > \tag{1.6}$$

with $A(\mathbf{k}) = M^{-\frac{1}{2}} D(\mathbf{k}) M^{-\frac{1}{2}}$, where M and $D(\mathbf{k})$ are Mass operator and dynamical matrix. Tight binding representation having projection operator $P(k)$ and transfer operator $T_{kl}$of above is

$$\begin{aligned} M &= \sum_k m_k \delta_{\mu\nu} P_k \\ D &= \sum_k D^{\mu\nu}_{R_k R_k} P_k + \sum_{kl} D^{\mu\nu}_{R_k R_l} T_{R_k R_l} \end{aligned} \tag{1.7}$$

Imaginary part of Green's function $G_{ss}(\mathbf{k}, \omega^2)$ gives us the spectral function. Dispersion relation are the peaks of spectral function for each wave-vector $\mathbf{k}$ along particular symmetry direction

1.2 Disorder handling techniques

For disordered medium Green's function $\langle\langle G(\mathbf{k}, \omega^2)\rangle\rangle$ is configuration averaged quantity. Very few methods can deal with such kind of disorder. As already mentioned

in beginning of this chapter, CPA and other mean-field methods cannot take care of environmental and nearest neighbor effect, which is clear from eqn. (1.4) and (1.5). To overcome this we carried out Augmented space recursion (ASR) and Special quasi-random structure(SQS) based method.

1.2.1 Augmented space recursion

We will start with the concept of Augmented space theorem proposed by Mookerjee(1973) [10]. The theorem states that "To each variable t_R there is associated configuration space $\emptyset$ spanned by the states $|k\rangle$ of realization of t_R and self adjoint operator T_R " such that probability density

$$P_R(t_R) = -\frac{1}{\pi} Im\langle\emptyset|(t_R + i\delta)I - T_R)^{-1}|\emptyset\rangle \tag{1.8}$$

then the average of any functions of the set of random variables $\{t_{R_i}\}$ is

$$\langle\langle f(t_R)\rangle\rangle = \langle\emptyset|\hat{f}(\hat{T}_R)|\emptyset\rangle \tag{1.9}$$

The product space Φ contains information about all possible configuration of the disordered system. Operator $\hat{T}_R$ is built up from the operator T_R as

$$\hat{T}_R = I \otimes I \otimes I \otimes ..... \otimes T_R \otimes I \otimes .. \tag{1.10}$$

This is known as the Augmented space theorem. Suppose if one wants to carry out the configuration averaging of the phonon Green's function

$$G_{RR}(\omega^2, t_R) = \langle R|(M(T_R)\omega^2 - D(\{t_R\}))^{-1}|R\rangle \tag{1.11}$$

The theorem says

$$\langle\langle G_{RR}(\omega^2)\rangle\rangle = \langle R \otimes \{\emptyset\}|(\hat{M}(\{T_R\})\omega^2 - \hat{D}(\{T_R\}))^{-1}|R \otimes \{\emptyset\}\rangle \tag{1.12}$$

where $\hat{M}(\{T_R\})$, and $\hat{D}(\{T_R\})$ are the operators having a functional form same as that of $M(\{t_R\})$ and $D(\{t_R\})$. The operation in the right hand side of eqn. 1.12 have no randomness and hence can be evaluated easily.

The power of the theorem is now apparent. The average is seen to be a particular matrix element of the Green's function of an augmented Hamiltonian. This is constructed out of the original random Hamiltonian by replacing the random variables by the corresponding configuration space operators built out of their probability distribution. The augmented Hamiltonian is an operator in the augmented space $\Psi = H \otimes \Phi$, when H is the space spanned by the tight binding basis and Φ the full configuration space. The result is exact. Approximation now can be introduced in the actual calculation of this matrix element in a controlled manner. The augmented Hamiltonian has no randomness in it and therefore various techniques are available for the calculation of the Green's function for non-random system. In particular we have used recursion method by Haydock[12] which suited well to obtain matrix elements in augmented space.

1.2.2 Special quasi-random Structure

The core problem of the phonon calculation is extraction of dynamical matrix elements. For disorder case the dynamical matrices are not symmetric and hence it is always a tedious task to get it theoretically. One has to depend fully on neutron scattering experiment data of the system. To overcome this situation we carry out the special quasi-random structure (SQS) based calculation. The advantage of SQS over normal mean-field techniques are that the distribution of distinct local environment (i.e. nearest neighbor) is maintained.

SQS is based on a design "Special N-atom periodic structure" S whose distinct cor-

relation functions $\bar{\Pi}_{k,m}(S)$ best match the ensemble average $\langle \Pi_{k,m} \rangle_R$ of random alloy. For configurational disordered alloy $A_x B_{1-x}$ there is no correlation in the occupation between various sites, which leads to the correlation function $\bar{\Pi}_{k,m}$ to be a product of the lattice-average site variable, relating to the composition by $\langle S_i \rangle = (2x-1)$. Thus in random alloy, the pair and multi-site correlation function takes a simple form

$$\langle \bar{\Pi}_{k,m} \rangle_R = (2x-1)^k \tag{1.13}$$

The SQS approach is computationally expensive to find the small unit cell ordered structure with

$$(\Pi_{k,m})_{SQS} \cong \langle \bar{\Pi}_{k,m} \rangle_R \tag{1.14}$$

An attempt to describe the random alloy by small unit cell periodically repeated structure gives rise to enormous correlation beyond certain distance, hence one should take only the nearest neighbor interaction.

1.3 Some important quantities

One of the most important observable quantity in our method is the configuration averaged Green's function $\langle\langle G(\mathbf{k}, \omega^2) \rangle\rangle$ for the disordered medium. Recursion method of Haydock *et.al.*[12] is one of key technique that has been used to calculate $\langle\langle G \rangle\rangle$. Unlike the ordinary recursion for simple tight binding Hamiltonian [12], we, in ASR, recurse in the space of all possible random configurations which the Hamiltonian may acquire in a disordered system. Essentially the Green function is expanded as a

continued fraction [13],

$$\begin{aligned}\langle\langle G(\mathbf{k},\omega^2)\rangle\rangle &= \cfrac{1}{\omega^2-\alpha_1(\mathbf{k})-\cfrac{\beta_1^2(\mathbf{k})}{\omega^2-\alpha_2(\mathbf{k})-\cfrac{\beta_2^2(\mathbf{k})}{\ddots\, T(\mathbf{k},\omega^2)}}} \\ &= \frac{1}{\omega^2-\omega_0^2(\mathbf{k})-\Sigma(\mathbf{k},\omega^2)} \qquad (1.15)\end{aligned}$$

The above continued fraction expansion is terminated after a suitable number of steps by the so-called Beer-Pettifor terminator $T(\mathbf{k},\omega^2)$ [14] which preserves the Herglotz analytic properties of the Green's function. The disorder-induced self-energy $\Sigma(\mathbf{k},\omega^2)$ is a signature of the damped vibrations arising out of random scattering and ω_0 are the band frequencies in the absence of disorder. Phonon self-energy Σ is intrinsically dependent on the wave-vector $\mathbf{k}$ as is evident from most neutron scattering experiments.

1.3.1 Spectral function and Phonon DOS

Once the Green's function $\langle\langle G(\mathbf{k},\omega^2)\rangle\rangle$ is calculated, the spectral function is obtained as,

$$A(\mathbf{k},\omega^2) = -\frac{1}{\pi}\Im m\langle\langle G(\mathbf{k},\omega^2)\rangle\rangle \qquad (1.16)$$

A more frequently used quantity is the *Coherent Scattering Structure Factor* $S_{coh}(\mathbf{k},w^2)$, which is basically the same as the spectral function except that the fluctuation in the scattering length of different atomic species is also included in the definition of S_{coh}. All of our results are based on the structure factor. The dispersion curves for different modes are then obtained numerically by calculating the peak frequencies of these structure factors.

The disorder-induced widths are the quantities which are more sensitive to the effect of randomness as compared to the dispersion, and as such is one of the focus of the present work. In order to extract these full widths at half maxima (FWHM), we have fitted the coherent structure factors to lorenzians exactly as experimentalists do to extract the same.

The phonon DOS is obtained by integrating the structure factor over the Brillouin zone,

$$\begin{aligned} n(\omega) &= \sum_{\lambda} \langle\langle n_{\lambda}(\omega)\rangle\rangle \\ &= -\frac{2}{3\pi}\frac{1}{\Omega_{BZ}}\sum_{\lambda}\int_{BZ} \Im m\langle\langle G_{\lambda}(\mathbf{k},\omega^2)\rangle\rangle \omega d\omega \end{aligned} \tag{1.17}$$

where λ is the normal-mode branch index and α is the SRO parameter.

1.3.2 Vibrational entropy

The lattice heat capacity (C_v^{β}) of a phase (β) is determined by its phonon DOS $n(w,\alpha)$. The difference $\Delta C_v^{\beta-\beta'}$ for two phases β and β' of a compound depends on the difference in their phonon DOS as,

$$\begin{aligned} \Delta C_v^{\beta-\beta'}(T) &= 3Nk_B\int_0^{\infty}\left[n^{\beta}(\omega)-n^{\beta'}(\omega)\right] \\ &\quad\times\left(\frac{h\nu}{k_BT}\right)^2\frac{e^{h\nu/k_BT}}{(e^{h\nu/k_BT}-1)^2}d\nu, \end{aligned} \tag{1.18}$$

where $\omega = 2\pi\nu$

The thermodynamic importance of vibrational entropy has often been neglected, but recent measurements show that it affects the relative stability of chemically ordered and disordered phases [15, 16, 17]. As a matter of fact, in many systems, the

vibrational entropy difference between two phases comes out to be comparable to the configurational entropy difference. The difference in vibrational entropy of two phases β and β', $\Delta S_{vib}^{\beta-\beta'}$ can be obtained from the difference in their lattice heat capacity $\Delta C_v^{\beta-\beta'}$ as:

$$\Delta S_{vib}^{\beta-\beta'}(T) = \int_0^T \frac{\Delta C_v^{\beta-\beta'}(T')}{T'} dT' \tag{1.19}$$

In the higher temperature limit ($T \geq \Theta_{Debye}$), combination of Eq. 1.18 and 1.19 yields,

$$\Delta S_{vib}^{\beta-\beta'}(T) = -3Nk_B \int_0^\infty \left[n^\beta(\nu) - n^{\beta'}(\nu)\right] ln(\nu) d\nu \tag{1.20}$$

Configurational entropy is a measure of the degree of disorder for an alloy. For a homogeneously disordered binary alloy, the configurational entropy is given by,

$$S_{\text{homog}} = -k_B \left[x\ ln(x) + (1-x) ln(1-x)\right] \tag{1.21}$$

This approximation assumes that all the lattice sites are equivalent and uncorrelated. However in an alloy with certain degree of order, not all lattice sites are equivalent and a certain degree of correlation always exists between lattice positions.

1.3.3 Thermal Conductivity and Diffusivity

The expression for the lattice thermal conductivity requires the configuration average of the response functions of,

$$\begin{aligned} \langle\langle \kappa(z_1, z_2, T) \rangle\rangle \ &= \\ &\int \frac{d^3\mathbf{k}}{8\pi^3} \text{Tr}\left[\langle\langle \mathbf{S}(\mathbf{k}, T)\mathbf{G}(\mathbf{k}, z_1)\mathbf{S}(\mathbf{k}, T)\mathbf{G}(\mathbf{k}, z_2)\rangle\rangle\right], \end{aligned} \tag{1.22}$$

where $\mathbf{S}$ is the heat current operator, $\mathbf{G}$ is the phonon propagator and $\langle\langle\ \ \rangle\rangle$ denotes configuration averaging. The expression for thermal diffusivity is similar to

conductivity $\langle\langle\kappa\rangle\rangle$ and given by,

$$\begin{aligned}\langle\langle D(\nu)\rangle\rangle &= \frac{1}{\pi^2}\int d\nu' \int \frac{d^3\mathbf{k}}{8\pi^3} \\ &\mathrm{Tr}\left[\langle\langle \Im m\mathbf{G}(\mathbf{k},\nu')\mathbf{S}(\mathbf{k})\Im m\mathbf{G}(\mathbf{k},\nu')\mathbf{S}(\mathbf{k})\Im m\mathbf{G}(\mathbf{k},\nu)\rangle\rangle\right]. \qquad (1.23)\end{aligned}$$

One can notice that thermal conductivity Eq. 1.22 involves the configuration average of four random functions while thermal diffusivity Eq. 1.23 involves the configuration average of five random functions whose fluctuations are correlated.

Chapter 2

Phononic properties with short-range order (SRO)

2.1 Introduction

Study of lattice vibrations and their effect is a long-standing problem for first-principles calculation of substitutional alloy thermodynamics. The complicated nature of phonon problem is due to existence of off-diagonal disorder in the dynamical matrix. Moreover, the sum rule obeyed by the diagonal and off-diagonal parts of the force constants leads to another kind of disorder called environmental disorder [18]. Including short-range features make the problem even more complicated. One then requires to carry out a conditional configuration averaging scheme discussed in chapter (1) for the disordered alloy, which captures the effect of correlated disorder. Typically, the ranges of inter-atomic force constants are not much larger than inter-atomic distances. Although phonons have many wavelengths, most of them in solids have high

[0]The contents of this chapter has been published in two papers :

1. Aftab Alam, Rajiv Kumar Chouhan, and Abhijit Mookerjee *Phys. Rev.* **B 83**, 054201(2011)
2. Rajiv Kumar Chouhan, Aftab Alam, Subhradip Ghosh and Abhijit Mookerjee, *J. Phys. Condensed Matter* **24** 375401 (2012)

frequencies and short wavelengths. Nevertheless, there have been no detailed first-principles investigation of how the phonon density of states (DOS) depend on the short-range ordering (or local atomic configuration) of alloys. In addition since the phonon DOS is a key quantity for any understanding of vibrational entropy (at least in the harmonic approximation), such a dependence of short-range ordering (SRO) is implicitly hidden on the entropy as well. Keeping in mind a growing effort in understanding the reason behind the vibrational entropy differences between various states of materials [19, 20], we formulated a new method which can take into account the effect of local chemical environment on the lattice dynamics of disordered alloys and hence provide a deeper insight to understand the origin of such entropy differences. Within the experimental framework, there have been advances made in this direction. Experimental literature mainly relies on three basic techniques namely, differential calorimetry measurement [20, 21], inelastic neutron scattering [22] and nuclear resonant inelastic x-ray scattering method [15]. Of them the nuclear resonant scattering experiment seems quite promising. Some of the application of this method provide a better understanding of the micro structure of alloys by assigning the dependence of local chemical environment on the phonon DOS [23]. Although such topic is littered by the experimental studies, a complete theoretical understanding is still lacking. This situation has motivated a few theoretical studies [24, 25, 26], which addressed properties that are sensitive to the presence of short-range ordering in the alloys. However, to our knowledge, the application of such methods are either limited to model systems or based on the use of a separate *ab-initio* energetics and inter atomic potentials. It is therefore required to have a direct first-principles calculation of the lattice dynamics and the vibrational entropy of disordered alloys with short-range order.

Taking a challenge of this possibility and motivated by a lack of available knowledge, we present a generalized method to investigate the vibrational properties of disordered alloys with SRO. This method should explicitly take into account the fluctuation in masses, scattering length (diagonal disorder) and force constants (off-diagonal disorder). The generalization should in principle allow the method an extra capability of capturing effect of correlated disorder arising out of the SRO. This technique is based on the augmented space theorem suggested by Mookerjee(1973) [10] combined with the recursion method of Haydock(1972) [12] to obtain the conditional configuration averaged Green function mentioned in chapter (1).

Keeping in mind the increasing interest in investigating the role of phonon entropy on the thermodynamic stability of compound, we choose a technologically important alloy system, namely FeCr. The phase diagram of FeCr at high temperatures, includes a bcc single-phase region over a broad range of composition, with a σ-phase region near equiatomic compositions from 725K to 1103K. Experimental observations in the temperature range 675K - 773K indicate that chemical unmixing occurs homogeneously by a mechanism like spinodal decomposition [27]. In fact FeCr alloys constitute the basic ingredient of stainless steels that for a century have been one of the most important structural material, hence some properties of stainless steel are inherited from the parent alloy. The present investigation was performed to asses the phonon DOS and vibrational entropy of mixing of bcc FeCr. In addition, we also analyze (from the first principles calculation) for the first time the effects of SRO on these lattice dynamical properties, which in turn is related to the thermodynamics of the alloy.

Various mechanisms have been suggested from time to time to explain the origin of vibrational entropy differences in alloys. Some of them are the *bond proportion* effect

[28], the *volume* effect, the *size mismatch* effect [29] etc. The entropy difference is actually related to the difference in the phonon DOS between the two concerned states. An intrinsic quantity from which this phonon DOS is obtained in most of the theoretical calculation are the phonon dispersion. In disordered alloys, these dispersion are associated with a full width at half maxima (FWHM), which provide finite life-time broadening to the phonon scattering. Considering this quantity to be one of the most basic quantity in any phonon theory of disordered alloys, we intuitively connect them to explain a general trend of the magnitude of vibrational entropy difference.

In contrast to the previous semi-emperical calculations [25] and experiments [22, 16], we found a comparatively smaller value of the phonon entropy of mixing. We shall provide plausible explanations for the comparatively large value of vibrational entropy difference obtained in previous studies. While this result does not rule out the possibility that lattice vibrations play a significant role in other systems, it does point out that vibrational effects in Fe-Cr may be comparatively smaller than originally claimed.

We carried out similar kind of study for Rhenium Tungsten (ReW) alloys performing $ab-initio$ study of the phonon properties. Technologically W is the core material making up the shield in fusion devices and $Re_{1-x}W_x$ and large doses of neutron radiation during fusion process converts some of the W atoms into Re. This happens at random sites on the W lattice. After continuous radiation for years, the material converts to a disordered binary alloy within a certain atomic % of Re ($\simeq 27\%$) in a body-centered cubic (bcc) structure. Beyond these concentrations, the bcc structure slowly becomes dynamically unstable [30]. Alloys of Re are also of interest to materials scientists, as when Re alloyed with group VI metals reinforces their mechanical

strength, at the same time it improves their plasticity [30]-[31]. Alloying with Re is an efficient way of designing materials with specified mechanical properties. These Re doped alloys are prepared by chemical vapor deposition [32]. In spite of this alloy being of technological importance, there have been very few theoretical or experimental works reported in literature. The only theory was by Persson *et.al.*[31]. We choose three different alloy concentrations: $x = 0.75, 0.43$ and 0.29. The choice is deliberate because persson *et.al.*[31] have investigated the same set of alloys with a different method. They, however, have not provided a complete picture for the three alloys in the bcc phase. In addition, due to the nature of their theoretical method, it is not clear whether they are able to calculate quantities like phonon lifetime (an important observable from neutron scattering), self energy, SRO effects etc.

The augmented space method has been described in great detail in chapter (1) of this thesis, we shall introduce here only those salient points which will be of direct relevance to our generalization to SRO for phonon problem. Detailed discussion were done by Alam *et.al.*(2004) and Mookerjee *et.al.*(2003) [13, 33].

2.2 Multiple Scattering Phenomenon

During the process a phonon propagates in a random alloy, it encounters irreducible multiple scattering both repeatedly off a single fluctuations and successively off fluctuations on the different sites. As mentioned in beginning of this chapter, being a single-site mean-field approximation CPA takes into account only the single fluctuation. This is precisely shown in the left panel of Fig. 2.1, which is a 2-dimensional cartoon diagram of the multiple scattering phenomenon captured by CPA. The black circle is a single fluctuation site embedded in an average medium denoted by light circle. Within the CPA (diagonal disorder), the irreducible scattering by the defect size

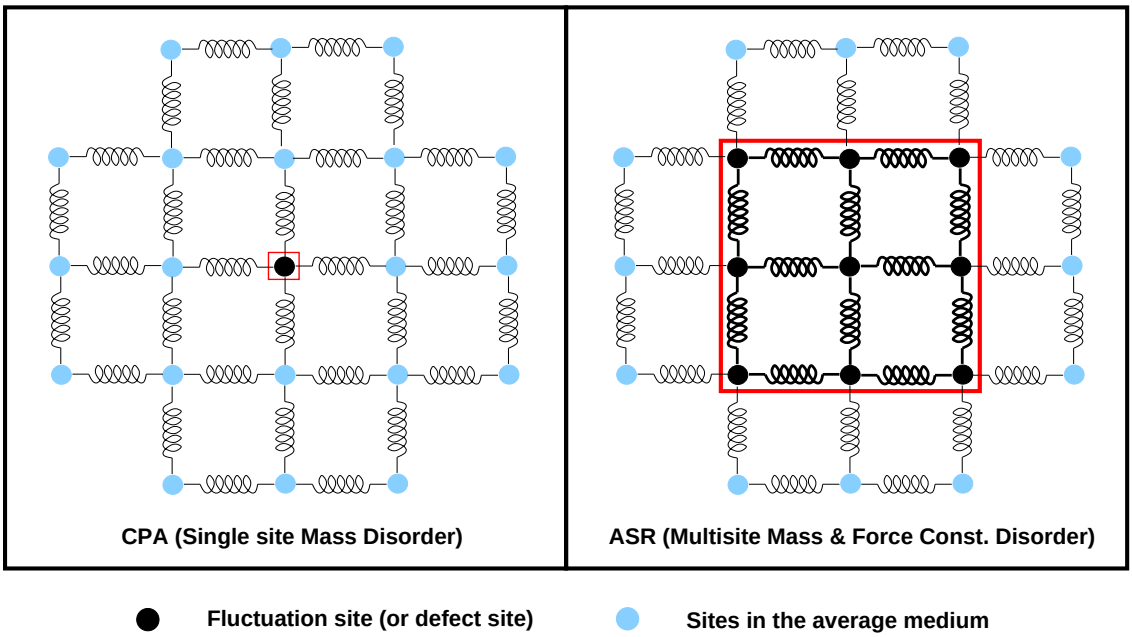

Figure 2.1: (Color Online) Multiple scattering picture for the singles-site CPA, and the multi-site ASR. The black dark circles indicate the fluctuation site and the red square around them indicates the region of influence. Within CPA the effect of fluctuation is limited to the single site itself, however ASR takes into account the influence to neighboring sites as well.

is confined to the defect site itself. The red box around the fluctuation site indicates the region of influence of the perturbation. This is an oversimplified model of phonon problem for disordered alloys, since none of the springs are affected by the presence of this defect as the force constants are same everywhere. In other words, the averaging is done over all possible occupation of single site only. The right panel in Fig. 2.1 illustrates the multiple scattering phenomenon captured within our augmented space method. One can easily see the difference compared to the CPA case. In this picture, the main difference is the region of perturbation which is not only the site of fluctuation but also its neighboring environments. The box around the dark circles shows the region of influence, which is an example of a model including the effect of 2nd nearest neighbor environment. One can perform calculation for extended neighbors as well.

During the process of propagation, the phonon at the fluctuation site scatters from all of its neighbors, and their force constants also undergo fluctuations (indicated by thick spring lines in contrast to the thin ones for the average medium). In fact, the whole cluster of atoms (within the red box) undergoes fluctuations both in masses (diagonal disorder) and force constants (off-diagonal disorder). This is an example of homogeneous disorder. Another thing to notice is the way scattering is spreaded all over the lattice, although the strength of scattering decreases with distance because of the short-range nature of phonon interaction. Apart from the fluctuations in masses and force constants, the scattering length of the alloy species might be very different from one another. For the sake of completeness, we have also included the fluctuations in scattering lengths.

2.3 Short range order (SRO) in phonons

Here we shall present a generalization of the Augmented space formalism to the phonon problem for the first time and hence relate it to the phonons DOS and vibrational entropy. We shall first present the salient features of the method for homogeneous disorder, and then discuss its generalization to inhomogeneous (or correlated) disorder.

The basic idea behind the augmented space method for configuration averaging is to extend the usual real Hilbert space $\mathcal{H}$ to include a configuration space $\mathbf{\Psi}$. Disorder fluctuations are described in $\mathbf{\Psi}$. Suppose $\{n_R\}$ be a collection of discrete independent random variables and $F(\{n_R\})$ be some function of these variables. If each random variables n_R takes on values $\{m_1, m_2, \ldots, m_r, \ldots\}$ one can decompose the

joint probability distribution function of these variables $P(\{n_R\})$ as:

$$P(n_1, n_2 \ldots, n_r, \ldots) = p_1(n_1)\ p_2(n_2) \ldots p_r(n_r) \ldots$$

Each p_i is +ve definite and has finite moments to all orders. A Hilbert space Ψ_R (spanned by the state of n_R) is constructed for each density p_R, and the full system configuration space is defined as $\mathbf{\Psi} = \prod_R^{\otimes} \Psi_R$. A self-adjoint operator $N_R \in \Psi_R$ is associated with each random variable n_R, such that

$$p_R(n_R) = -\frac{1}{\pi} \lim_{\delta \to 0} \Im m \langle \nu_0^R |\ [(n_R + i\delta)I - N_R]^{-1}\, |\nu_0^R\rangle, \tag{2.1}$$

where $\nu_0^R = \sum_{j=1}^{\alpha} w_j |m_j^R\rangle$ is a specific member of Ψ_R. The ground state $|\nu_0\rangle$ in the full product space Ψ is defined as $|\nu_0\rangle = \prod_j^{\otimes} |\nu_0^j\rangle$.

According to augmented space theorem, the configuration average of $F(\{n_R\})$ is

$$\langle F \rangle = \langle \nu_0 |\ \widetilde{F}(\widetilde{N}^{(1)}, \widetilde{N}^{(2)}, \ldots, \widetilde{N}^{(R)}, \ldots) |\nu_0\rangle,$$

where

$$\widetilde{N}^{(R)} = I \otimes \ldots \otimes N_R \ldots \otimes I \otimes \ldots \tag{2.2}$$

and $\widetilde{F}$ is the same function of $\widetilde{N}^{(R)}$ as F was of $n_R's$. The calculation of the configuration average $\langle F \rangle$ thus reduces to the problem of obtaining the above expectation value.

However if the random variables $\{n_R\}$ are correlated (instead of being independent), then the joint probability distribution should be decomposed as:

$$P(n_1, n_2 \ldots, n_r, \ldots) = p_1(n_1)\ p_2(n_2|n_1)\ p_3(n_3|n_1, n_2) \ldots \tag{2.3}$$

And in general for a correlated variable n_R, one has an associated operator,

$$\widetilde{N}_{\text{corr}}^{(R)} = \sum_{l_1} \cdots \sum_{l_{R-1}}\ P_1^{l_1} \otimes P_2^{l_2} \otimes \ldots \otimes N_R^{l_1, \ldots l_{R-1}} \otimes I \otimes \ldots \tag{2.4}$$

where the operator $N_R^{l_1,\ldots l_{i-1}}$ is associated with the conditional probability density $P_i^{l_i}$ and $p_i(n_i|n_1, n_2, \ldots n_{i-1})$ are projection operators on a specific state l_i. The elegance of the formulation is that, the basic augmented space theorem still holds good rigorously, but $\widetilde{N}(R)$ instead being of the form given by Eq. 2.2, now has the form of Eq. 2.4.

For a binary alloy, the macroscopic state of order is described in terms of the Warren-Cowley short-range order parameter,

$$\alpha_R^{AB} = 1 - \frac{P_R(B|A)}{y}$$

where the center of R-th shell is occupied by A-atom, y denotes the macroscopic concentration of species B, and P_R is the probability of finding a B-atom anywhere in the R-th shell centered around an A-atom.

In terms of the above defined SRO parameter, the probability density associated with the sites belonging to first nearest neighbor shell is given by,

$$\begin{aligned} p(n_{R_2}|n_{R_1}=1) &= (x+\alpha y)\delta(n_{R_2}-1) + (1-\alpha)y\delta(n_{R_2}) \\ p(n_{R_2}|n_{R_1}=0) &= (y+\alpha x)\delta(n_{R_2}) + (1-\alpha)x\delta(n_{R_2}-1), \end{aligned} \tag{2.5}$$

where n_{R_1} is the variable associated with central atom. Also $\alpha = \alpha_1^{AB}$ and $x + y = 1$.

The construction of operator corresponding to the conditional probability density for the occupation variable has been discussed in detail by Alam and Saha [34]. Here we mention only the final form of augmented space operators associated with the

conditional probability density given by Eq. 2.4 as,

$$\begin{aligned}\widetilde{N}^{(R)}_{\rm corr} &= xp_1^0 \otimes p_R^0 + yp_1^0 \otimes p_R^1 + X_1\ p_1^1 \otimes p_R^0 + X_2\ p_1^1 \otimes p_R^1 \\ &+U_1\ p_1^0 \otimes (\tau_R^{01} + \tau_R^{10}) + U_2\ p_1^1 \otimes (\tau_R^{01} + \tau_R^{10}) \\ &+U_3\ (\tau_1^{01} + \tau_1^{10}) \otimes p_R^0 + U_4\ (\tau_1^{01} + \tau_1^{10}) \otimes p_R^1 \\ &+U_5\ (\tau_1^{01} + \tau_1^{10}) \otimes (\tau_R^{01} + \tau_R^{10}), \end{aligned} \tag{2.6}$$

where p_k^0, p_k^1 denotes the projection operators and τ_k^{01}, τ_k^{10} are the transfer operators. The constants are defined as:

$$\begin{aligned} X_1 &= x - \alpha(x-y),\ \ X_2 = y + \alpha(x-y) \\ U_1 &= x\sqrt{(1-\alpha)y(x+\alpha y)} + y\sqrt{(1-\alpha)x(y+\alpha x)} \\ U_2 &= y\sqrt{(1-\alpha)y(x+\alpha y)} + x\sqrt{(1-\alpha)x(y+\alpha x)} \\ U_3 &= \alpha\sqrt{xy},\ \ U_4 = -\alpha\sqrt{xy} \\ U_5 &= \sqrt{xy}\left[\sqrt{(1-\alpha)y(x+\alpha y)} - \sqrt{(1-\alpha)x(y+\alpha x)}\right] \end{aligned}$$

We should also mention at this point that the augmented space operator $\widetilde{N}^{(R)}$ associated with independent probability density $p_R(n_R)$ is:

$$\widetilde{N}^{(R)} = x\ p_R^0 + y\ p_R^1 + \sqrt{xy}(\tau_R^{01} + \tau_R^{10}) \tag{2.7}$$

The next step is to use these operators and the central theorem for correlated random variables to set up an effective Hamiltonian in augmented space for the phonon problem. For the phonon problem, the Green function for a disordered binary alloy in reciprocal space representation is given by,

$$\langle\langle G(\mathbf{k}, w^2)\rangle\rangle = \frac{1}{N}\sum_{R\ R'} e^{i\mathbf{k}.(\mathbf{R}-\mathbf{R'})}\langle\langle R|(\mathbf{M}w^2 - \mathbf{D})^{-1}|R'\rangle\rangle,$$

where

$$\begin{aligned}\mathbf{M} &= \sum_R m_R P_R, \;\; m_R = m^A n_R + m^B(1-n_R) \\ \mathbf{D} &= \sum_R \Phi_{RR} P_R + \sum_{R,R'\neq R} \Phi_{RR'} T_{RR'}\end{aligned}$$

along with the sum rule,

$$\Phi_{RR'} = -\sum_{R'\neq R} \Phi_{RR'}$$

and in terms of random variables,

$$\begin{aligned}\Phi_{RR'} &= \Phi^{AA}_{RR'} n_R n_{R'} + \Phi^{BB}_{RR'}(1-n_R)(1-n_{R'}) + \\ &\quad \Phi^{AB}_{RR'}\{n_R(1-n_{R'}) + (1-n_R)n_{R'}\}. \end{aligned} \tag{2.8}$$

$\langle\langle\rangle\rangle$ stands for the configuration averaging over random variables, R, R' refer to lattice positions. $\mathbf{M}$ and $\mathbf{D}$ are the mass and dynamical matrices in vibrational mode space. $\{n_R\}$ are the random site-occupation variables.

A convenient way of representing states in the configuration space $\mathbf{\Psi} = \prod_R^{\otimes} \Psi_R$ is the use of *cardinality sequence*, which is basically the sequence of sites $\{C\}$ at which one has an atom of type B corresponding to the value of random variable $n_R = 1$. In the language of ising model, we shall denote such a state by a $\downarrow$ configuration and those sites occupied by an atom of type A by $\uparrow$. For example, for the state $\{C\} = |\{\downarrow_2, \downarrow_5, \downarrow_7, \ldots\}\rangle$, the site numbers $2, 5, 7, \ldots$ are occupied by B-atoms. If we define $|\{\uparrow, \uparrow, \ldots, \uparrow \ldots\}\rangle$ as the *reference* configuration, then the *cardinality sequence* of this configuration is a null sequence $\{\emptyset\}$

According to augmented space theorem, the configuration averaged Green function can be expressed as,

$$\langle\langle G(\mathbf{k}, w^2)\rangle\rangle = \langle \mathbf{k} \otimes \{\emptyset\} | (\widetilde{\mathbf{M}} w^2 - \widetilde{\mathbf{D}})^{-1} | \mathbf{k} \otimes \{\emptyset\}\rangle, \tag{2.9}$$

where the augmented **k**-space basis has the form

$$|\mathbf{k}\otimes\{\emptyset\}=\frac{1}{\sqrt{N}}\sum_{R}e^{-i\mathbf{k}.\mathbf{R}}|R\otimes\{\emptyset\}.$$

The augmented space operators $\widetilde{\mathbf{M}}$ and $\widetilde{\mathbf{D}}$ are constructed from the original random operators (Eq. 2.8) by replacing all the random variables $\{n_R\}$ associated with correlated disorder (i.e. n_R corresponding to the sites in the nearest neighbor shell of the central site) by $\widetilde{N}^R_{\text{corr}}$ (given by Eq. 2.6) and all the other variables $\{n_R\}$ associated with un-correlated disorder by $\widetilde{N}^R$ (given by Eq. 2.7). $\widetilde{\mathbf{M}}$ and $\widetilde{\mathbf{D}}$ are the operators in the enlarged augmented space $\mathbf{\Xi}=\mathcal{H}\otimes\Psi$, which contains the information about both the real Hilbert space and the statistical fluctuation of the system arising out of disorder.

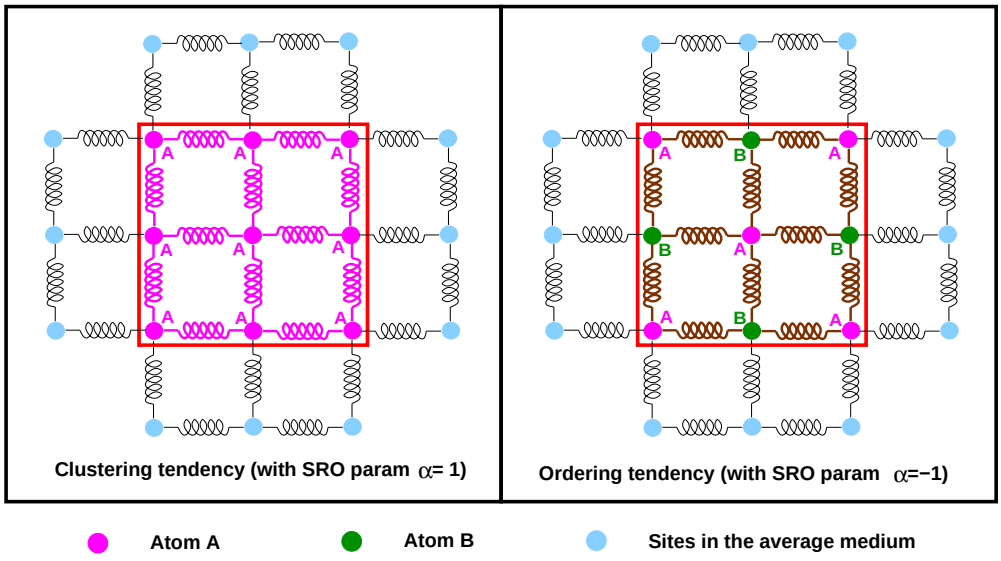

Figure 2.2: (Color Online) Multiple scattering picture for the disordered alloy with short rang ordering. Left panel shows a clustering tendency while the right panel an ordering tendency. The range of short-range correlation is extended up to the 2nd nearest neighbors in this cartoon diagram (shown by the red box).

Keeping in mind the two forms of operator $\widetilde{N}$ (i.e. $\widetilde{N}^R_{\rm corr}$ and $\widetilde{N}^R$: one indicating the signature of correlated disorder cluster with conditional probability and the other the rest of the homogeneous disordered medium), the augmented space operators $\widetilde{\mathbf{M}}$ and $\widetilde{\mathbf{D}}$ can be expressed as:

$$\widetilde{\mathbf{M}} = m_B\widetilde{\mathcal{I}}\otimes I + \delta m\left[\sum_{R\notin\text{corr}}\widetilde{N}^R + \sum_{R\in\text{corr}}\widetilde{N}^R_{\rm corr}\right]\otimes P_R, \tag{2.10}$$

$$\begin{aligned}
\widetilde{\mathbf{D}}_{off} &= \left[\sum_{R\notin\text{corr}}\sum_{R'\notin\text{corr}}\left\{\Phi^{BB}_{RR'}\widetilde{\mathcal{I}} + \Phi^{(1)}_{RR'}(\widetilde{N}^R + \widetilde{N}^{R'}) + \Phi^{(2)}_{RR'}\widetilde{N}^R\widetilde{N}^{R'}\right\} + \right. \\
&\quad \left.\sum_{R\in 1}\sum_{R'\in\text{corr}}\left\{\Phi^{BB}_{RR'}\widetilde{\mathcal{I}} + \Phi^{(1)}_{RR'}(\widetilde{N}^R + \widetilde{N}^{R'}_{\rm corr}) + \Phi^{(2)}_{RR'}\widetilde{N}^R\widetilde{N}^{R'}_{\rm corr}\right\}\right]\otimes T_{RR'}, \\
&= \left[\sum_{R\notin\text{corr}}\sum_{R'\notin\text{corr}}\Phi^{\rm uncorr}_{RR'} + \sum_{R\in 1}\sum_{R'\in\text{corr}}\Phi^{\rm corr}_{RR'}\right]\otimes T_{RR'}, \\
\widetilde{D}_{dia} &= -\left[\sum_{R\notin\text{corr}}\sum_{R'\notin\text{corr}}\Phi^{\rm uncorr}_{RR'} + \sum_{R\in 1}\sum_{R'\in\text{corr}}\Phi^{\rm corr}_{RR'}\right]\otimes P_R, \\
\widetilde{D} &= \widetilde{D}_{dia} + \widetilde{D}_{off},
\end{aligned} \tag{2.11}$$

where

$$\begin{aligned}
\delta m &= m^A - m^B, \quad \Phi^{(1)}_{RR'} = (\Phi^{AB}_{RR'} - \Phi^{BB}_{RR'}), \\
\Phi^{(2)}_{RR'} &= (\Phi^{AA}_{RR'} + \Phi^{BB}_{RR'} - 2\Phi^{BB}_{RR'}).
\end{aligned}$$

Once the augmented space operators $\widetilde{\mathbf{M}}$ and $\widetilde{\mathbf{D}}$ are constructed, the configuration averaged Greens function is obtained from Eq. 2.9 using the recursion method of Haydock *et.al.*(1972) [12].

In terms of multiple scattering picture, the above mathematical formulation can explain a number of situations describing the short-ranged correlations depending

on the value of warren-cowley parameter α. Out of various other possibilities, the tendency of clustering and ordering are described in Fig. 2.2 for the two extreme values of α (+1 and -1) for a $50-50$ alloy. The left panel shows the clustering tendency with the effect of short-range correlation maintained till the second nearest neighbor (shown by the red box), and the right panel shows the ordering tendency with the same range of correlation.

An important SRO effect we studied for configurational entropy (see chapter 1). In this case there exists a finite cluster up to which the correlation between sites remain stronger and decay rapidly with increasing distance. All the correlations are described within the basic cluster and the rest of the lattice sites are considered to be homogeneously disordered. Since one of our focus in this chapter is to describe states with certain degree of SRO, we choose the basic clusters to be pairs for simplicity. The configurational entropy (including pairs up to n-th nearest neighbor distance) for a random binary alloy with SRO is given by,

$$S_{\rm corr}^{(n)} = S_{\rm homog} - S_{\rm homog}\left(\sum_{j=1}^{n} N^{(j)}\right) - k_B \sum_{j=1}^{n} \frac{N^{(j)}}{2} .... \\ .... \left[P_j^{AA} ln(P_j^{AA}) + 2P_j^{AB} ln(P_j^{AB}) + P_j^{BB} ln(P_j^{BB})\right], \tag{2.12}$$

where $N^{(j)}$ denotes the number of atoms in the j-th neighboring shell, Also the pair probabilities P_j's are given by,

$$P_j^{AA} = y^2 + xy\alpha_j, \quad P_j^{AB} = xy(1-\alpha_j), P_j^{BB} = x^2 + xy\alpha_j,$$

where α_j is the SRO-parameter in the j-th nearest neighbor shell.

It is easy to verify that for $\alpha_j = 0(\forall j)$, $S_{\rm corr}$ reduces to $S_{\rm homog}$. In addition, the term under the summation converge to zero with increasing distance, meaning that lattice sites separated by large distances are uncorrelated. In our case of bcc

disordered alloy, we verified that the inclusion of third neighbor pairs modifies the entropy only by 0.005% confirming the short-range nature of the correlations.

2.4 Case 1: $Fe_{1-x}Cr_x$ bcc binary alloy

Ab-initio Quantum Espersso [35] code has been used to compute the Fe-Fe, Fe-Cr and Cr-Cr dynamical matrices at different bond lengths with different ordered structures. Force constants for B2 FeCr, DO_3 Fe_3Cr and $FeCr_3$, and bcc Fe and bcc Cr at their equilibrium lattice parameters have been used to estimate the random alloy dynamical matrix. Quantum Espresso is based upon the density functional perturbation theory (DFPT) [36], which is basically a linear response method to study the electronic structure and phonon excitations in condensed matter systems. Within this method, the dynamical matrix associated with the lattice dynamics of the system can be obtained from the ground state electron charge density and its linear response to a distortion of the nuclear geometry. In terms of computational efficiency, one of the greatest advantages of DFPT (as compared to other non-perturbative methods) is that within this method the responses to perturbation of different wavelengths are decoupled. This feature allows one to calculate phonon frequencies at arbitrary wave-vectors avoiding the use of supercells and with a workload that is independent of the phonon wavelength. The calculation were done at the alloy lattice constants: a=2.873$\dot{A}$ for $Fe_{75}Cr_{25}$, a=2.876$\dot{A}$ for $Fe_{50}Cr_{50}$ and a=2.879$\dot{A}$ for $Fe_{25}Cr_{75}$. Ultra soft pseudo-potentials with nonlinear core corrections [37] were used. PBE-96 spin-polarized generalized gradient approximate (GGA) functionals were used for exchange-correlation part of the potential. The reason for choosing GGA functionals is its better capability to calculate the ground state properties. Plane waves with energies up to 55 Rydberg are used in order to describe electron wave function and

Fourier components of the augmented charge density with cut-off energy of up to 650 Rydberg are taken into account. The Brillouin zone integrations are carried out with Methfessel Paxton smearing [38] using a $14 \times 14 \times 14$ **k**-point mesh. The value of smearing parameter is 0.01 Rydberg. These parameters are found to yield phonon frequencies converged to within 5%. Once the electronic structure calculation is converged within a desired accuracy, the force constants are then computed first in reciprocal space on a finite **q**-point grid and then a Fourier transformation is employed to obtain the real space force constant. In this work, we have used a $8 \times 8 \times 8$ **q**-point mesh, which provide a sufficiently dense grid.

The augmented space recursion (ASR) calculation for the random alloy is done by generating a map from a real space cluster of 700 atoms. The disorder in the force constants were considered till the 2nd nearest neighbor shell, which consists of 14 sites for a bcc structure. The phonon DOS is calculated on a frequency mesh of 1001 points with a small smearing of 0.005. However for a more accurate calculation of vibrational entropy, the phonon DOS used in the entropy expression was calculated at 2001 points.

In terms of computational efficiency, one of the advantages of **k**-space recursion (over the real space one) is the possibility of working in an enormously reduced space (compared to the Hilbert space required in the real space recursion method). It can be shown explicitly [39] that the operation of effective Hamiltonian (in **k**-space recursion method) can entirely be done in configuration space only and the calculation does not require us to involve the Hilbert space $\mathcal{H}$ at all. Thus, for example, for a system with N-sites and m-possible realizations of the random variables associated with each site, the augmented space involved $\mathrm{N} \times \mathrm{m}^{\mathrm{N}}$ basis functions. The standard real space method for implementing this on a computer would require handling an

impossibly large $(\mathrm{Nm^N})\times(\mathrm{Nm^N})$ matrices. The first reduction of computational cost in a **k**-space recursion comes in the form of dealing with smaller sub-space of such a huge product space. Since in the **k**-space recursion, one requires to deal only with the configuration space, so instead of handling the enormously large matrix of rank $(\mathrm{Nm^N})\times(\mathrm{Nm^N})$, one need to work with a matrix of rank $(\mathrm{m^N})\times(\mathrm{m^N})$ only. In addition, the approximation involved in truncating the full lattice to a large cluster (in real space method) is also avoided. Secondly, we can utilize the local symmetries of the configuration space (as described earlier [40]) to further reduce its rank. Finally we have used memory reduction and time saving for ASR by taking advantage of multi-spin coding technique. In other words, one can utilize the bit manipulation technique and predefined logical functions in the computer to store the basis vectors of configuration space in bits associated with different words.

2.4.1 $\mathrm{Fe}_{1-x}\mathrm{Cr}_x$ Alloy $(x = 0.25, 0.47, 0.75)$

In this section, we focus on the lattice dynamics of three bcc $\mathrm{Fe}_{1-x}\mathrm{Cr}_x$ ($x = 0.25, 0.47$ and 0.75) alloys. The present study will be based on the phonon dispersion, phonon DOS, lattice heat capacity, vibrational and configurational entropy for these alloys. The trend and the magnitude of the phonon entropy as a function of the alloy composition (x) will be discussed in some detail. We also provided plausible explanation for our smaller value of vibrational entropy of mixing(compared to other findings).

In Fig.2.3 we display the phonon dispersion curves for the three $\mathrm{Fe}_{1-x}\mathrm{Cr}_x$ ($x = 0.25, 0.47$ and 0.75) alloys. The error bars in all the three panels represent the full widths at half maxima (FWHM) at various ζ-values. Interestingly, the gross feature of dispersion for all the three alloys, including the Cr-rich $\mathrm{Fe_{25}Cr_{75}}$, resemble much more the phonon dispersion of bcc Fe, than that of bcc Cr. The disorder-induced line-

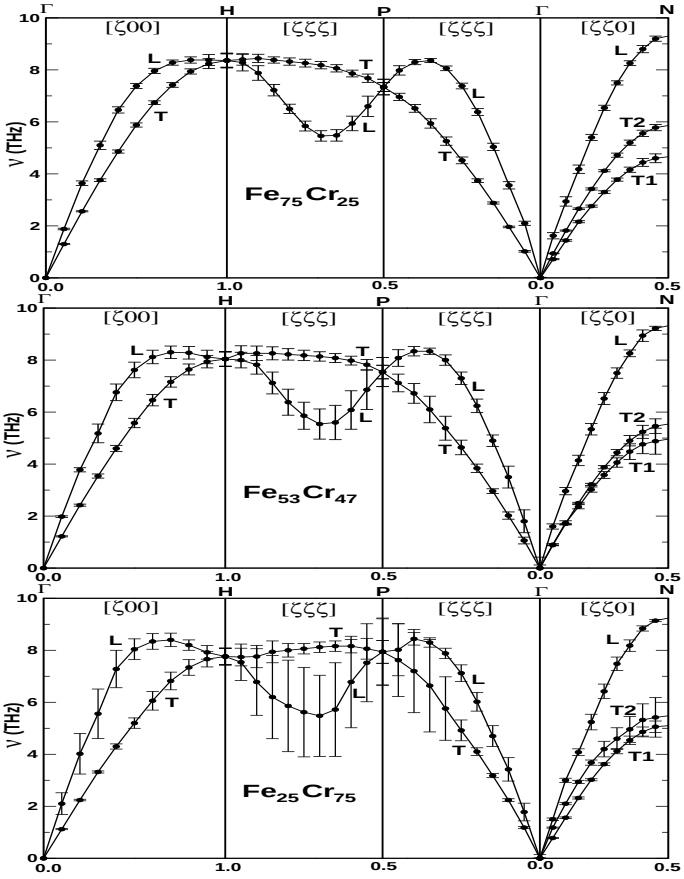

Figure 2.3: Phonon dispersion curves for three $Fe_{1-x}Cr_x$ ($x = 0.25, 0.47$ and 0.75) alloys. The error bar in all the three panels represent the full width at half maxima (FWHM) at various ζ-values.

widths on the other hand varies from one alloy to another along the different high symmetry directions. The Cr-rich alloy tends to have a larger width (i.e. smaller phonon life-time) than the other two alloys. Being dominated by the force constant disorder, we expect augmented space recursion (ASR) to perform a good job (as done before [13] as well in case of Ni-Pt alloy) in capturing the essential off-diagonal disorder in the present case. The advantage of ASR over the other approximate theories (VCA or single-site CPA) is more significant if one look at the feature of phonon dispersion at higher wave-vectors, where the improper inclusion of disorder

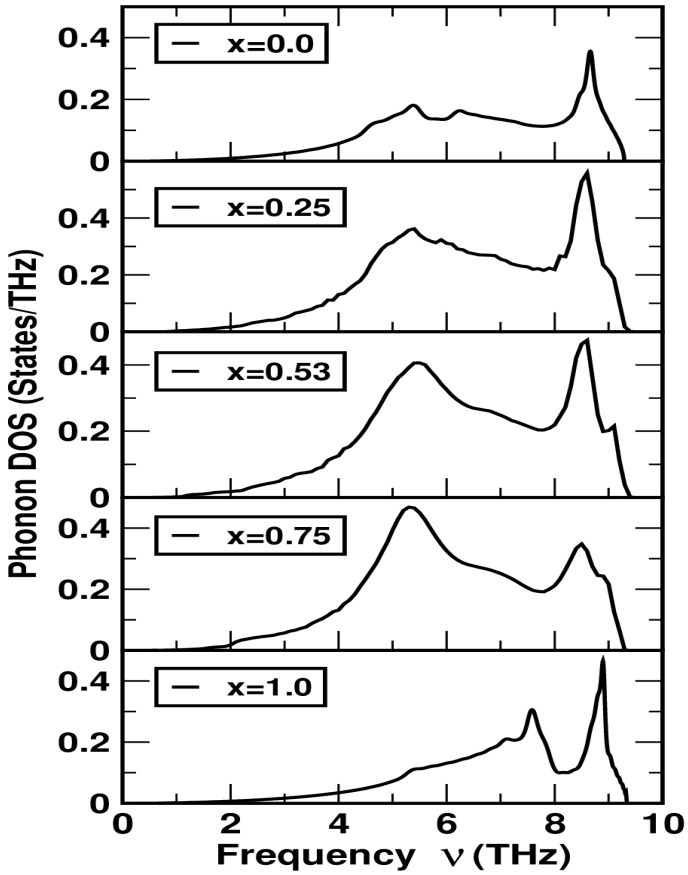

Figure 2.4: Phonon DOS for pure bcc Fe, bcc Cr and the three $Fe_{1-x}Cr_x$ ($x = 0.25, 0.47$ and 0.75) alloys.

effect in other theories deviate the dispersion curves lower in frequency and away from the one calculated from ASR (as well as those measured). The distinction in the low wave-vector regime is not that big, because the self averaging of both masses and force constants over a single wavelength reduces the result of ASR or any other accurate theory to become close to VCA.

The phonon DOS for the three alloys along with those of pure bcc Fe and bcc Cr are shown in Fig. 2.4. As reflected by the dispersion curves, the phonon DOS for all the three alloys resemble much more the phonon DOS of bcc Fe than that of bcc

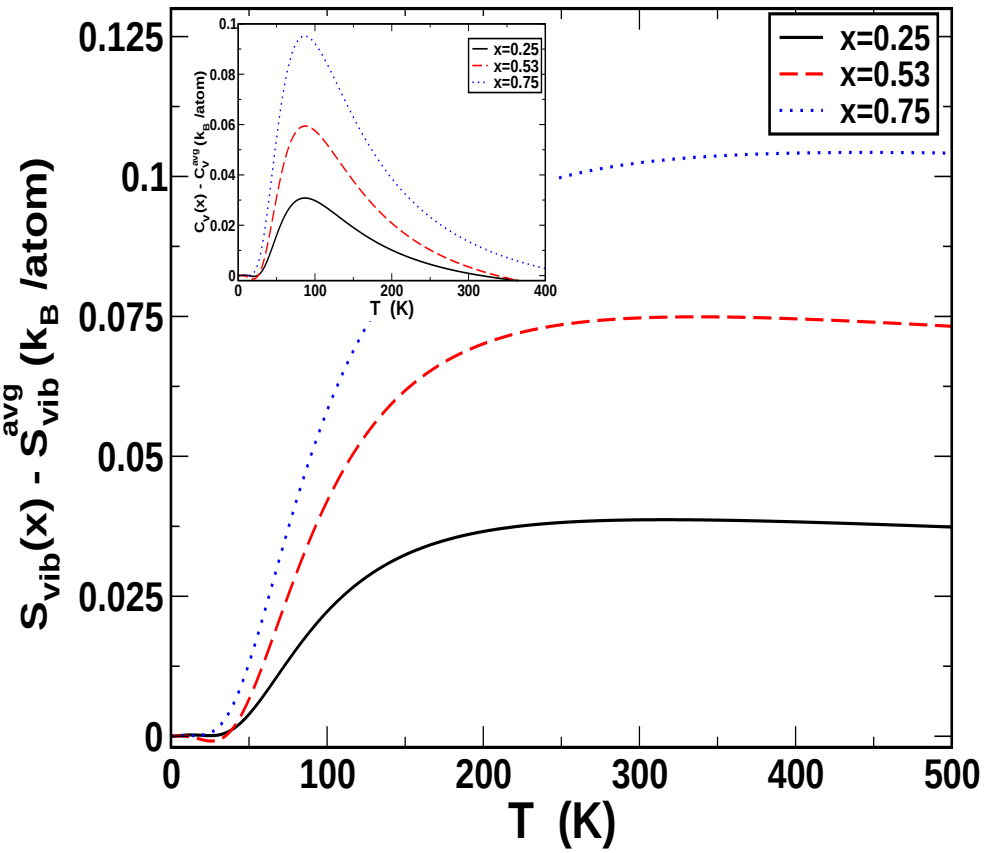

Figure 2.5: (Color Online) Temperature dependence of phonon entropy of mixing $\Delta S_{\rm vib} = S_{\rm vib}(x) - [xS^{\rm Cr}_{\rm vib} + (1-x)S^{\rm Fe}_{\rm vib}]$ for the three $Fe_{1-x}Cr_x$ alloys. The inset shows a similar estimate of the difference in lattice heat capacity $\Delta C_{\rm v}(x)$ between the alloy with composition x and the corresponding chemically unmixed state.

Cr. The overall shape of the phonon DOS curves calculated in the present work is similar to the previous findings [22, 15] for almost similar alloy composition. Since the change in the phonon DOS as Cr is added to bcc Fe is rather small, so there should in fact be little difference in the integral $\int_0^\infty n(\nu)ln(\nu)d\nu$ for bcc Fe and that of the three alloys. This will be shown more explicitly by our data on the vibrational entropy for these set of alloys.

The temperature dependence of the vibrational entropy of mixing for the three

$Fe_{1-x}Cr_x$ alloys are shown in Fig.2.5. This entropy difference is calculated by using Eq. 1.19, where $S_{\rm vib}(x)$ (β-state) is the vibrational entropy of the alloy with composition x, and $S_{\rm vib}^{\rm avg}(\beta'$-state) is the average of the chemically unmixed state of bcc Fe and bcc Cr weighted by the factors 75 : 25, 53 : 47 and 25 : 75 for the alloys $Fe_{75}Cr_{25}$, $Fe_{53}Cr_{47}$ and $Fe_{25}Cr_{75}$ respectively. The inset shows a similar estimate of the difference in lattice heat capacity between each of the bcc Fe-Cr alloy and the corresponding chemically unmixed state. it is immediately clear from the inset that the specific heat curves have similar shapes, but increases in weight with the concentration of Cr. Because of the similar shape of the phonon DOS curve of alloy as that of the DOS curve for pure Fe, a linear scaling of $\Delta C_{\rm v}(T)$ with the Cr-concentration x is expected. In the moderate temperature limit, we obtained $\Delta S_{\rm vib}(T)$ to be 0.033 k_B/atom and 0.039 k_B/atom for $Fe_{75}Cr_{25}$ alloy at 150 k and 300 K respectively. These entropy difference for $Fe_{53}Cr_{47}$ alloy are 0.062 k_B/atom and 0.075 k_B/atom, and for $Fe_{25}Cr_{75}$ alloy are 0.107 k_B/atom and 0.132 k_B/atom at respective temperatures. These values are smaller than those obtained experimentally [22, 16].

How can we explain the apparent discrepancy between our findings (smaller entropy difference) and the results from inelastic neutron scattering [22, 16]? One of the reason for such a discrepancy is the so called neutron weighting problem [16] in the calculation of phonon DOS in inelastic neutron scattering measurements. For alloys, different alloy components have different efficiencies for phonon scattering, which are proportional to the ratio of their neutron scattering cross sections σ_{sc} to their atomic mass. The displacements of different atoms in different phonons usually have different amplitudes, so different phonons may be over or under represented in a DOS directly obtained from experimental measurements. This distortion of phonon DOS should be corrected to get a reliable estimate of vibrational entropy. In fact for Fe-Cr alloy, the

phonon scattering from natural Fe is approximately three times stronger than that from natural Cr i.e. $\sigma_{\rm sc}^{\rm Fe}/m_{\rm Fe} \simeq 3\ \sigma_{\rm sc}^{\rm Cr}/m_{\rm Cr}$. Such a neutron-weighting problem has been investigated recently [16] for Fe-Cr alloy, and an attempt has been made to avoid such a problem by estimating a neutron weight-corrected phonon DOS. As a matter of fact, phonon entropy of mixing calculated from the neutron weight corrected DOS is smaller than those evaluated from the directly measured DOS. This is an indication of the right trend of our calculated phonon entropy of mixing if the measured phonon DOS accurately takes into account the effect of different efficiencies of phonon scattering for alloy components. A related reason for the mentioned discrepancy can be attributed to the use of the virtual crystal approximation (VCA) for analyzing the coherent inelastic neutron scattering data from chemically disordered alloys. The VCA does not allow for high frequency vibrations in disordered alloys at the frequencies of optical modes in the ordered alloys. It, therefore, may overestimate the change in phonon DOS upon chemical ordering. In addition, it has also been mentioned by Fultz *et al.*[22] that the absolute error in the value of vibrational entropy of mixing ($\Delta S_{\rm vib}$) obtained from their inelastic neutron scattering experiment can be as large as 0.05 k_B/atom. Keeping this error in mind, our theoretical phonon entropy of mixing then lie on the same ball part as that measured by them.

In order to understand the general trend of the phonon entropy of mixing with varying alloys, we shall next make a connection with a more intrinsic quantity, the so called full widths at half maxima (FWHM) associated with the disorder-induced lifetime broadening of the phonon groups. Life time broadening is a consequence of the local vibrational modes mainly arising out of the disorder in the inter-atomic force constants. Fig. 2.6 shows the FWHM as a function of the wave-vector magnitude ($|\zeta|$) along the high symmetry directions for the three bcc $Fe_{1-x}Cr_x$ alloys. One

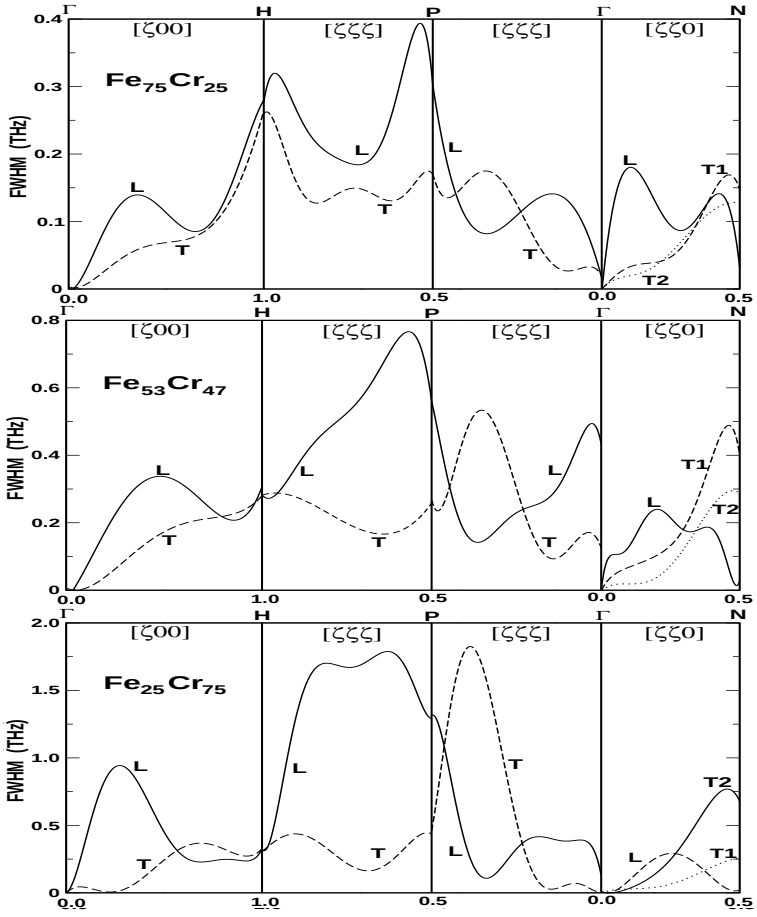

Figure 2.6: Disorder induced Full Widths at Half Maxima (FWHM) along the high symmetry directions for three $Fe_{1-x}Cr_x$ ($x = 0.25, 0.47$ and 0.75) alloys.

can easily notice that the disorder broadening increases quited rapidly as we move towards the Cr-rich alloy. For example the maximum value of line-width along H-P direction for $Fe_{75}Cr_{25}$ alloy is $\simeq$ 0.4 THz, however it increases to $\simeq$ 0.78 THz for $Fe_{53}Cr_{47}$ alloy and increases further to $\simeq$ 1.85 THz in case of $Fe_{25}Cr_{75}$ alloy. A damped harmonic oscillator function fit to the two phonon groups (one along [100] and the other along [111]) for $Fe_{53}Cr_{47}$ alloy has been made by Fultz *et.al.*[22]. They estimated a resonance width of 0.2 THz for [100] $Q = 0.5$ phonon group and 0.96 THz

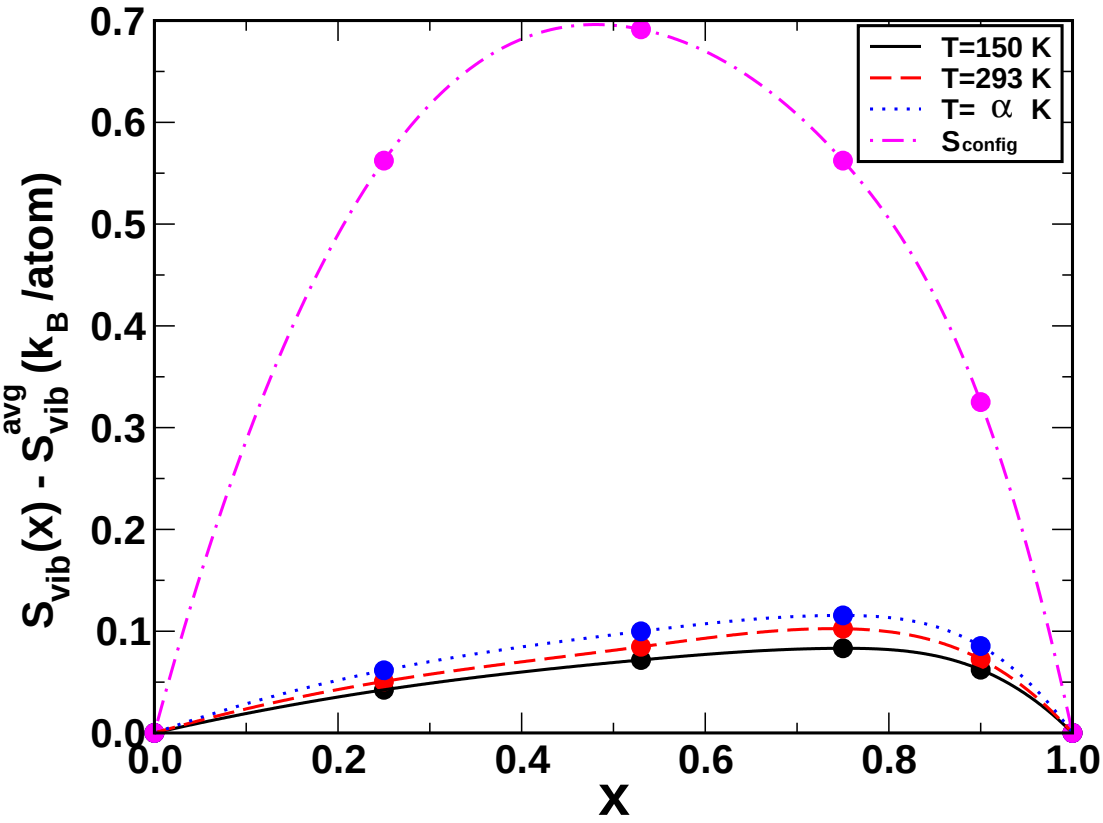

Figure 2.7: (Color Online) Concentration dependence of phonon entropy of mixing $\Delta S_{\rm vib}(x)$ at various fixed temperature. The high temperature (T$\rightarrow \infty$) limit of $\Delta S_{\rm vib}(x)$ is calculated from Eq. 1.20. Composition dependence of the configurational entropy (indicated by magenta dot-dashed line) for the fully random solid solution is also shown to compare the relative magnitude of the phonon entropy of mixing.

for [111] $Q = 0.6$ phonon group. We obtained a similar estimate for the widths for $Fe_{53}Cr_{47}$ alloy. Broadened peaks were also observed for phonons near Brillouin-zone boundaries.

Usually the line broadening of the phonon groups is more if the strength of the disorder is more, which causes smearing of the sharp features in the phonon DOS curves for the alloys. Such a smoothening of the vibrational energy spectrum will have benign consequences on the phonon entropy calculation provided the phonon

structure factors are broadened neither too asymmetrically nor excessively towards low frequencies. The phonon line shapes in our calculation for $Fe_{75}Cr_{25}$ and $Fe_{53}Cr_{47}$ came out to be quite symmetric except in some of the higher frequency regime. The line shapes for Cr-rich $Fe_{75}Cr_{25}$ alloy are comparatively less symmetric with a larger disorder broadening. Keeping in mind the magnitude of calculated vibrational entropy difference for the three alloys as quoted before and looking at the FWHM for the same three alloys in Fig. 2.6, one can arrive at a conclusion that the disorder broadening of the phonon groups tend to increase the phonon entropy of mixing. Such a theoretical prediction has also been supported by previous experimental investigations [22].

In Fig. 2.7, we display the phonon entropy of mixing as a function of alloy composition (x) at different temperatures (T). The high temperature limit of ΔS_{vib} were obtained from Eq. 1.20 and are shown by blue-dotted curve. The configurational entropy of the fully random solid solution is also plotted to show the relative magnitude of the phonon entropy.

It is expected intuitively that all thermodynamic functions should change monotonically during spinodal decomposition. A smooth change occurs for configurational entropy for example. However, due to the small changes in phonon DOS curve, the phonon entropy will not change significantly during the early stages of spinodal decomposition. For the Fe-Cr alloy, the transition of the shape of phonon DOS curve from being Fe-like to Cr-like occur at high Cr-concentration. Therefore, vibrational entropy affect differently the solubility of Fe in bcc Cr-rich phase compared to the solubility of Cr in bcc Fe-rich phase. Although this asymmetry does not occur for the configurational entropy of mixing, the phonon entropy has a different dependence on composition (x) and hence the reason for an asymmetric curve in Fig. 2.7. This is precisely the reason that the inclusion of vibrational entropy into the alloy thermody-

namics alter the shapes of phase boundaries, and not simply re scale the temperature of the miscibility gap. The critical temperature and composition of the miscibility gap in Fe-Cr are 905 K and $x = 0.51$ respectively. [41] As a matter of fact, it has been found that, in the absence of phonon entropy of mixing, the miscibility gap shifts up in temperature and towards pure Cr, with a critical temperature and composition of 1208 K and $x = 0.64$ respectively. Thus the role of phonon entropy is to lower the critical temperature of the miscibility gap and shift it towards the equiatomic composition.

2.4.2 Short Range Ordering Effect in Fe-Cr alloy

Here we investigate the effect of local chemical environment on the vibrational properties of bcc $Fe_{50}Cr_{50}$ alloy. The effect of local environment will be studied via the Warren-Cowley short-range order (SRO) parameter. The existence of inter-metallic phases in compounds is a consequence of the strong ordering tendency of the alloy. The same driving forces, in various systems, make the alloy exhibit chemical short-range order (SRO) in that phase. Depending on the system of interest, the chemical SRO might result a complete ordering or a phase segregating tendency or even a combination of the two. Although there exist few experimental work [23, 42] to study the effects of local chemical environment on the lattice dynamics of disordered alloys, a reliable theoretical understanding of the same from a first-principles calculation is still lacking. The present investigation is undertaken to analyze the effects of local atomic environment (via the warren-cowley SRO parameter α) on three basic lattice dynamical properties, namely, phonon DOS, vibrational and configurational entropies within a first-principles calculation.

Fig.2.8 shows how the phonon density of states for a $50-50$ Fe-Cr alloy changes as

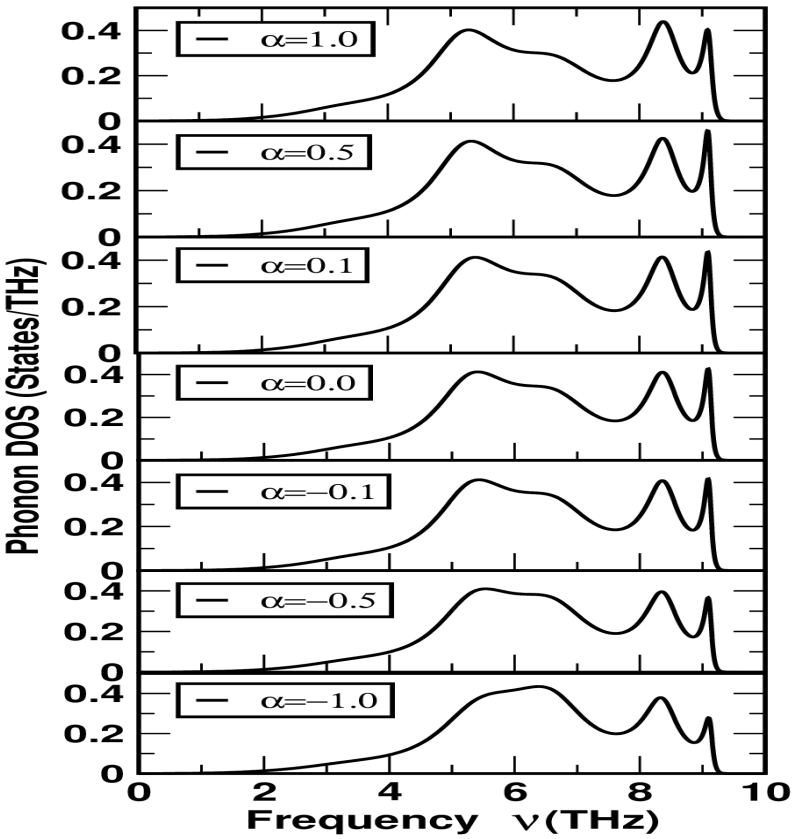

Figure 2.8: Local chemical environmental effect on the Phonon density of states (DOS) of $Fe_{50}Cr_{50}$ alloy. The phonon DOS of fully random solid solution ($\alpha = 0$) is also plotted for the sake of comparison. The local environmental effect is dictated via the warren-cowley short-range order parameter (α). $\alpha = -1$ indicates an ordering tendency, $\alpha = +1$ indicates a clustering (phase segregating) tendency and $\alpha = 0$ corresponds to a fully random solid solution with no SRO

a function of the Warren-Cowley short-range order parameter (α). The two extreme limits $\alpha = -1$ and $+1$ corresponds to the tendency towards ordering and phase segregation respectively. The DOS for the completely random (homogeneously disordered) alloy ($\alpha = 0$) is also shown for the sake of comparison. It is clear from the figure, that the alloys show moderate differences in DOS for samples with chemical short-range order. A general connection between the phonon DOS and chemical short-range order may be made from the slopes of the phonon dispersion curves. A high density

of phonon states is obtained from a flat dispersion curves, especially when they include Brillouin-zone boundaries. They also provide a slow group velocity of sound. Much of the energy of lattice vibrations is associated with localized atomic movements for slowly propagating phonon wave packets. The SRO affect these localized atomic movements quite strongly and hence have a major effect on the corresponding regime of the phonon DOS. Those parts of the phonons DOS not associated with the flattened dispersion curves should be less sensitive to SRO. Based on these arguments, one can easily notice from Fig. 2.8 that the phonon DOS in the frequency range ($\simeq 4.5 - 7$) THz are mainly arising from the contribution of flat parts of the dispersion curves, and hence are influenced by SRO more strongly than the feature of the DOS beyond $\simeq 7$ THz.

It is even more interesting to look at the effects of SRO on the entropy of mixing. In the lower panel of Fig. 2.9, we display how the vibrational entropy of mixing in the high temperature limit ($T \geq \Theta_{\mathrm{Debye}}$) varies with the short-range order parameter (α) for a $50 - 50$ Fe-Cr alloy. For comparison sake, we also plotted the short-range order variation of the configurational entropy (Upper panel) as calculated from Eq. 2.13 (including only the first nearest-neighbor shell SRO effect $\alpha = \alpha_1$). The small variation of phonon DOS curve as a function of SRO parameter is also reflected in the phonon entropy of mixing. For the homogeneously disordered ($\alpha = 0$) $Fe_{50}Cr_{50}$ alloy, the phonon entropy of mixing came out to be 0.094 k_B/atom. However, in different local chemical environment, the phonon entropy of mixing ranges from 0.082 k_B/atom (for $\alpha = -1$) to 0.101 k_B/atom (for $\alpha = +1$), which is not a big change compared to the completely random solid solution. The dependence of phonon entropy of mixing on the local arrangement of atoms delivers a deeper insight to the understanding of thermodynamic stability of complex alloys.

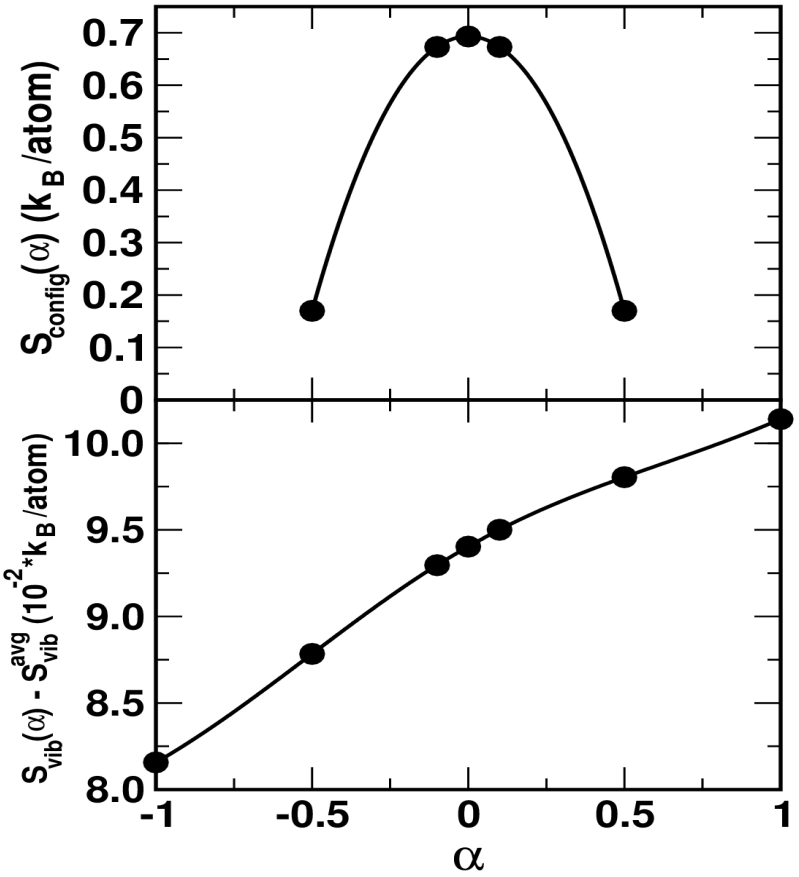

Figure 2.9: SRO dependence of the configurational and phonon entropy of mixing for a disordered $Fe_{50}Cr_{50}$ alloy.

As obvious from the phonon DOS curves (See Fig. 2.8) for the three $Fe_{1-x}Cr_x$ alloys, the total DOS looks very similar to that of bcc Fe than bcc Cr. Unfortunately, we do not exactly know the concentration above 75 at. % of Cr for which the phonon DOS changes from being Fe-like to Cr-like. However at low concentrations of Fe in a Cr-host, there is a substantial distortion of the Fe partial DOS (PDOS) curves compared to pure bcc Fe. The PDOS of both Fe and Cr atoms undergo an average softening upon alloying, which leads to a net +ve phonon entropy of mixing, but with a net softening of Cr PDOS to be larger than that of Fe. At low concentrations of Fe

in Cr, this larger softening of Cr PDOS curves causes the phonon entropy of mixing to increase rapidly with Fe concentration, yielding a skewed shape of the concentration dependence of phonon entropy (See Fig. 2.7). The interplay of such softening of phonon modes in alloys with short-range order is even more dramatic, because in this case the total phonon entropy of mixing is not just affected by the different entropic weights of their atomic species, but also by the nature of correlated disorder present in the short-ranged clusters considered.

The main reason behind investigating the SRO dependence of the phonon DOS and phonon entropy in this work was to satisfy ourselves and at the same time provide a validation for our correct smaller value of phonon entropy of mixing compared to other findings. It was our intuition that SRO effect might enhance the magnitude of phonon entropy of mixing to bring it closer to other findings, but we figured out that, that's not the case at least in case of Fe_{1-x} Cr_x alloy. And the reason we gave in the previous subsection IV(A) for the comparatively smaller value of our calculated phonon entropy is indeed valid. While this result does not restrict the possibility that SRO play an important role in the lattice dynamics of alloys in other systems, it does indicate that the local environmental effects in Fe-Cr alloy may not be that significant.

2.5 Case 2: $\mathbf{Re_{1-x}W_x}$ alloy (x=0.29, 0.43, 0.75)

For this alloy too, we have used a first-principles derivation of the dynamical matrices we have used the *ab-initio* Quantum-Espresso code. We estimated Re-Re, W-W and W-Re, Re-W dynamical matrices from the ordered bcc and B2 structures respectively, by density functional perturbation theory (DFPT). The calculations were done at the alloy equilibrium lattice constants.

Dynamical Matrix $D_{\mu\nu}(\|R\|)$						
Direct.	Distance (in units of a)	$x = 0.75$	$x = 0.43$	$x = 0.29$	$x = 0$	$x = 1$
		Newton/meter				
111xx	0.866	5.556	5.852	7.274	3.961	23.200
111xy	0.866	27.732	30.571	32.099	31.339	19.500
200xx	1.000	40.876	45.572	47.194	8.306	47.800
200yy	1.000	7.411	8.267	8.851	2.052	-1.100

Table 2.1: Dynamical matrices calculated from first-principles for the $Re_{1-x}W_x$ alloys. The data for pure W is taken from the paper by Chen *et.al.*[43]

Actually, the alloys we are currently looking at are disordered and to a good approximation this is a valid procedure. However, if accuracy demands that the dynamical matrices be calculated from large super-cells with random occupation of sites by atoms, we have to do so instead of our present calculations. As mentioned earlier, the calculations were done at the alloy lattice constants: a=5.871 a.u. for $Re_{25}W_{75}$, a=5.840 a.u. for $Re_{57}W_{43}$ and a=5.812 a.u. for $Re_{71}W_{29}$. Vanderbilt ultra-soft pseudo-potentials with nonlinear core corrections were used. Convergence was checked with respect to the kinetic energy cutoff, which for wave-function comes out to be $\sim$ 35 Ry and that for the charge density and potential is $\sim$ 100 Ry. Spin polarized calculation with magnetization along z-axis was carried out to get better force constants for this metallic system. The Brillouin zone integration was carried out with Gaussian smearing using a $14\times14\times14$ k-point Monkhorst-Pack grid with grid displaced by half the grid space in the corresponding direction. The value of smearing parameter was 0.02 Ry. Once the electronic structure calculation is converged within the desired accuracy, the force constants were obtained first in reciprocal space on a $4 \times 4 \times 4$ Monkhorst-Pack grid. Then a Fourier transform led to the real space force constant. The masses of Re and W were taken to be 186.21 and 183.84 amu and their scattering lengths 9.2 and 4.86 fm, respectively.

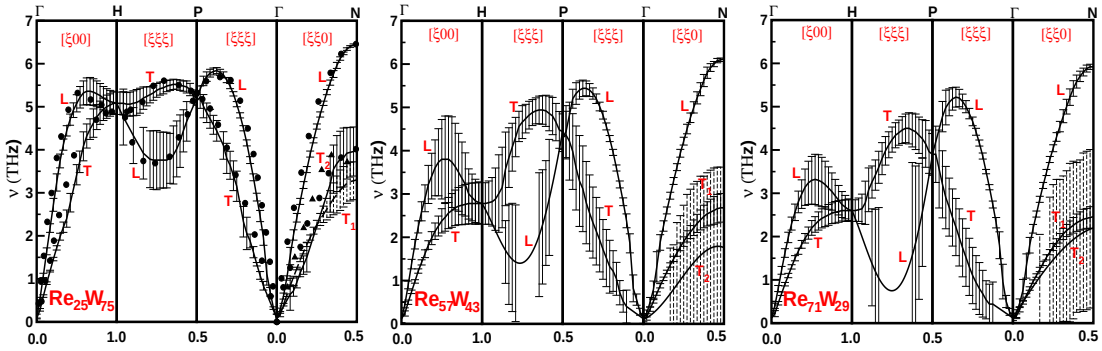

Figure 2.10: (Color Online) Phonon dispersion curves for three $Re_{1-x}W_x$ alloys ($x = 75, 43$ and 29 %) along the high symmetry directions of the bcc Brillouin zone (BZ). Error bars in all the panels represent our calculated full widths at half maxima (FWHM). Filled symbols in the left panel are the cluster expansion results for $Re_{25}W_{75}$ from Persson *et* al.[31]

Table 2.1 shows the calculated nearest neighbor ({111xx}, {111xy}) and next nearest neighbor ({200xx}, {200yy}) dynamical matrices for the pure Re and W ($x = 0$ and 1) and those of the three $Re_{1-x}W_x$ alloys. One can notice the dramatic changes in the values of the force constants in alloys due to the different nature of effective embedded medium in different alloys. B2 ordering can be considered as one of the configuration out of various configurations in the actual random alloy. Within a B2 ordering, the nearest neighbor ({111xx}, {111xy}) of a central A-atom is a B-atom and the next nearest neighbor ({200xx}, {200yy}) is an A-atom itself. As such, one can compare the next nearest neighbor A-A force constants (f.c.) in the alloys with the same in the pure A-element itself. For example {200xx} f.c. in pure Tungsten changes from 47.8N/m to 45.57 N/m in $Re_{57}W_{43}$, while {200yy} f.c. changes from -1.1 to 8.2 N/m. Thus the screening effects (due to a Re-atom at the nearest neighbor site) in the $57 - 43$ alloy is quite significant along the {200yy} direction. The effects in other two alloys are even more significant due to a very different nature of the random environment around each sites.

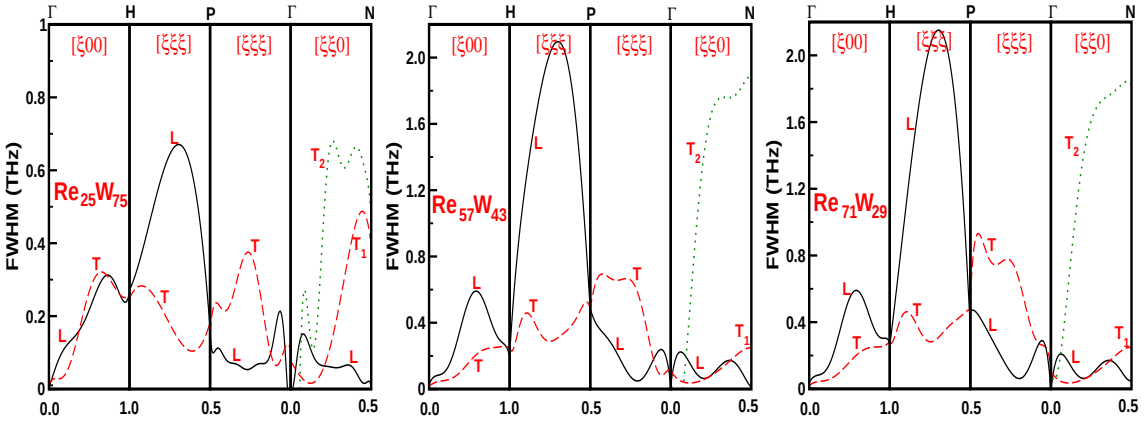

Figure 2.11: (Color Online) Full widths at half maxima (FWHM) for three $Re_{1-x}W_x$ alloys ($x = 75, 43$ and 29 %) along the same high symmetry directions as in Fig. 2.10.

2.5.1 Results and discussions

Phonon dispersion curves for the three $Re_{1-x}W_x$ alloys are calculated from the coherent structure factors (CSF) $S_{coh}(\mathbf{k},\omega^2)$. In the absence of disorder the CSF has poles on the real frequency axis and exhibits delta function peaks at $\nu_0(\mathbf{k}) = \omega_0(\mathbf{k})/2\pi$. In the presence of disorder, when we have the self-energy Σ (as shown in Eq. 1.15), the peaks shift to $\omega_0 + Re[\Sigma(\mathbf{k}, \omega_0^2)]$ and are broadened by a width $\Im m[\Sigma(\mathbf{k}, \omega_0^2)]$. We usually locate the peak positions numerically to plot the phonon dispersion and fit a Lorentzian function in the vicinity of the peaks to extract the full widths at half maximum (FWHM). Depending on the complex interplay between the mass and force constant matrices of the concerned alloy, the CSF function can be very different compared to a simple lorentzian e.g. doubly peaked structure, significantly broadened in certain **k**-range etc. as shown in an article [13] on NiPd alloy.

Figure 2.10 shows the phonon dispersion curves for the three $Re_{1-x}W_x$ alloys along the high symmetry directions of the bcc Brillouin zone. L and T's indicate the longitudinal and transverse modes. Within a bcc symmetry, transverse modes are

degenerate except along the [$\xi\xi$0] direction. The error bars in all the three panels represent our calculated full widths at half maxima (FWHM) at various values of **k**. Filled symbols in the left panel indicate the cluster expansion results by Persson *et.al.*[31] We could not find any other theoretical or experimental data on this system. There are some discrepancy along the direction Γ-N which may be due to the different way of handling the off-diagonal disorder in the two methods. Interestingly, however, the results from cluster expansion in all the directions lie within the error bar of our calculation. We find that the effects of disorder-induced scattering is much stronger in the Re-rich alloys compared to that in the W-rich ones, which is evident from the larger FWHM's (smaller scattering length) in the middle and the right panels. For visualization purpose, we have shown the FWHM's of the T_2 modes along the [$\xi\xi$0] direction by dashed error bars. Due to the highly asymmetric nature of the CSF along H-P directions, we cannot find enough data points for the longitudinal modes in this direction, we have therefore fitted a polynomial to these points only for the L-modes. Interestingly, the gross feature of the dispersion for all the three alloys, resemble each other and that of pure Re as well. The disorder-induced line-widths on the other hand varies from one alloy to another along the different high symmetry directions. This is clearly evident in Fig. 2.11, which shows the FWHM's vs the wave vector along the same high symmetry lines as in Fig. 2.10.

We note that as we go from Re concentration 0.25 to 0.71, the FWHM of some of the branches increase drastically, e.g. longitudinal mode in H-P direction and the T_1 and T_2 modes in the Γ-N direction. This points towards the possible instability of the bcc phase which is already seen in experiments [30]. Such a drastic change (increase) in the FWHM arise due to a stronger **k**-dependence of the phonon self-energy $\Sigma(\mathbf{k}, w^2)$ for these particular modes. The frequency dependence of the phonon

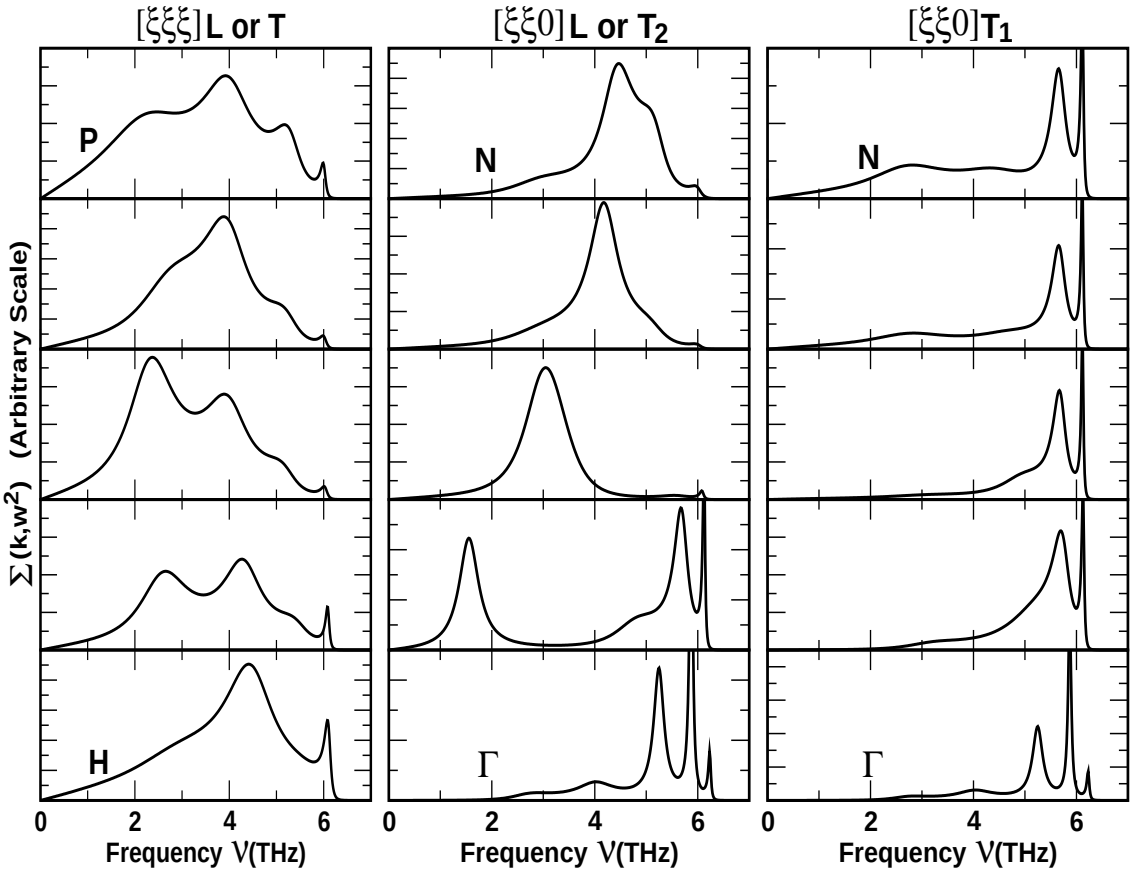

Figure 2.12: **k**-dependence of the imaginary part of the phonon self energy $\Sigma(\mathbf{k}, w^2)$ along [ξξξ] (H to P) and [ξξ0] (Γ to N) directions for $Re_{57}W_{43}$ alloy.

self-energy for various **k**-values along the [ξξξ] and [ξξ0] directions for $Re_{57}W_{43}$ is shown in Fig. 2.12. One can notice rapid changes in the shape of of $\Im m[\Sigma(\mathbf{k})]$ as we go from H-point to P-point (along [ξξξ]) and Γ to N-point (along [ξξ0]). This is in complete contrast to the CPA-based self energy which is shown to be **k**-independent. This is due to the single-site, mean-field nature of the CPA which is unable to capture the multi-site effects as is essential for the phonon problem.

The phonon DOS for the three alloys as well as the pure bcc Re and W are shown in the left panel of Fig. 2.13. As reflected by the dispersion curves, the main effect of

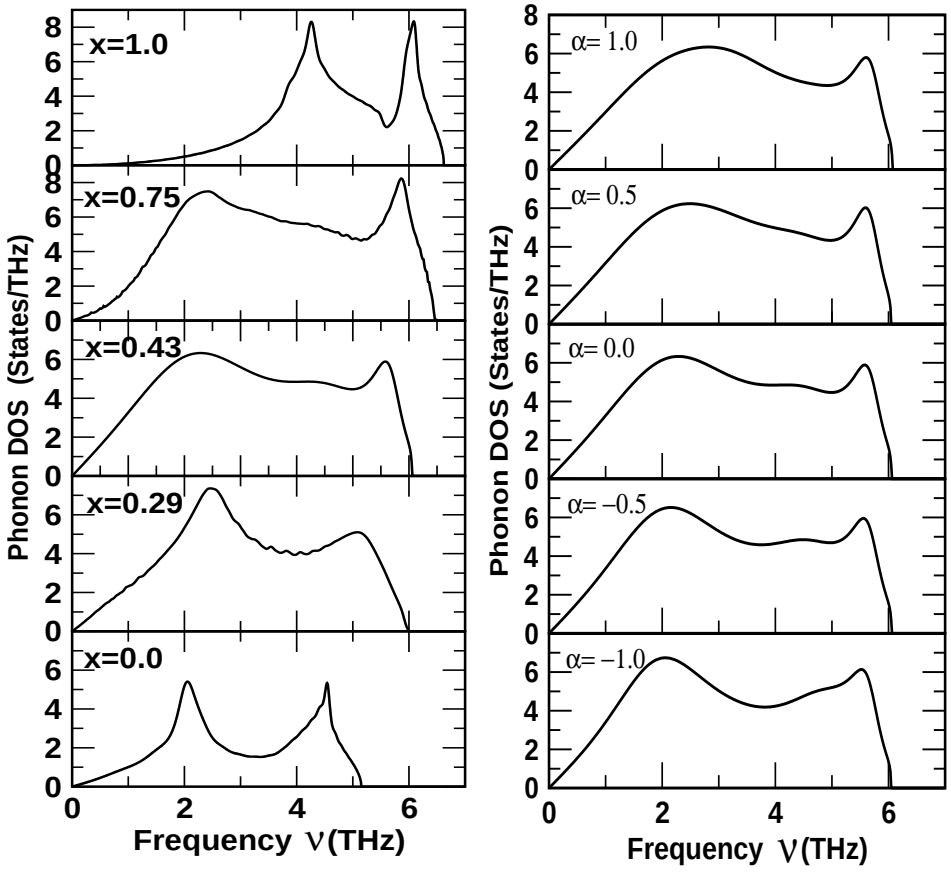

Figure 2.13: Phonon density of states for $Re_{1-x}W_x$ alloys, (Left) $x = 1.0$ to 0.0 (top to bottom) (Right) at x=0.5 with SRO parameter α (see Ref. [45]) varying from 1 to -1.

alloying with W is to smear out some of the sharp features of pure DOS and rearrange the right hand peak. As the concentration of W increases, the prominent right peak of the DOS at around 6 THz begins to show up. The effect is of course maximum for the most concentrated alloy with x=0.43. Now, because of the rather small change in the overall shape of the phonon DOS as W is added to bcc Re, there should be little difference between the integral $\int_0^\infty n(\nu)ln(\nu)d\nu$ for the composition averaged DOS and those for the corresponding three alloys. This will be evident from our results on the specific heat and vibrational entropy for these set of alloys.

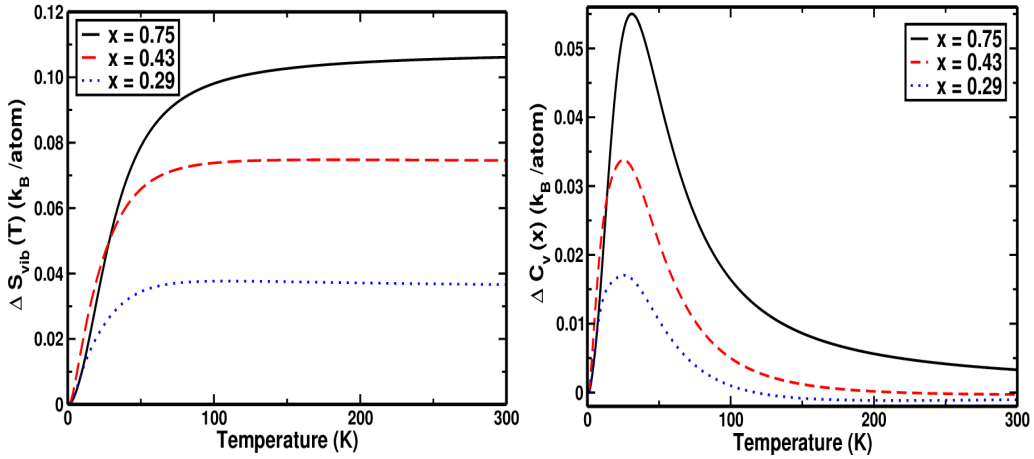

Figure 2.14: (Color Online) (Top) Temperature dependence of the vibrational entropy of mixing $\Delta S_{vib} = S_{vib}^{Alloy}(x) - [xS_{vib}^{W} + (1-x)S_{vib}^{Re}]$ for the three $Re_{1-x}W_x$ alloys. (Bottom) A similar estimate of the difference in lattice heat capacity ΔC_v.

The right panel of Fig. 2.13 shows the effect of short-ranged order on the alloy with x=0.5. As the Warren-Cowley parameter α traverses in value from 1 to -1, we go from complete segregation to local B2 ordering. When local order/segregation has set in, we still have background disorder. The situation resembles that of clusters embedded in a disordered medium. The remaining disorder provides the smoothing of the DOS. Although the overall structure of the DOS does not seem to change appreciably with the SRO, however such a small change is sufficient to induce a local ordering from a completely segregated phase.

The temperature dependence of the vibrational entropies of mixing for the three $Re_{1-x}W_x$ alloys are shown in the top panel of Fig. 2.14. The figure in the bottom panel shows a similar estimate of the difference in lattice heat capacity between each of the bcc Re-W alloys and the corresponding chemically unmixed states. It is immediately clear from the figure that the specific heat curves have similar shapes, but decreases in weight with the decrease in W-concentration. This is a reflection of

the similar shapes of the phonon DOS curves as in Fig. 2.13. In the large T-limit, the vibrational contribution to the entropy increases with concentration x. This is due to an extra weight (in Eq. 2.5) arising out of the difference in phonon DOS between the alloy and the chemically unmixed state. Phonon contribution of the Tungsten states are mainly responsible for such increase in both the ΔC_v and the ΔS_{vib} of the alloy. The intrinsic harmonic diffusion of higher energy delocalized vibrations are mostly responsible for the relevant dominant mechanism in such instances.

Another important result we noticed that the sudden increase in the life-times of certain bands, as the concentration of Re increases beyond 27%, had indicated that the corresponding bands destabilizes and precurses structural phase transitions. It is known that alloys in this composition range are unstable. An stability analysis must include the vibrational entropy along with the configurational entropy. Unlike the previous case of FeCr we do not have experimental data with which to compare. We suggest that relevant experiments should be carried out before a comparison can be made.

2.6 Concluding Remarks

We propose a combination of the first-principles Quantum-Espresso method (based on the density functional perturbation theory) and the ASR to investigate the lattice dynamics and the vibrational and configurational entropy of disordered alloys at any arbitrary concentration. A generalized formalism (within the ASR method) to include the effects of short-range order on the lattice dynamics has been derived and implemented on a bcc Fe_{1-x} Cr_x alloy for the first time. We studied three alloys Fe_{25} Cr_{75}, Fe_{53} Cr_{47} and Fe_{75} Cr_{25}, the phonon dispersion and phonon DOS of which were much more similar to those of pure bcc Fe than that of Cr. We obtained

a comparatively smaller value of phonon entropy of mixing (ΔS_{vib}) in contrast to the interpretations from previous experiments. However, in light of our results, the upper bounds of ΔS_{vib} obtained from inelastic neutron scattering data should be reinterpreted. The upper bound from the experiment is unlikely to be appropriate (i) due to the use of virtual crystal approximation (VCA) in analyzing their data and (ii) due to the incorrect neutron weighting caused by difference in phonon scattering efficiencies of the two elements. A connection with the life-time broadening of the phonon groups has been made to explain the trend of the magnitude of calculated ΔS_{vib}. A comparatively larger softening of the Cr partial DOS (compared to Fe) curves is found to be the reason behind the compositional asymmetry of the phonon entropy of mixing. The phonon entropy shifts both the miscibility gap towards the equiatomic composition and lowers the critical temperature by $\sim$ 300K. The effect of SRO did not come out to be significant in terms of the magnitude of phonon entropy of mixing, which we initially thought not to be the case. Understanding the magnitude of the phonon entropy variations between different states of a compound remains a central problem in any first-principles alloy theory. The effect of local arrangement of atoms on the phonon entropy provide an even higher level of details which we studied in the present work for Fe-Cr alloy. Although this effect came out to be small in the Fe-Cr alloy, it still remains of interest to evaluate the magnitude of this effect in other systems.

In case 2 study we presented a clear picture of the lattice dynamical properties of the random $\text{Re}_{1-x}\text{W}_x$ alloys within a first principles approach. The density functional perturbation theory (within the Quantum-Espresso code) is first used to generate the alloy dynamical matrices of the individual pairs of constituent atoms. Subsequently, using these dynamical matrices and the augmented space recursion,

we have studied phonon dispersion, densities of states, self energies, lattice specific heat and vibrational entropies. Phonon dispersion for the Re-rich alloys is found to be strongly fuzzy: an outcome of the highly asymmetric CSF with large disorder-induced broadening. Such a fuzziness in the phonon dispersion is actually related with the instability of the bcc phase in this composition range. This is also evident in experiments [30]. Unlike FeCr alloys, there are only a handful of relevant experimental works on $Re_{1-x}W_x$. We, therefore, suggest that such experiments should be carried out, because $Re_{1-x}W_x$, an alloy used in the core of thermonuclear reactors, is an extremely important material and a thorough understanding of its behavior is desirable.

Chapter 3

Thermal conductivity and diffusion-mediated localization in $Fe_{1-x}Cr_x$ Alloys

3.1 Introduction

In this chapter we introduced an important formalism we developed to study the configuration averaged lattice thermal conductivity and diffusivity for random alloys. We apply a Kubo-Greenwood-type formula combined with a generalized Feynman diagrammatic technique to carry out a first-principles calculation of the thermal transport properties of disordered $Fe_{1-x}Cr_x$ Alloys. The study of phonon excitations and the associated thermal transport properties is an important field of research in disordered alloys. In few materials, disorder mediated scattering can shrink the typical mean free path (MFP) of phonons to such a level that wavelength and MFP no

[0]The contents of this chapter has been published in two papers :

1. Aftab Alam, Rajiv K. Chouhan and Abhijit Mookerjee, *Phys. Rev.* **B 84**, 224309 (2011)
2. Rajiv Kumar Chouhan, Aftab Alam and Abhijit Mookerjee *Conference Proceedings of the 31st International Thermal Conductivity Conference and the 19th International Thermal Expansion Symposium 2011* (in press)

longer remain sharp concepts, and the usual textbook phonon gas model for thermal conductivity breaks down. From the theoretical perspective, the development of a reliable quantum mechanical theory to predict such properties in random alloys is a difficult task mainly because of two problems : (i) one needs a microscopic description of inter-atomic force constants with an intrinsic off-diagonal disorder and (ii) one has to configuration average a two-particle correlation function using a Kubo-type formula. The effects of dominant off-diagonal force constant disorder in alloys can be quite unusual, as being shown earlier [13] & [46]. Most theories of thermal transport, developed in the past few decades however, are either based on the single-site coherent potential approximation (CPA) [5], the perturbation-based approach simulating the Peierls-Boltzmann equation (PBE) [47] or atomistic models with a large unit cell and periodic boundary conditions [48]. CPA, being a single-site mean-field approximation, is inadequate for treating multi-site off-diagonal disorder arising out of force constants. The CPA is unable to adequately explain experimental life-time data on simple Ni-Pt alloys [49]. The perturbative simulation approach, although rigorously derived, is limited in applicability to model lattices alone and has not been tested on realistic materials. The atomistic models are computationally expensive due to the large unit-cell size, non-self-consistent and suffer from the finite size errors.

Recent work by Aftab *et.al.*[50] demonstrated a theoretical approach to calculate the configuration averaged lattice thermal conductivity and diffusivity for random alloys. This formalism combined a Kubo-Greenwood approach with a generalized Feynman diagrammatic technique to explicitly incorporate the effect of disorder induced scattering. We showed that disorder scattering renormalizes both the phonon propagators as well as the heat currents. These corrections are related to the self-energy and vertex corrections. Unlike the single-site CPA, this approach explicitly

takes into account the fluctuations in masses (diagonal), force constants and heat currents (off-diagonal disorder) between different ion-cores and incorporates the sum rule relating the diagonal element of the force constant to the off-diagonal ones.

We find that the disorder induced scattering effects on the thermal conductivity, $\kappa(T)$, is relatively large in the low frequency regime. $\kappa(T)$ shows a quadratic T-dependence in the low temperature range, where only low energy vibrations are excited, and then smoothly rises to a T-independent saturated value at high T. Thermal diffusivity manifests the effect of disorder in a more dramatic fashion, and gives an idea about localization. Based on our calculation on $Fe_{1-x}Cr_x$ alloys, a large fraction (> 90 %) of vibrational eigenstates are found to be localized with the maximum localization near 50-50 composition, where the disorder scattering is maximum, as expected.

3.2 Thermal Transport properties in disordered alloy

For disordered materials, the lattice thermal conductivity requires the configuration average of the response functions of the kind see [50],

$$\langle\langle \kappa(z_1, z_2, T)\rangle\rangle \;=\; \int \frac{d^3\mathbf{k}}{8\pi^3} \mathrm{Tr}\left[\langle\langle \mathbf{S}(\mathbf{k}, T)\mathbf{G}(\mathbf{k}, z_1)\mathbf{S}(\mathbf{k}, T)\mathbf{G}(\mathbf{k}, z_2)\rangle\rangle\right], \tag{3.1}$$

where $\mathbf{S}$ is the heat current operator and $\mathbf{G}$ is the phonon propagator.$\langle\langle\ \ \rangle\rangle$ denotes configuration averaging.

The right hand side of (3.1) involves the configuration average of four random functions whose fluctuations are correlated. Unlike the configuration average of a single particle Green function $\langle\langle \mathbf{G}(\mathbf{k}, z)\rangle\rangle$, which can be calculated via a perturbative self-consistent Dyson's equation (shown diagrammatically in the 1st row of Fig. 3.1),

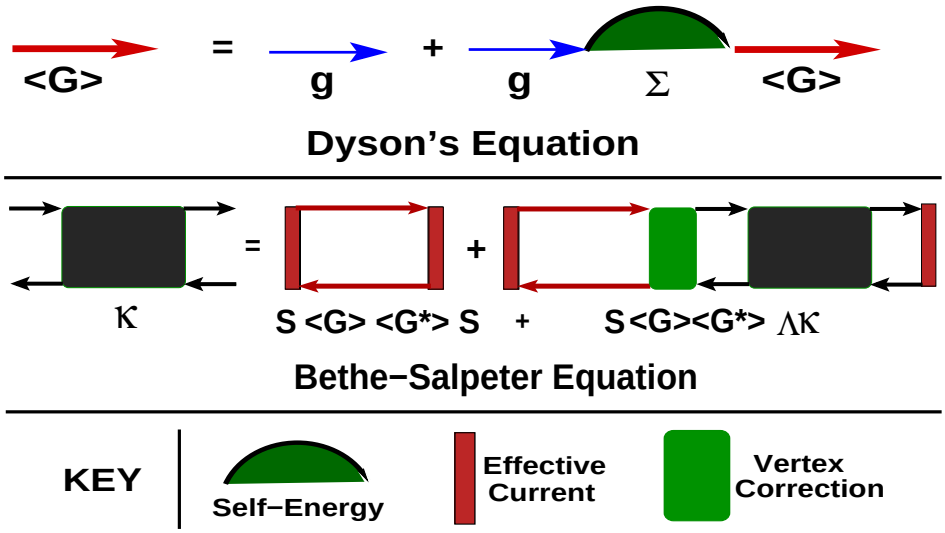

Figure 3.1: (Color Online) (Top row) Dyson's Equation due to scattering diagrams for the single particle averaged Green's functions for disordered alloys. (Middle Row) Bethe-Salpeter equation for the response functions in disordered alloys. (Bottom Row) Key to diagrams. $< \mathbf{G} >$ is the averaged disorder renormalized Green's function, $< \kappa >$ is the two-particle correlation function related to Thermal conductivity, Σ is the self energy and $\mathbf{S}$ is the disorder-renormalized effective current.

the average of a two-particle correlation function such as that in Eqn. 3.1 is non-trivial. The zeroth order approximation for such an average is the one which assumes the fluctuations between all four random functions to be uncorrelated, and expresses the average of the product as the product of the averages (as in the so called Virtual Crystal Approximation (VCA)). The inherent correlation, however, requires the contributions from averages taken in pairs, triplets and all four random functions. Such disorder induced corrections can be calculated very efficiently within a Feynman diagrammatic technique (details have been discussed in Ref. [50]), which renormalizes both the phonon propagators as well as the heat currents to provide a mathematical expression for $\langle\langle\kappa\rangle\rangle$ with an *effective* heat current $\mathbf{S}_{\rm eff}$ related to the self-energy of the propagators (shown by 1st diagram on RHS of the middle row of Fig. 3.1). The last term in the middle row gives the contribution from the so called vertex correction

arising out of the correlated propagation. For a harmonic solid, thermal diffusivity has a similar expression as $\langle\langle\kappa\rangle\rangle$ except the product of five random functions instead of four. A similar diagrammatic procedure has been used earlier by Alam *et.al.*[50] to calculate the configuration averaged thermal diffusivity as given by

$$\begin{aligned}\langle\langle D(\nu)\rangle\rangle &= \frac{1}{\pi^2}\int d\nu' \int \frac{d^3\mathbf{k}}{8\pi^3} \\ &\mathrm{Tr}\left[\langle\langle \Im m\mathbf{G}(\mathbf{k},\nu')\mathbf{S}(\mathbf{k})\Im m\mathbf{G}(\mathbf{k},\nu')\mathbf{S}(\mathbf{k})\Im m\mathbf{G}(\mathbf{k},\nu)\rangle\rangle\right].\end{aligned}$$

In this chapter, we used the first-principles Quantum ESSPRESSO(QE) [35] to extract the force-constants. QE is a linear response based method : the density functional perturbation theory (DFPT) [36]. The dynamical matrix for the phonon excitation of a system is obtained from the ground state electron charge density and its linear response to a distortion of the ion-core geometry. This alloy, being a basic ingredient of stainless steel, is a technologically important structural material, dominated by force-constant disorder and hence should serve as a critical test of our theory for the thermal transport properties.

3.3 Result and dicussion for $\mathbf{Fe_{1-x}Cr_x}$ alloys ($x = 0.25, 0.47,$ and 0.75)

In Fig. 3.2, we display the frequency dependence of lattice thermal conductivity $\kappa(\nu)$ and the scaled joint density of states $J(\nu)$ at $T = 200$ K for the $Fe_{53}Cr_{47}$ alloy. It is obvious from the figure that the transition rate τ (related to the heat current operator) is strongly dependent both on the initial and final energies throughout the phonon spectrum i.e. $\kappa(\nu,T) \neq |\tau(\nu,T)|J(\nu)$, where $J(\nu)$ (shown by dot-dashed line in Fig. 3.2) is given by

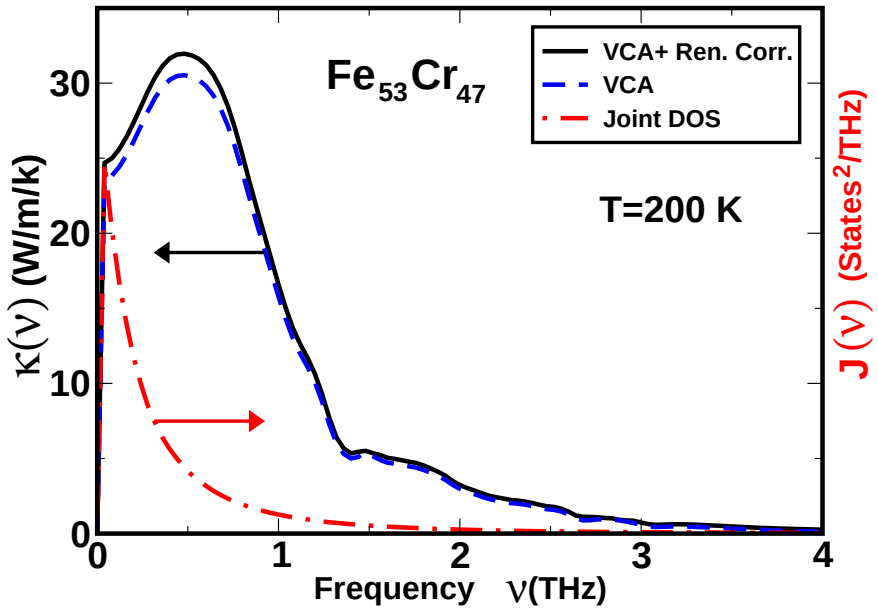

Figure 3.2: (Color Online) Frequency dependence of Thermal conductivity and Joint density of states for $Fe_{53}Cr_{47}$ alloy at $T = 200$ K. Solid line shows the result including all disorder-induced corrections + the vertex correction (middle row of Fig. 3.1) and dashed line including the VCA average alone.

$$\langle\langle J(\nu)\rangle\rangle \;=\; \int d\nu' \int \frac{d^3\mathbf{k}}{8\pi^3} \mathrm{Tr}\left[\Im m\langle\langle \mathbf{G}(\mathbf{k},\nu')\rangle\rangle \Im m\langle\langle \mathbf{G}(\mathbf{k},\nu'+\nu)\rangle\rangle\right].$$

The effect of disorder-induced renormalized corrections (black solid lines) to the zeroth order virtual-crystal-approximation (VCA) (blue dashed line) thermal conductivity is not significant, and becomes negligibly small beyond $\nu = 2.7$ THz. The traditional single site mean-field approximation is, therefore, expected to describe well the multiple scattering phenomenon associated with the high frequency mode, deviating only in the low frequency range where the higher order corrections become important. Notably, both $\kappa(\nu)$ and $J(\nu)$ curve has a dip at a very small energy

($\nu \simeq 0$). Such a dip reflects the missing intraband contribution (κ^{II}) to the conductivity. The origin of this dip is a natural outcome of a smooth convolution of two Green matrices $\mathbf{G}(\mathbf{k}, \nu')$ and $\mathbf{G}(\mathbf{k}, \nu' + \nu)$ (or two smooth DOS). A similar dip has also been reported by Feldman *et.al.*[48] in amorphous Si and $Si_{1-x}Ge_x$ alloys. Unlike our case ($\kappa(\nu) \to 0$ as $\nu \to 0$), this dip in their calculation stands at a finite value as $\nu \to 0$. These authors have introduced an arbitrary Lorenzian broadening of the delta functions in their Kubo-Greenwood expression for κ, while in our calculation this arises naturally through the disorder induced broadening of the spectral function $\Im m[\mathbf{G}(\mathbf{k}, \nu)]$. An extrapolation of our $\kappa(\nu)$-curve (see Fig. 3.2) from a value just above $\nu = 0$ to a value at $\nu = 0$ yields an estimate of the dc thermal conductivity, which comes out to be 24.7 W/m/K for the present $Fe_{53}Cr_{47}$ alloy at $T = 200$ K. Literature survey shows a lack of available experimental data for concentrated $Fe_{1-x}Cr_x$ alloy, however there exist some on the dilute Cr alloys[90]. For example κ_{expt} for x=0.25% Cr is $\sim 22W/(mK)$, with which we shall compare our theoretical estimate below.

Figure 3.3 shows the temperature dependence of thermal conductivity for three $Fe_{1-x}Cr_x$ alloys. Note that $\kappa(T)$ behaves quadratically (see inset) in the low temperature regime ($T < 20$ K) where only low-energy vibrations are excited. As the temperature is increased further, the T-dependence of κ becomes much milder and eventually reaches a T-independent saturated value. The origin of such a high T-saturation is not very well described by most previous theories. Within a harmonic approximation, such a saturation mainly arise from the T-dependence of Einstein specific heat piece of the conductivity expression [48]. The intrinsic harmonic diffusion of higher energy delocalized vibrations are mostly responsible for the relevant dominant mechanism in this regime. Another qualitative explanation can be that

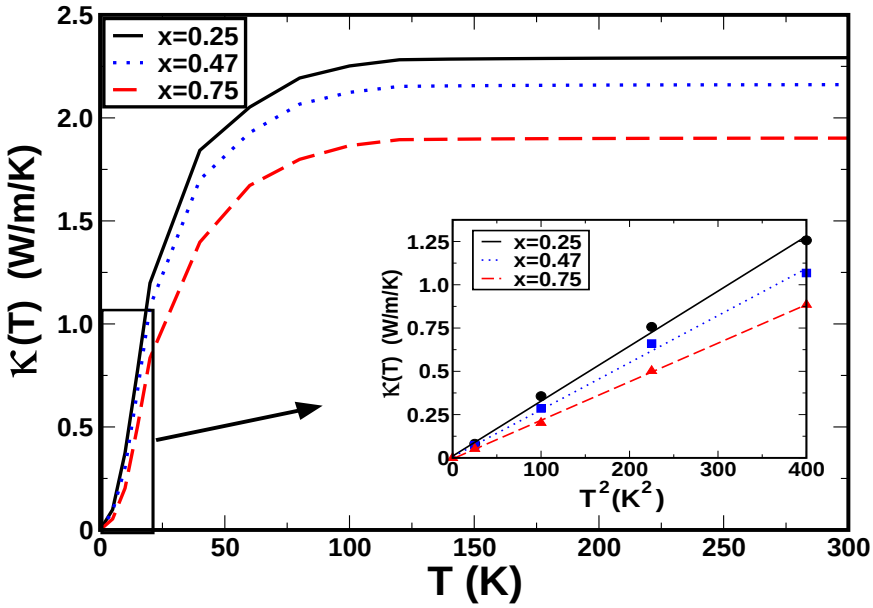

Figure 3.3: (Color Online) Temperature dependence of Thermal conductivity (κ) for three $Fe_{1-x}Cr_x$ alloys. Inset shows the quadratic T-dependence of κ in the low T-range.

: the phonon-phonon scattering in this high T-range becomes so strong that the phonon MFPs reach a minima, and further enhancing the disorder scattering by raising temperature would not cause any further reduction in the MFP, hence resulting in a T-independent thermal conductivity. This, however, is just a physically plausible explanation based on the MFP and is not intended to reflect a known basis in the proposed theory itself. One can also notice an overall reduction of κ with increasing disorder (x), as expected. Such effect usually reflect the scattering arising out of the difference in masses, radii and force constants between the host lattice atoms and impurities. In the present $Fe_{1-x}Cr_x$ alloy, however, this scattering is mainly dominated by a large difference of force constants between Fe and Cr atoms in the alloy, while their masses and radii are almost similar.

Next, we examine the effect of disorder scattering on the vibrational eigenstates

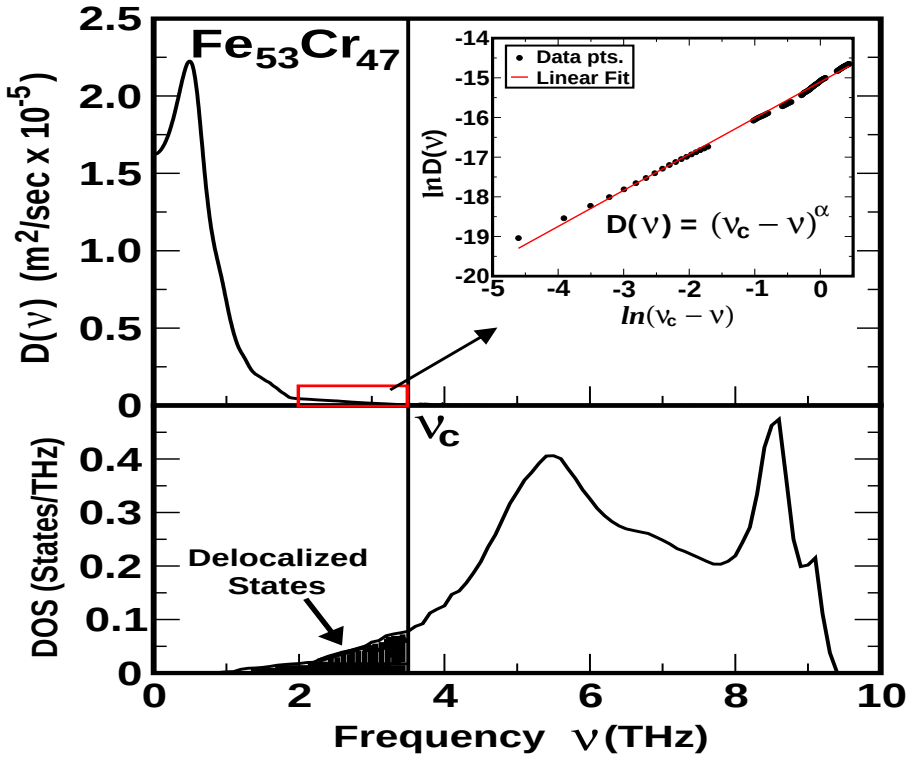

Figure 3.4: (Color Online) Thermal diffusivity (top) and DOS (bottom) vs. phonon frequency (ν) for $Fe_{53}Cr_{47}$ alloy. Inset shows an approximate linear ν-dependence of $D(\nu)$ above 2 THz. ν_c locates the mobility edge and area under the shaded region gives an estimate of the fraction of delocalized states.

and hence the localization of the phonon modes based on a thermal diffusivity calculation. In Fig. 3.4, we show the thermal diffusivity (top panel) and the phonon density of states (bottom panel) vs frequency for the $Fe_{53}Cr_{47}$ alloy. Above $\nu \simeq$ 2 THz, D(ν) decreases smoothly (approximately linear in ν) with a critical frequency $\nu_c = 3.55$ THz, where D(ν) vanishes to within a very small level of noise. This regime is shown, for clarity, as a log-log plot within the inset of the upper panel. The calculated critical exponent $\alpha \simeq 1.011$ agrees with the scaling and other theories of Anderson localization [51]. The critical frequency ν_c locates the mobility edge above which the diffusivity strictly goes to zero in the infinite size limit, and the allowed

vibrational states below this frequency remain delocalized. This is shown by the area under the shaded region in the lower panel which gives an estimate of the percentage of delocalized states.

An alternative way of estimating the fraction of localized (delocalized) states is to calculate the so called "*inverse participation ratio*" $1/p_\gamma$ defined as, $1/p_\gamma = \sum_\mu \int (d^3k/8\pi^3)\ \epsilon_\gamma^\mu(\mathbf{k})$, where $\epsilon_\gamma^\mu(\mathbf{k})$ is the μth Cartesian component of the normalized polarization vector of the γth mode. p_γ measures the number of atoms on which γth vibrational mode has significant amplitude. $1/p_\gamma \to 0$ for delocalized mode, but remains finite for localized modes. Although this procedure provides a quick assessment of localization, it suffers from a shortcoming which arises quite often from the existence of an unexpected *few* localized modes in the low frequency regime (e.g. within the shaded region in the lower panel of Fig. 3.4), as discussed earlier[48, 52]. This is mainly due to a sensitive dependence of p_γ on the boundary condition used in the concerned model. In other words, finite-size theory (even for large model systems) causes an unphysical gap at the bottom of the spectrum, and the states in a macroscopic sample, however, may not be localized but propagating (or may be resonant)[48]. The percentage of localized (delocalized) states calculated using the area above (below) μ_c of DOS curve and using p_γ may differ, if calculated from such finite-size theories. However, being a k-space based formulation, our theory does not suffer from such differences and is free from the unexpected errors arising from the existence of few localized modes in the low-energy regime.

The location of the mobility edge (ν_c) and the percentage of localized states with varying Cr-content in $Fe_{1-x}Cr_x$ alloy is shown in Fig. 3.5. Such a non-monotonous variation of the fraction of localized states is an artifact of the varying band-width of the phonon spectrum with x. Unlike the mass dominated $Si_{1-x}Ge_x$ alloys [48]

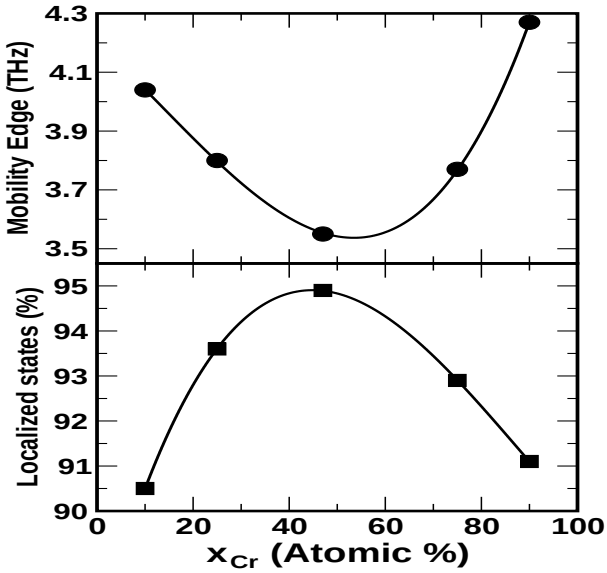

Figure 3.5: Mobility edge (top) and the percentage of localized states (bottom) vs Cr-concentration for $Fe_{1-x}Cr_x$ alloy.

which show an increasing percentage of localized states, towards the upper end of the phonon spectrum, with increasing Ge-concentration, the Fe-Cr alloys show maximum localization at $x_{\mathrm{Cr}} = 47$ %. We believe that, this arises due to the dominance of the force constant disorder in the present alloy which causes an enhanced disorder scattering at $x = 47$ % and hence localize the vibrational modes maximally.

3.4 Concluding Remarks

In summary, we combine a generalized Kubo-Greenwood type formula with the linear-response based Quantum Espresso calculation to make a first principles prediction of the thermal conductivity and diffusivity of disordered Fe-Cr alloys. The effect of disorder-induced scattering on thermal conductivity(κ) is found to decrease with increasing phonon energy. Thermal conductivity shows a quadratic T-dependence in

the low T-regime, increasing smoothly to a T-independent saturated value at high T. Thermal diffusivity provides an estimate of the location of mobility edge, which subsequently gives an idea about the disorder-induced localization in the system. Vibrational modes in the present $Fe_{1-x}Cr_x$ alloy are maximally localized at $x = 47$ %, where the effect of disorder scattering is maximum.

Chapter 4

Phonon study based on Augmented space recursion and Special quasi-random structure

4.1 Introduction

Interatomic force constants in disordered alloys is one of the key factors to the study of phonon. A reliable prediction based on first principles method is still missing. The main reason is due to the presence of off-diagonal (multisite) disorder arising out of the dynamical matrices $D_{\mu\nu}(R_i - R_j)$ in the phonon problem. In additions the sum rule $D_{\mu\nu}(R_i) = -\sum_{R_j} D_{\mu\nu}(R_i - R_j)$ which needs to be satisfied, makes the disorder at a site depend upon its immediate neighborhood. As we already discussed in chapter 1, coherent potential approximation (CPA) and other mean-field approaches are inapplicable to this problem. A striking approach, that has emerged in recent years, is the so called special quasirandom structure (SQS) proposed by Zunger *et al.* [9], which carries the signature of configuration correlation with them. In particular, SQS is an ordered supercell which is constructed in such a way to mimic the most relevant pair and multisite correlation functions of the disordered phase. Unlike CPA and other related approaches, SQS is a local structural model which captures the most

relevant microstates of disordered phase.

As far as the calculation of force constants for random alloys are concerned, three approaches have been mainly utilized in the past. The first attempt [54, 13] was to fit an empirical set of force constants to match the available experimental phonon spectra. The second approach was to compute the force constants from selected ordered structures and then use them for random alloys [46]. This is of course not a proper solution, because dynamical matrices are not directly transferable across the environment [55]. In later studies [56], few SQS methods have been used, but only $\leq$ 8-atoms cell were used which is not enough to capture the detailed properties of phonons.

In addition to configuration averaging the estimation of reliable force constants plays an important role in getting the phonon spectra, DOS etc for disorder alloys. Augmented space recursion is a powerful technique to deal with configuration disorder which is being explained in Chapter 1 of this thesis. Here we have merged a first principles SQS method with the ASR to demonstrate the interplay of force constant within a disordered environment. Unlike previous approaches, a systematic calculation of the force constants with increasing size of the SQS cell is made. Stress on the atomic sites are directly related to the force constant matrix and hence a small disturbance leads to a large change. To overcome this effect we use the SQS cell in conjunction with the *small displacement method* [60], to construct the dynamical matrix $D_{\mu\nu}$. Based on the predicted bond length distribution and the calculated force constants for each pairs A-A, B-B, and A-B, it is concluded that a minimum of 32-atom SQS cell is needed to capture the important disorder correlation, and hence a reliable phonon dispersion. Two different alloy systems, bcc TaW and fcc NiPt, are chosen to demonstrate the reliability of the approach. Inelastic neutron scattering

data is available for both the system, to compare our theoretical results. In NiPt (fcc) alloy Ni and Pt has large size and mass mismatch (size $\sim$ 12%, mass of Pt is 3-times heavier than Ni) as well as force constant ($\phi_{\text{Pt-Pt}}$ is 55% larger than $\phi_{\text{Ni-Ni}}$). On the other hand for TaW (bcc) alloy Ta and W belong to 5-d metal series with similar size and atomic masses, but quite different force constants. We compare our theoretical force constant matrix to the experimental data available.

4.2 Treatment to force constants (FC)

4.2.1 Non-symmetric FC computation

To keep the real picture of disorder in force constants we first develop a structural model based on the SQS method [9], which is an N-atom periodic structure constructed in such a way that the associated set of correlation function of this structure mimic the ensemble average correlation functions of the random alloy. For both cases, fcc and bcc system we used three different sized SQS-cells (8-atom, 16-atom, and 32-atom).

We use Vienna ab-initio simulation package (VASP) [58] with a pseudo-potential and a projected-augmented-wave (PAW) basis[59] based on the local density approximation (LDA). The cut-off energy for the electronic wavefunctions is 500 eV. All the structures are fully relaxed until the energy converges to within 10^{-6} eV and the forces on each atom is less than 0.001 $e\text{V}/\mathring{A}$. A Monkhorst-pack Brillouin zone integration with a 8^3 **k**-mesh is used for $>$ 16-atom SQS calculation. Smaller **k**-meshes are used for 8-atom 2x2x1 supercell. Magnetic (non-magnetic) calculations are done for NiPt (Ta-W) systems. Relaxed lattice constants for 8-atom, 16-atom, and 32-atom SQS calculation for fcc $Ni_{50}Pt_{50}$ are 3.72$\mathring{A}$, 3.72 $\mathring{A}$, and 3.70 $\mathring{A}$ respectively, compared to

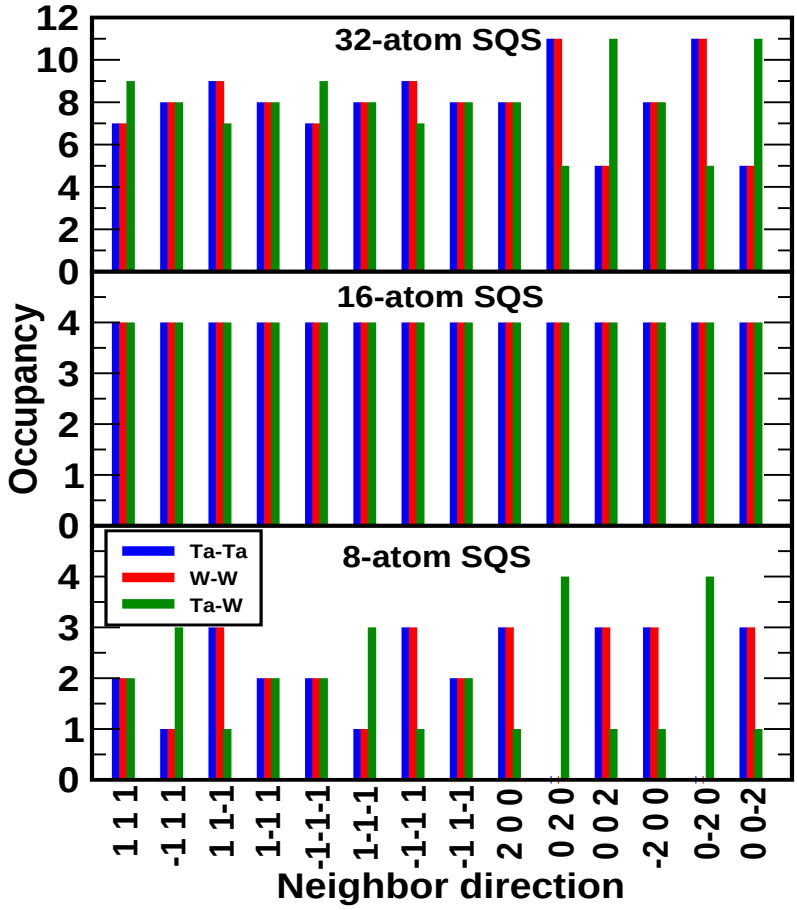

Figure 4.1: (Color online) Number of occupation for Ta-Ta, W-W and Ta-W pairs along various neighbor directions with 32 (top), 16 (middle) and 8 (bottom) atom SQS for bcc $Ta_{50}W_{50}$.

the experimental value of 3.785 $\mathring{A}$ [61], For bcc $Ta_{50}W_{50}$, they are 3.23 $\mathring{A}$ for all the structures, compared to 3.23 $\mathring{A}$ as observed [62]. To extract the force constant matrices, we use the fully relaxed SQS structures and apply the *small displacement method* using PHON package [60] implemented within VASP. Force fields are constructed by applying 48 displacements for $Ni_{50}Pt_{50}$ and 96 displacements for $Ta_{50}W_{50}$ along 3-cartesian axes, each of amplitude 0.04 $\mathring{A}$.

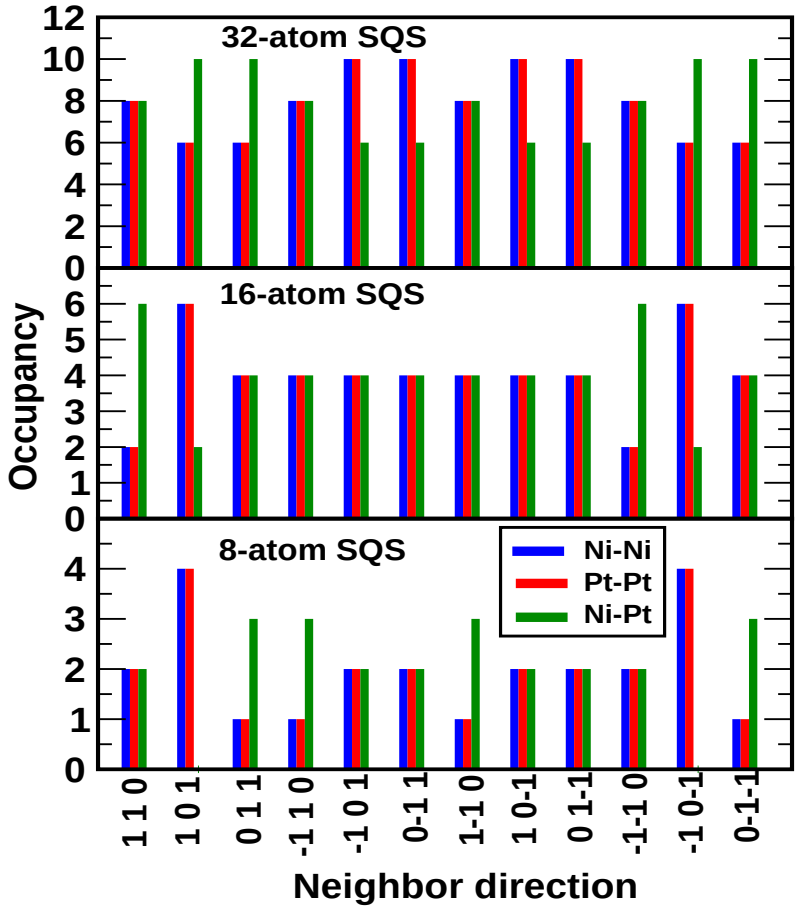

Figure 4.2: (Color online) Number of occupation for Ni-Ni, Pt-Pt and Ni-Pt pairs along various neighbor directions with 32 (top), 16 (middle) and 8 (bottom) atom SQS for fcc $Ni_{50}Pt_{50}$.

4.2.2 Symmetrization of FC matrices

Special quasi-random structures are having low symmetry in the underlying lattice (fcc and bcc in present case) which result to the non-symmetric force constant. As we have relaxed the structure the proper symmetry for FCC (along $[\frac{1}{2}\frac{1}{2}0]$) and BCC (along $[\frac{1}{2}\frac{1}{2}\frac{1}{2}]$&[100])

From		To	Transformation matrix
$[1\ 0\ 1]$	$\rightarrow$	$[1\ 1\ 0]$	$F_1 = \begin{pmatrix} 1 & 0 & 0 \\ 0 & 0 & 1 \\ 0 & -1 & 0 \end{pmatrix}$
$[0\ 1\ 1]$	$\rightarrow$	$[1\ 1\ 0]$	$F_2 = \begin{pmatrix} 0 & 0 & 1 \\ 0 & 1 & 0 \\ -1 & 0 & 0 \end{pmatrix}$
$[\bar{1}\ 1\ 0]$	$\rightarrow$	$[1\ 1\ 0]$	$F_3 = \begin{pmatrix} -1 & 0 & 0 \\ 0 & 1 & 0 \\ 0 & 0 & -1 \end{pmatrix}$
$[\bar{1}\ 0\ 1]$	$\rightarrow$	$[1\ 1\ 0]$	$F_4 = \begin{pmatrix} 1 & 0 & 0 \\ 0 & 0 & -1 \\ 0 & 1 & 0 \end{pmatrix}$
$[0\ \bar{1}\ 1]$	$\rightarrow$	$[1\ 1\ 0]$	$F_5 = \begin{pmatrix} 0 & 0 & -1 \\ 0 & 1 & 0 \\ 1 & 0 & 0 \end{pmatrix}$

Table 4.1: Transformation matrices for FCC upto 1st nearest neighbour

$$\Phi_{fcc} = -\begin{pmatrix} \alpha & \beta & 0 \\ \beta & \alpha & 0 \\ 0 & 0 & \gamma \end{pmatrix}, \Phi_{bcc} = -\begin{pmatrix} \alpha_1 & \beta_1 & \beta_1 \\ \beta_1 & \alpha_1 & \beta_1 \\ \beta_1 & \beta_1 & \alpha_1 \end{pmatrix} \& -\begin{pmatrix} \alpha_2 & 0 & 0 \\ 0 & \beta_2 & 0 \\ 0 & 0 & \beta_2 \end{pmatrix}$$

is not maintained and get the general form as nearest neighbor is

$$\Phi_{ij} = \begin{pmatrix} a_{11} & a_{12} & a_{13} \\ a_{21} & a_{22} & a_{23} \\ a_{31} & a_{32} & a_{33} \end{pmatrix}$$

modified as $(\frac{1}{2} \pm \delta_1^1, \frac{1}{2} \pm \delta_2^1, \pm\delta_3^1)$, $(\frac{1}{2} \pm \delta_1^2, \frac{1}{2} \pm \delta_2^2, \frac{1}{2} \pm \delta_3^2)$, and $(1 \pm \delta_1^3, \pm\delta_2^3, \pm\delta_3^3)$ respectively. To overcome this Lattice imposed symmetric dynamical matrices are required to perform a direct configuration average within the ASR scheme. These symmetric matrices are also directly comparable to the neutron scattering data and

other theoretical results, if available. In order to resort to the symmetry of the underlying lattice, we followed two steps: (1) For a particular SQS-cell of a given lattice, one can see various atom-pairs along specific crystal directions (See Fig. 4.1 and 4.2 for occupancy number for each pair A-A, B-B, and A-B along various neighbor directions). Depending on the occupancy number, the force constants are averaged for each configurations (i.e. A-A, B-B, and A-B pair) along every directions (upto first nearest neighbor [nn] for fcc and second neighbor [nnn] for bcc lattices). (2) Having done the directional averaging, we still lack the proper symmetry of the dynamical matrices for the underlying lattice. This is due to the relaxation effect, which modifies the atomic positions by δ. For example, a particular atom at (1/2,1/2,0) in a perfect fcc lattice moves to $(1/2 \pm \delta_1^1, 1/2 \pm \delta_2^1, \pm\delta_3^1)$ or atoms at (1/2,1/2,1/2) and (1,0,0) in a bcc lattice moves to $(1/2 \pm \delta_1^2, 1/2 \pm \delta_2^2, 1/2 \pm \delta_3^2)$ and $(1 \pm \delta_1^3, \pm\delta_2^3, \pm\delta_3^3)$ respectively. In order to retrieve the desired symmetry of the dynamical matrix, we apply transformation operation on these average matrices to get the direction specific dynamical matrices e.g. $\phi_{111} = B_1 \phi_{-111} B_1^T$ along one of the nearest neighbor direction of bcc lattice, where B_1 is the transformation matrix. The Transformation matrices along specific direction (i.e. [110] for fcc and [111], [200] for bcc) are given in table 4.1 and 4.2 respectively.

4.3 $Ta_{50}W_{50}$ and $Ni_{50}Pt_{50}$ alloys

In earlier section we have mentioned about the occupancy of A-kind and B-kind of atoms in A-B alloy along different directions (Fig. 4.1 and 4.2). Figure 4.1 shows the number of occupation for three different pairs Ta-Ta, W-W, and Ta-W along various neighbor directions (1st and 2nd neighbors) for 32-atom (top), 16-atom (middle), and 8-atom (bottom) SQS cell for bcc $Ta_{50}W_{50}$.

From		To	Transformation matrix
$[\bar{1}\ 1\ 1]$	$\rightarrow$	$[1\ 1\ 1]$	$B_1 = \begin{pmatrix} -1 & 0 & 0 \\ 0 & 1 & 0 \\ 0 & 0 & 1 \end{pmatrix}$
$[1\ \bar{1}\ 1]$	$\rightarrow$	$[1\ 1\ 1]$	$B_2 = \begin{pmatrix} 1 & 0 & 0 \\ 0 & -1 & 0 \\ 0 & 0 & 1 \end{pmatrix}$
$[1\ 1\ \bar{1}]$	$\rightarrow$	$[1\ 1\ 1]$	$B_3 = \begin{pmatrix} 1 & 0 & 0 \\ 0 & 1 & 0 \\ 0 & 0 & -1 \end{pmatrix}$
$[0\ 2\ 0]$	$\rightarrow$	$[2\ 0\ 0]$	$B_4 = \begin{pmatrix} 0 & 1 & 0 \\ -1 & 0 & 0 \\ 0 & 0 & 1 \end{pmatrix}$
$[0\ 0\ 2]$	$\rightarrow$	$[2\ 0\ 0]$	$B_5 = \begin{pmatrix} 0 & 0 & 1 \\ 0 & 1 & 0 \\ -1 & 0 & 0 \end{pmatrix}$

Table 4.2: Transformation matrices for BCC upto 2nd nearest neighbour

As expected, 32-atom SQS-cell shows the largest number of each pairs, and provide a proper averaging for both bond distances and the force constant matrices for each pairs. We have tried larger SQS cells as well, but the calculated force constants did not change much compared to those from 32-atom SQS results. The calculated dispersion in the occupancy for each pairs reflect the sensitivity of the bond distances on the local environment. This eventually affects the calculated force constants. The calculated nearest neighbor (next nearest neighbor) average bond distances for three pairs $d_{Ta\text{-}Ta}$, $d_{W\text{-}W}$, and $d_{Ta\text{-}W}$ are 2.837 $\mathring{A}$ (3.220 $\mathring{A}$), 2.775 $\mathring{A}$ (3.226 $\mathring{A}$), and 2.788 $\mathring{A}$ (3.235 $\mathring{A}$) respectively for 32-atom SQS $Ta_{50}W_{50}$. The nn-bond distance for Ta-Ta in the alloy is found to be $\sim$ 0.8% smaller compared to that in pure Ta, while W-W bond distance in the alloy is $\sim$ 1.7% larger than that in pure W. Such a sensitivity of the bond distance on the disordered environment in turn affect the alloy force constants. The calculated dynamical matrices (upto 2nd neighbor) for 8-atom, 16-atom, and 32-atom

bcc $Ta_{50}W50$						
	8-atom^a	8-atom^b	16-atom	32-atom	Expt.[66]	direction
Ta-Ta	27.707	23.573	25.103	22.324	16.983	111_{xx}
W-W	28.934	19.581	24.568	21.063	23.000	111_{xx}
Ta-W	27.734	22.186	26.071	23.192	23.984	111_{xx}
Ta-Ta	11.504	16.404	15.727	16.120	11.201	111_{xy}
W-W	6.655	10.584	8.348	9.418	19.200	111_{xy}
Ta-W	8.585	12.240	13.080	13.668	17.603	111_{xy}
Ta-Ta	-0.009	15.202	9.114	25.937	1.182	200_{xx}
W-W	0.016	20.136	17.693	36.233	47.300	200_{xx}
Ta-W	16.448	29.435	13.442	30.733	24.803	200_{xx}
Ta-Ta	-0.001	-0.751	3.105	-2.909	1.423	200_{yy}
W-W	0.008	-0.114	2.755	-1.648	-0.800	200_{yy}
Ta-W	-1.634	-0.667	3.656	-2.163	1.184	200_{yy}

Table 4.3: Dynamical matrices $D_{\mu\nu}(|R|)$ (Newton/meter) for bcc $Ta_{50}W_{50}$. N-atom represents the size of the SQS supercell. 8-atom SQS calculations are done with two supercell size: $1 \times 1 \times 1$ (8-atom^a) and $2 \times 2 \times 1$ (8-atom^b). Other experimental[66] data are give for comparison.

SQS $Ta_{50}W_{50}$ are shown in the Table 4.3. In order to compare the sensitivity of long ranged environment, 8-atom SQS calculation is done with two cell size (i) conventional 8-atom SQS indicated by 8-atom^a and (ii) a $2 \times 2 \times 1$ supercell of the conventional 8-atom SQS-cell indicated by 8-atom^b. Notice that the conventional 8-atom^a SQS-cell can not capture the second neighbor information properly as reflected by the vanishingly small force constants for Ta-Ta and W-W pairs. Note that, experimental force constants for Ta-Ta and W-W pairs are not for the alloy, but for pure Ta [64] and pure W [65] respectively. Force constants for Ta-W [66] pair, however, are indeed for the alloy. Notably our calculated Ta-Ta force constants in the alloy are stiffer compared to those in pure Ta. On the other hand, the calculated W-W force constants are softer than those in pure W. This prediction actually be with the calculated bond lengths between these two pairs. Alloying shrinks (expands) the Ta-Ta (W-W) bond lengths making the springs relatively stiffer (softer). As far as the force constants

fcc $Ni_{50}Pt_{50}$						
	8-atom^a	8-atom^b	16-atom	32-atom	Other[67]	direction
Ni-Ni	6.289	8.901	8.433	9.813	8.231	110_{xx}
Pt-Pt	13.755	26.575	34.576	36.317	33.494	110_{xx}
Ni-Pt	12.421	17.098	17.387	21.210	17.868	110_{xx}
Ni-Ni	3.791	9.432	8.845	11.115	9.580	110_{xy}
Pt-Pt	9.008	30.877	36.546	43.377	39.655	110_{xy}
Ni-Pt	8.026	19.511	18.287	25.091	20.740	110_{xy}
Ni-Ni	5.394	-0.107	0.946	-1.845	-0.525	110_{zz}
Pt-Pt	9.487	-4.739	2.310	-8.351	-6.854	110_{zz}
Ni-Pt	8.785	-1.443	1.035	-4.124	-2.820	110_{zz}

Table 4.4: Dynamical matrices $D_{\mu\nu}(|R|)$ (Newton/meter) for fcc $Ni_{50}Pt_{50}$. N-atom represents the size of the SQS supercell. 8-atom SQS calculations are done with two supercell size: $1 \times 1 \times 1$ (8-atom^a) and $2 \times 2 \times 1$ (8-atom^b). Other theoretical[67] data are give for comparison.

for Ta-W pair goes, 32-atom SQS results are our best numbers to compare with the experiment [66]. Experimental force constants are computed using using a polynomial fit to their measured dispersion (extended upto 7th nearest neighbors). Keeping in mind the sensitivity of the estimates both on the theoretical and experimental front, the overall agreement between the 32-atom SQS results and the experiment for Ta-W force constants is fairly well.

Figure 4.2 shows the variation of occupation for three pairs along the nearest neighbor directions for 32-atom (top), 16-atom (middle) and 8-atom (bottom) SQS fcc $Ni_{50}Pt_{50}$ alloy. This system is interesting because of the large difference in size, mass and force constants of the constituent atoms. One can notice from the histogram that there exists a large scatter in the number of occupation between each pair. The calculated average bond lengths for Ni-Ni, Pt-Pt and Ni-Pt pairs are 2.573 $\mathring{A}$, 2.692 $\mathring{A}$ and 2.604 $\mathring{A}$ for 32-atom SQS cell. Ni-Ni (Pt-Pt) bond length in the alloy is $\sim$ 3.3% larger ($\sim$ 2.8% smaller) than those in pure Ni (Pt). As such, Ni-Ni (Pt-Pt) force constants in the random alloy is expected to get softer (stiffer) compared to those in

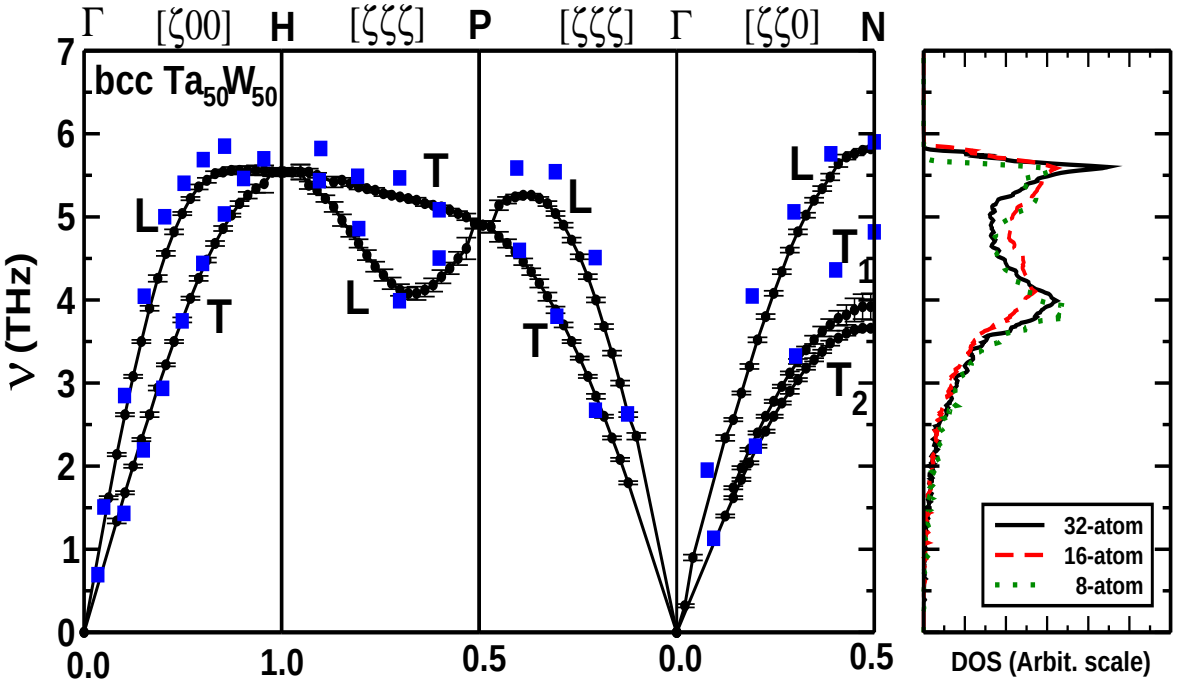

Figure 4.3: (Color online) (Left) Phonon dispersion for bcc $Ta_{50}W_{50}$ alloy using the force constants of 32-atom SQS. L and T stands for longitudinal and transverse modes. Error bars indicate the calculated FWHM's. Square symbols indicate experimental data [66]. (Right) Phonon DOS using the force constants of 32-, 16-, and 8-atom SQS.

pure Ni (Pt). The calculated ab-initio force constants for the three pairs in disordered $Ni_{50}Pt_{50}$ alloy are shown in the Table 4.4. As before, results are shown for 8-atom, 16-atom and 32-atom SQS. The force constants under the column labeled *Other* [67] are the results from a recent calculation for $Ni_{50}Pt_{50}$ alloy by Granas *et al.* [67] These force constants for each pair (Ni-Ni, Pt-Pt and Ni-Pt) are within the disordered environment, and agree fairly well with ours within a few percent. Calculated force constants for Ni-Ni (Pt-Pt) pairs in the alloy are found to be softer (stiffer) compared to those in pure Ni (Pt) (See Ref. [68] for the force constants of pure Ni and Pt). This, again, goes in accordance with the bond lengths of respective pairs in the alloy vs. those in pure elements.

Figure 4.3 shows the calculated phonon dispersion (left) and the configuration averaged phonon DOS (right) for bcc $Ta_{50}W_{50}$. Dispersion curves are calculated using the force constants of 32-atom SQS, as listed in Table 4.3. Phonon DOS, however, are shown with all the three sets of force constants, i.e. 8-, 16- and 32-atom SQS, for comparison. Error bars in the dispersion curve indicate the full widths at half maxima (FWHM). Our calculated phonon dispersion compares fairly well with the experiment [66] (shown by square symbol).

Left panel of Fig. 4.4 shows the phonon dispersion for $Ni_{50}Pt_{50}$ alloy calculated using the force constants of 32-atom SQS cell (see Table 4.3). Unlike TaW, NiPt alloy shows interesting split band behavior along each symmetry direction. This is due to the strong disorder in both mass and force constants, which gives rise to resonant modes, and has been evidenced in previous studies[49, 67] as well. Error bars with solid circles indicate the calculated FWHM. Error bars with square symbol along [ζ00] direction indicate the neutron scattering data. [49] The panel on the right shows the configuration averaged phonon DOS with three sets of calculated force constants. Square symbols indicate the generalized phonon DOS derived from inelastic incoherent scattering. [49] Notice that the calculated band edge increases with increasing the SQS cell size, and compare better with experiment. The integral value under each phonon DOS, however, remain the same. It is important to emphasize that the experimental phonon DOS is only shown for reference. A one to one comparison between our calculated DOS and the experimental DOS is not feasible. In inelastic neutron scattering, phonon DOS can be represented as $N(\omega) = \sum_j (b_j/M_j) n_j(\omega)$, where b_j, M_j and $n_j(\omega)$ are the inelastic scattering cross section, atomic mass, and the partial phonon DOS of atom j respectively. Although the calculated DOS from the force constants of 32-atom SQS cell resembles maximally with the experimental

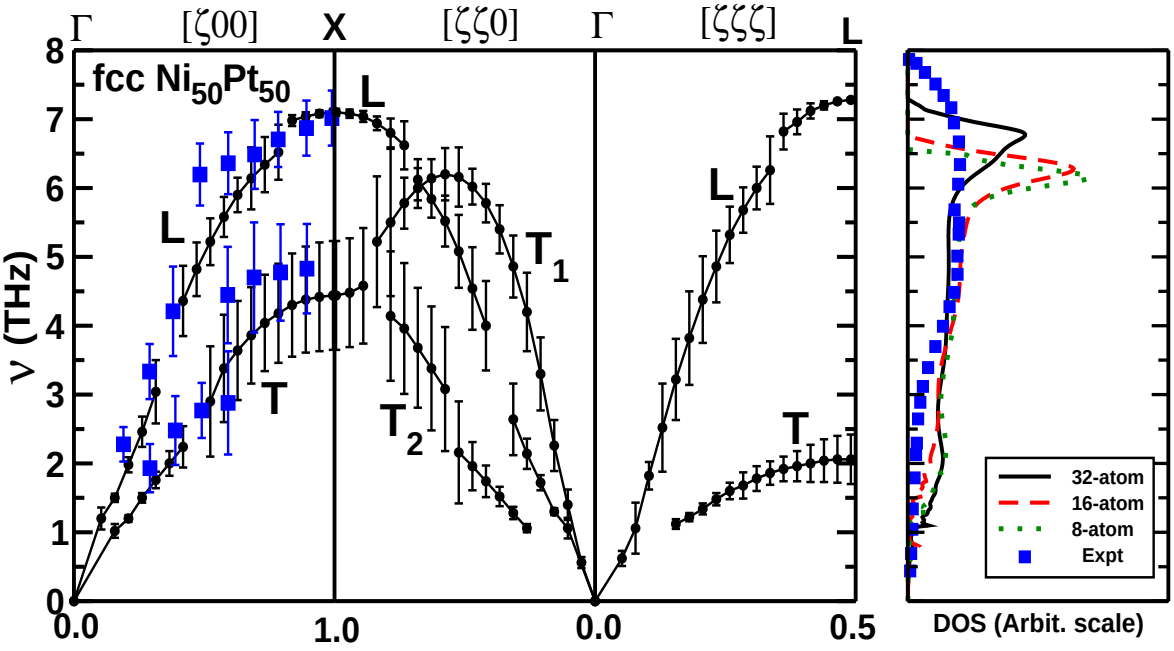

Figure 4.4: (Color online) (Left) Phonon dispersion for fcc $Ni_{50}Pt_{50}$ alloy using the force constants of 32-atom SQS. L and T stands for longitudinal and transverse modes. Error bars indicate the calculated FWHM's. Blue square symbols in both left and right panels indicate the experimental data [49].

4.4 Conclusion

We proposed a systematic first principles calculation of the interatomic force constants for disordered alloys. SQS structures of different cell size are used to capture the effects of random environment at different length scales. Two alloy systems with very different intrinsic properties (e.g. lattice type, masses, force constants etc.) are

investigated. In bcc TaW alloy, Ta-Ta force constants are predicted to be stiffer compared to those in pure Ta, however W-W force constants behave oppositely. In fcc NiPt alloy, Ni-Ni and Pt-Pt force constants within the disordered environment behave softer and stiffer than those in pure Ni and pure Pt. Calculated average bond lengths between each pair of atoms are found to closely dictate the nature of force constants. For both the alloys, the prediction of bond length distribution and the force constants are found to be more accurate with a larger size of the SQS-cell; in particular the 32-atom SQS cell for bcc $Ta_{50}W_{50}$ yields force constants which agree fairly well with experiment.

Chapter 5

Magnetic Phase study for Cu-Mn alloys

5.1 Motivation

In this chapter I will discuss the magnetic phase study for Cu-Mn magnetic alloys. For decades experimental work has been done on Cu-Mn alloy, particularly on its magnetic properties. As early as 1957 Schmitt and Jacobs [69] studied magnetic hysteresis in CuMn with 2 at % Mn. Around the same time neutron scattering measurements by Meneghetti and Sidhu [70] showed that for compositions with $>$ 70 at % Mn the alloys exhibited antiferromagnetism, while for compositions with $<$ 70 at % Mn only a diffuse peak near (100) indicated lack of magnetic long-ranged ordering. A series of later neutron scattering experiments could not resolve the exact nature of the magnetic implications of this diffuse peak [71]-[72]. Later work [71]-[73] indicated the existence of both short-ranged as well as long ranged atomic and magnetic correlations. A detailed experimental work of Gibbs *et.al.*[74] established the magnetic phase diagram of CuMn clearly : with a low-temperature spin-glass phase at low Mn concentrations, a cluster-glass around 50 at % Mn compositions and

[0]The contents of this chapter has been published in, Rajiv Kumar Chouhan, Abhijit Mookerjee, *Journal of Magnetism and Magnetic Materials* **323** 868-873 (2011)

a 'mixed' phase or randomly canted anti-ferromagnetic phase for Mn concentrations > 70 at %. A mixed or randomly canted structures with averaged canting angle of 5^{o} was proposed by Tsunoda and Nakai [75]. Using a parameter fitted random Heisenberg model Chowdhury and Mookerjee [76] showed that a mean-field description of the phase diagram reproduced most aspects of the experimental data of the work of Gibbs *et.al.*[74]. The unsatisfactory part of that work was the fitting of the values for the pair energies and the assumption that these were independent of the alloy composition. The motivation of this work was to satisfy the experimental phase

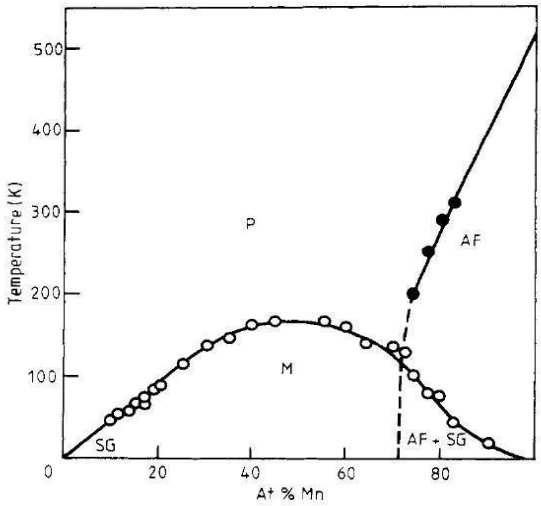

Figure 5.1: The magnetic phase diagram of quenched Cu-Mn alloys showing the composition dependence by Gibbs *et.al.*(1985).

boundaries reported by Gibbs *et.al.*[74] (see Fig. 5.1). For this we carried out generalized perturbation method (GPM) which expands the total band energy in terms of composition fluctuations, obtain the pair energies and locate the temperatures where

the perturbation destabilizes the system. The usual statistical mechanical models used to study magnetism and magnetic phase diagrams of alloys involve the Ising and Heisenberg models, both of which involve localized moments. Straightforward application of such models in our study poses problems as magnetism in such metallic alloys are believed to be itinerant magnetism. Consequently, these localized spin models may be inappropriate. In order to describe our alloys we have to begin with an itinerant picture. This we shall do within a local spin density functional (LSDA) approach. We shall begin with the Kohn-Sham equation for the valence electrons in the alloy. To perform the electronic structure calculation we follow tight-binding, linear muffin-tin orbitals method (TB-LMTO) [77]. Since the system is disordered, our description of self-averaging properties will require configuration averaging, for which we follow augmented space recursion discussed in Chapter 1.

5.2 System study

The TB-LMTO-ASR allows us to obtain the configuration averaged Green function $\ll G^{\sigma}_{\vec{R}_i L \vec{R}_i L}(E) \gg$. From this we obtain the local density of states, the charge and magnetization densities and the local magnetic moment per atom

$$\begin{aligned} n^{\sigma}(E,\vec{R}_i) &= -\frac{1}{\pi}\Im m\ \mathrm{Tr}_L \ll G^{\sigma}_{\vec{R}_i L \vec{R}_i L}(E+i0^+) \gg \\ \rho^{\sigma}(\vec{r}-\vec{R}_i) &= \int_{-\infty}^{E_F} |\Phi(\vec{r}-\vec{R}_i,E)|^2\ n^{\sigma}(E,\vec{R}_i)\ dE \\ \rho(\vec{r}-\vec{R}_i) &= \rho^{\uparrow}(\vec{r}-\vec{R}_i)+\rho^{\downarrow}(\vec{r}-\vec{R}_i) \\ m(\vec{r}-\vec{R}_i) &= \rho^{\uparrow}(\vec{r}-\vec{R}_i)-\rho^{\downarrow}(\vec{r}-\vec{R}_i) \\ m(\vec{R}_i) &= \int_{AS} d^3\vec{r}\, m(\vec{r}-\vec{R}_i) \end{aligned} \tag{5.1}$$

The TB-LMTO-ASR, on which our calculations were based, partitions the solid into atom centric atomic spheres (AS) labeled by $\vec{R}_i$. $\Phi(\vec{r}-\vec{R}_i)$ is the wave function in an AS and $\rho(\vec{r}-\vec{R}_i)$ is the charge density within it. $m(\vec{r}-\vec{R}_i)$ is the magnetic moment density in that AS. From this description it is clear that the magnetic moment is smeared across the AS. $m(\vec{R}_i)$ integrated over an AS is the average magnetic moment associated with it. These magnetic moments are thus built up out of itinerant electron charge densities associated with different spins.

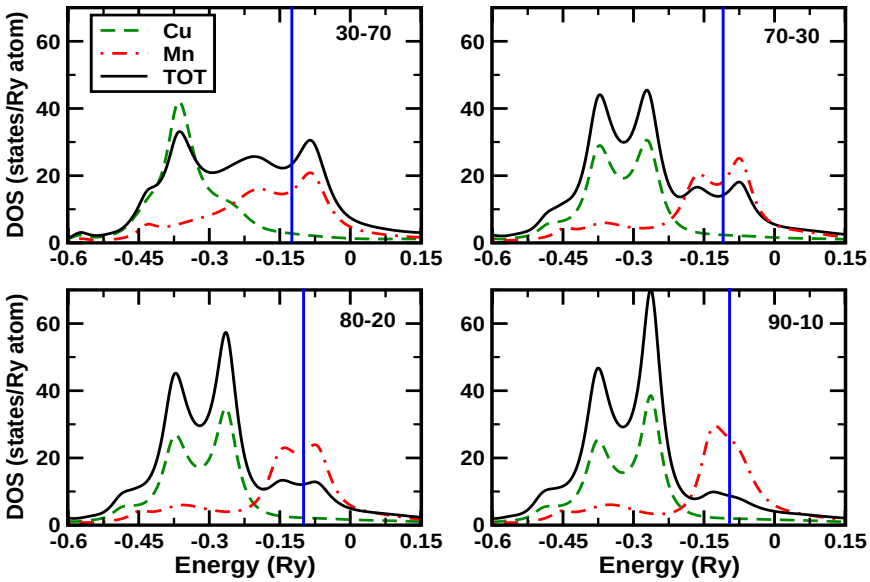

Figure 5.2: Density of states for nonmagnetic CuMn for four compositions (n:m refer to n atomic % of Cu and m atomic % of Mn). The nonmagnetic alloy forms the background of our GPM method.

Fig. 5.2 shows us the TB-LMTO-ASR component projected and total densities of states for several characteristic compositions. The top left panel shows that for the composition $Cu_{30}Mn_{70}$. The Cu and Mn 'bands' are almost non-overlapping and

Cu_xMn_{1-x} is a split band alloy. The minority component Cu has a rather featureless impurity like spectrum imposed upon a broader Mn 'band'. Disorder scattering smoothens out sharp structures in the densities of states. The bottom right panel shows the results for the composition $Cu_{90}Mn_{10}$. Here we see the reverse : with a featureless Mn impurity spectrum and a typical Cu face-centered cubic spectrum at lower energies. At all compositions the signature of a split band is evident.

5.2.1 Generalized Perturbation Method (GPM)

To describe the magnetic phases of an itinerant magnetic alloy we shall follow the generalized perturbation method first introduced by Ducastelle and Gautier [78]. We start from a completely disordered nonmagnetic arrangement of atomic spheres and into that system introduce local configuration fluctuations as perturbations and expand the total band energy :

$$E = E_{\text{dis}} + \sum_{\vec{R}_i \in Mn} E^{(1)}(\vec{R}_i)\ \delta\xi_i^Q + \sum_{\vec{R}_i, \vec{R}_j \in Mn} E^{(2)}(\vec{R}_i, \vec{R}_j)\ \delta\xi_i\ \delta\xi_j \ldots \tag{5.2}$$

We can interpret the second and third term as: if E^A is the configuration averaged total energy of a configuration in which any arbitary site labeled R_i is occupied by an atom of the type A and other sites are randomly occupied, and E^{AB} is the averaged total energy of another configuration in which the sites R_i and R_j are occupied by atoms of the types A and B respectively, and all other sites are randomly occupied, then Eqn. 5.2 can be shown as

$$E^{(1)}(R_i) = E^A - E^B; E^{(2)}(R_i, R_j) = \frac{1}{2}[E^{AA} + E^{BB} - E^{AB} - E^{BA}] \tag{5.3}$$

The single site energy $E^{(1)}(R_i)$ correspond to inhomogeneous disorder and $E^{(2)}(R_i, R_j)$, the pair interaction energy gives the ordering energy.

In the alloy, Cu carries no magnetic moment. Consequently, the summations $\vec{R}_i, \vec{R}_j$ are over those sites occupied by Mn. The scalar variable $\delta\xi_i$ takes the value ± 1 according to whether the atomic sphere labeled by $\vec{R}_i$, occupied by a magnetic Mn, has its average moment. (constructed out of the itinerant electron charge densities) pointing in the quantization direction or opposite to it. Note that $\delta\xi_i$ are *not* spin variables. Once the magnetic moment in the AS labeled by $\vec{R}_i$ is built up from itinerant electron densities, the variables $\delta\xi_i$ describe how the AS and its associated magnetic moment densities are arranged as a pattern on the lattice.

Although GPM is computationally fast but has major drawback in order to calculate $E^{(2)}(R_i, R_j)$; the terms E^{ij} are very large and comparable in magnitude. Hence , the difference between these two quantities is too small, which leads to error in δE^{ij} measurement. This problem is overcome using the orbital peeling method discussed below.

5.2.2 Orbital Peeling

Orbital peeling technique was first proposed by Einstein and Schrieffer [79] and was generalized by N. R. Burke [11] to take very small energy differences into account accurately.

As seen earlier the terms $E^{(1)}(\vec{R}_i)$, $E^{(2)}(\vec{R}_i, \vec{R}_j)$ are called the renormalized single-site and pair energies. The former plays no role in ordering of the AS, while the higher terms like triplet and quadruplet energies are assumed to be small enough to be ignored. It is easy to note from the above definition that :

$$E^{(2)}(\vec{R}_i - \vec{R}_j) = \frac{1}{2} \sum_{\sigma,\sigma'} \chi_{\sigma\sigma'} \; E^{\sigma\sigma'}_{\vec{R}_i,\vec{R}_j} \tag{5.4}$$

where $\chi_{\sigma\sigma'} = 2\delta_{\sigma\sigma'} - 1$ and $E^{\sigma\sigma'}_{\vec{R}_i,\vec{R}_j}$ is the total energy of a paramagnetic background with the sites $\vec{R}_i$ and $\vec{R}_j$ occupied by Mn, with σ and σ' describing the alignment of averaged magnetic moment in the AS.

This leads to :

$$E^{(2)}(\vec{R}_i - \vec{R}_j) = \int_{-\infty}^{E_F} dE\ (E - E_F)\ \Delta n^{(Mn)}(E) \tag{5.5}$$

where

$$\Delta n^{(Mn)}(E) = -\frac{1}{2\pi}\Im m \sum_{\sigma,\sigma'} \chi_{\sigma\sigma'} \mathrm{Tr}\left[(E\mathbf{I} - \mathbf{H}^{(Mn\ \sigma, Mn\ \sigma')})^{-1}\right]_{av}$$

where, $\mathbf{H}^{Mn\ \sigma, Mn\ \sigma'}$ is the Hamiltonian where every site is occupied randomly by either Cu or paramagnetic Mn, but the sites $\vec{R}_i$ and $\vec{R}_j$ are occupied by Mn atoms with σ and σ' spins respectively. The configuration averaging is carried out using the augmented space recursion introduced by Mookerjee (1973) [10]. Here :

$$\mathrm{Tr}\left[(E\mathbf{I} - \mathbf{H}^{Mn\ \sigma, Mn\ \sigma'})^{-1}\right]_{av} = \sum_i \sum_{\ell,m} \langle \vec{R}_i \ell m \otimes \emptyset | (E\widetilde{\mathbf{I}} - \widetilde{\mathbf{H}}^{Mn\ \sigma, Mn\ \sigma'})^{-1} | \vec{R}_i \ell m \otimes \emptyset \rangle \tag{5.6}$$

the tilded operators are in the product space between $\mathcal{H}$ (in which $\mathbf{H}$ was described) and the space of configurations Φ of the randomly occupying Cu and Mn atoms. $\emptyset$ is the 'reference' configuration described in Mookerjee [10]. The average over random configurations is related to a specific element in the augmented product space. Details can be found in Mookerjee *et.al.*(2003) [33].

The change in the averaged local density of states is related to a generalized phase shift $\eta(E)$ through the relation :

$$\Delta n^{(Mn)}(E) = \frac{d\eta^{Mn}(E)}{dE}$$

where,

$$\eta^{Mn}(E) = \mathrm{Log}\left[\frac{\det \ll \mathbf{G}^{Mn\uparrow,Mn\uparrow}(E) \gg \det \ll \mathbf{G}^{Mn\downarrow,Mn\downarrow}(E) \gg}{\det \ll \mathbf{G}^{Mn\uparrow,Mn\downarrow}(E) \gg \det \ll \mathbf{G}^{Mn\downarrow,Mn\uparrow}(E) \gg}\right]$$

$\mathbf{G}^{Mn\ \sigma,Mn\ \sigma'}$ are the resolvents or Green functions corresponding to $\mathbf{H}^{Mn\ \sigma,Mn\ \sigma'}$. The behaviour of the phase shift is complicated and the integration over the energy by standard methods is difficult. In addition the integrand is multivalued. The way forward was suggested by Burke [11]. Burke's orbital peeling method was a repeated application of the downfolding technique on the Hamiltonian $\widetilde{\mathbf{H}}^{Mn\ \sigma,Mn\ \sigma'}$ and yields a 'pair energy function' :

$$f(\vec{R}_i - \vec{R}_j; E) \;=\; \sum_{\sigma,\sigma'}^{\uparrow\downarrow} \sum_{\ell=1}^{\ell_{max}} \left[\sum_{\lambda=1}^{z^{\ell,\sigma\sigma'}} Z_m^{\ell,\sigma,\sigma'} - \sum_{\lambda=1}^{p^{\ell,\sigma\sigma'}} P_m^{\ell,\sigma,\sigma'} + \left(p^{\ell,\sigma\sigma'} - z^{\ell,\sigma\sigma'}\right) E \right]$$

where $Z^{\ell,\sigma,\sigma'}$ and $P^{\ell,\sigma,\sigma'}$ are the zeroes and poles of the Green functions below E, while $z^{\ell,\sigma,\sigma'}$ and $p^{\ell,\sigma,\sigma'}$, the number of such zeroes and poles. These zeroes and poles are obtained by repeated recursions on the peeled Hamiltonian [12].

Finally,

$$E^{(2)}(\vec{R}_i - \vec{R}_j) = f(\vec{R}_i - \vec{R}_j, E_F) \tag{5.7}$$

The Fig. 5.3 shows the pair energy functions for two characteristic compositions : a low Cu content alloy, $Cu_{20}Mn_{80}$ and a low Mn content alloy, $Cu_{90}Mn_{10}$. We note that although the general shape of the pair energy functions are similar, quantitatively they depend upon the composition. As a result, as shown in Fig. 5.3, the pair energies themselves are composition dependent. In particular, the dominant nearest neighbour pair energy has a distinct dependence on the Mn concentration. For a low Mn concentration alloys with almost the same compositions, we may compare our pair

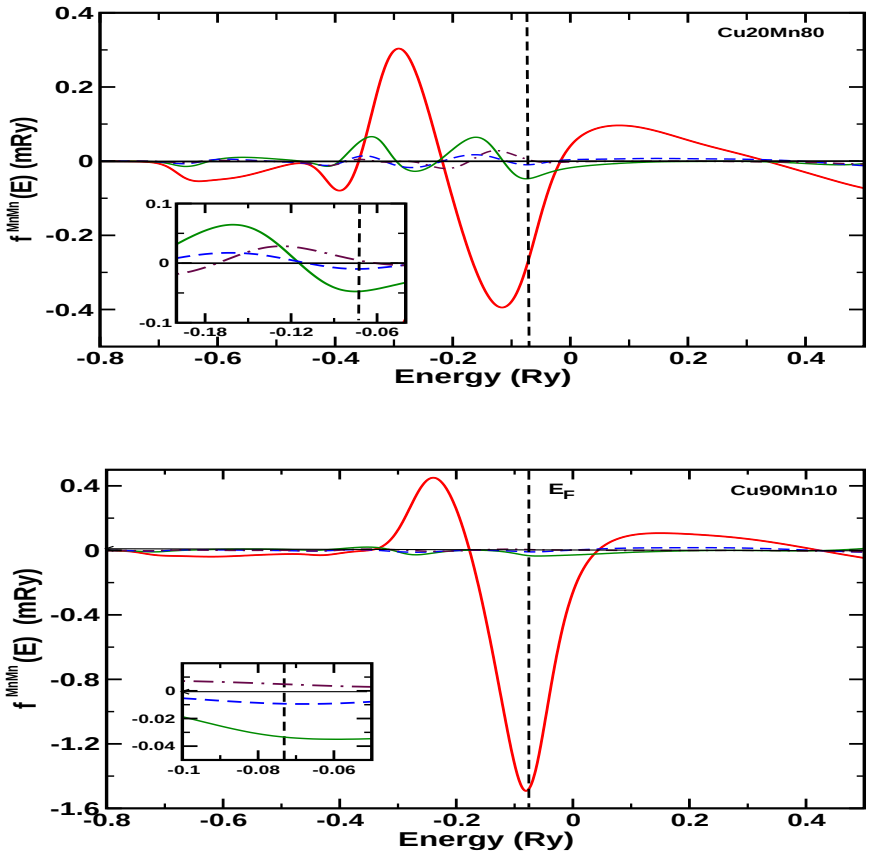

Figure 5.3: The pair energy functions up to fourth nearest neighbours for (top) Cu20Mn80 and (bottom) Cu90Mn10 alloys, obtained from the orbital peeling technique.The inset shows the further neighbour pair energy functions near E_F

energy of -1.5 mRy with -2.5 mRy found by Peil *et.al.*[80]. Our calculation was based on orbital peeling and augmented space recursion on tight-binding linear muffin-tin orbitals method (TB-LMTO-ASR), while theirs was based on the single-site coherent potential approximation on the exact muffin-tin orbitals technique (EMTO-CPA) . Given that the pair energies are really small energy differences, the two match reasonably well. The error in estimates of temperatures will be $\sim 157K$ which is tolerable in a mean-field type approach. The further neighbour pair energies rapidly decrease as is characteristic of disorder damped oscillatory interactions. We have not gone

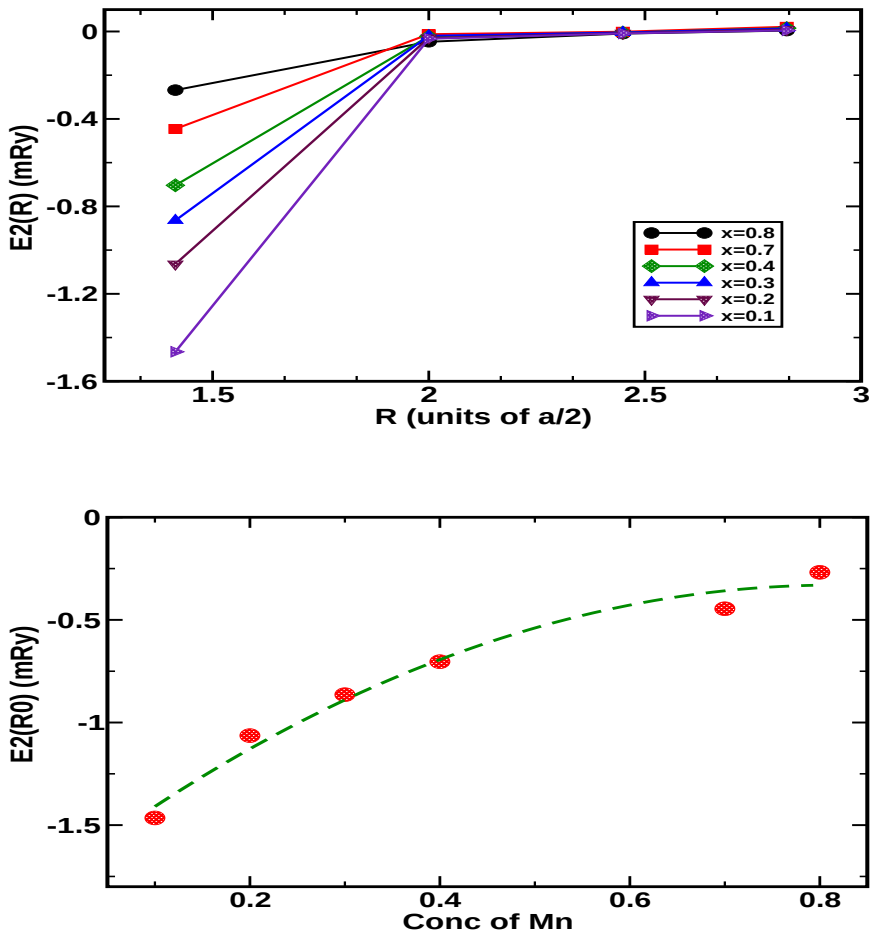

Figure 5.4: (top) E(2)(R_{ij}) as a function of R_{ij} for different compositions of Cu_xMn_{1-x}. (bottom) Composition dependence of the dominant nearest neighbour pair energy.

beyond the fourth nearest neighbours, since the numbers for more distant neighbours become smaller than errors characteristic of the TB-LMTO-ASR and hence it would be meaningless to quote such small numbers.

5.2.3 Mean-field analysis

Our mean-field analysis will begin with the equation :

$$\Delta E \simeq \frac{1}{2} \sum_{\vec{R}_i, \vec{R}_j \in Mn} E^{(2)}(|\vec{R}_i - \vec{R}_j|)\ \delta\xi_i\ \delta\xi_j$$

First of all, we note that in this analysis we do not deal with spin dynamics. Our approach cannot deal with the anomalously slow spin dynamics characteristic of the spin-glass phase. Rather, we shall examine probability distributions of magnetization patterns in the asymptotic time limit.

The free energy can be obtained from the above :

$$F = -\frac{1}{\beta}\ \mathrm{Log}\ \left\{ \mathrm{Tr}_{\{\delta\xi_i\}}\ \exp\left[-\beta \Delta E(\{\delta\xi_i\}\right] \right\}$$

The problem closely resembles a random classical Ising model with fluctuating, long-ranged interactions. This problem has been dealt with earlier by Mookerjee and Roy [81] within a mean-field approximation.

In our case the dominant nearest neighbour $E^{(2)}(R) < 0$ and the transition should be to a pattern where the lattice sites occupied by Mn have a AB ordering. We partition the lattice into two sub-lattices $\mathcal{L}_1$ and $\mathcal{L}_2$ such that the nearest neighbour of a site in $\mathcal{L}_1$ is in $\mathcal{L}_2$ and vice versa. We now define a staggered local occupation variable $\widehat{\xi_i}$ and a staggered pair energy $\widehat{E}^{(2)}(R)$ as :

$$\widehat{\xi_i}\widehat{\xi_j} = I_{ij}\xi_i\xi_j \quad \text{and} \quad \widehat{E}^{(2)}(|\vec{R}_i - \vec{R}_j|) = I_{ij}E^{(2)}(|\vec{R}_i - \vec{R}_j|) \tag{5.8}$$

where $I_{ij} = \pm 1$ according to whether $\vec{R}_i, \vec{R}_j$ are in same or different sub-lattices.

We shall rewrite the energy difference in terms of the staggered quantities :

$$\Delta E = \frac{1}{2} \sum_{\vec{R}_i} \sum_{\vec{R}_j \in Mn} \widehat{E}^{(2)}(|\vec{R}_i - \vec{R}_j|)\ \widehat{\xi_i}\widehat{\xi_j} \tag{5.9}$$

but now the dominant staggered nearest neighbour $\widehat{E}^{(2)} > 0$. We shall closely follow the arguments of Mookerjee and Roy [81] for binary alloys. This approach follows that suggested earlier by Kaneyoshi [82], Plefka [83] and Thouless *et.al.*[84]. The single-site mean-field approximation leads to an estimate of the free energy for a binary alloy :

$$F = \frac{1}{2} \sum_{\vec{R}_i \in Mn} h_i \widehat{n}_i - \frac{1}{\beta} \sum_{\vec{R}_i \in Mn} \log \cosh(\beta h_i)$$

the local staggered occupation parameters are $\widehat{n}_i = \langle \widehat{\xi}_i \rangle$ are the thermal averages of the local staggered occupation numbers. The local staggered 'fields' are given by :

$$h_i = \sum_{\vec{R}_j \in Mn} \widehat{E}^{(2)}(R_{ij}) \; \widehat{n}_j \tag{5.10}$$

where $R_{ij} = |\vec{R}_i - \vec{R}_j|$. On minimizing the Free energy, the thermally stable local staggered occupation parameters are given by :

$$\widehat{n}_i = \tanh(\beta h_i) \tag{5.11}$$

In a disordered alloy the local staggered 'fields' are random. We introduce the configuration averaged order parameters :

$$\begin{aligned} \widehat{n} &= \int dh_i \; \widehat{n}_i(\{h_i\}) \; P(\{h_i\}) \\ q &= \int dh_i \; \widehat{n}_i^2(\{h_i\}) \; P(\{h_i\}) \end{aligned} \tag{5.12}$$

We evaluate the conditional probability density $P(\{\widetilde{h}_i\})$ of the staggered 'field' at $\vec{R}_i$, scaled by the dominant nearest neighbour staggered $\widehat{E}(R_0)$, provided that the site is occupied by Mn by the Radon transform :

$$P(\{\widetilde{h}_i\}) = \sum_{\vec{R}_1} \ldots \sum_{R_M} P(\vec{R}_i, \ldots \vec{R}_M) \prod_{\mu} \delta \left[\widetilde{h}_i - \sum_{Q'} \sum_{\vec{R}_j} \widetilde{E}^{(2)}(R_{ij}) \, \widehat{n}_j \right]$$

where $\widetilde{E}^{(2)}(R_{ij})$ is the scaled pair energy. We assume that there is no clustering or chemical short-ranged correlations, so that any atom can occupy any site with equal probability. Following the same arguments of Mookerjee and Roy [81] for the binary case, we use Eqn.(5.11) and replace the delta functions by their configuration averages to get :

$$P(\{\widetilde{h}_i\}) = \frac{1}{(2\pi)^3} \int dk \exp(ik\widetilde{h}_i) \left[1 - \frac{F_{QQ'}(\{k\})}{M} \right]^N$$

where out of M sites of which N are occupied by Mn atoms.

$$F(\{k\}) = \sum_R \int d\widetilde{h}_j P(\{\widetilde{h}_j\}) \left[1 - \exp\left\{ -ik\widetilde{E}^{(2)}(R) \, \widehat{n}(\beta\widetilde{h}_j) \right\} \right]$$

We shall now expand the exponential and, assuming that the spatial moments $\sum_R [\widetilde{E}^{(2)}(R)]^n$ rapidly decrease with n (which implies that the spatial distribution of the pair energies is approximately Gaussian), we neglect all terms $n \geq 3$. We note that $\lim_{M\to\infty} N/M = x$. We get the conditional probability density of the scaled $\widetilde{h}$ and scale back to get the conditional probability density of the local staggered occupation 'fields' :

$$P(h_i) = (2\pi J_1^2)^{-1/2} \exp\left\{ -(h_i - J_0)^2 / 2J_1^2 \right\} \tag{5.13}$$

where

$$
\begin{aligned}
J_0 &= x\,\widehat{n}\sum_R E^{(2)}(R) \;= k_B T_0\,\widehat{n} \\
J_1^2 &= xq\sum_R \left\{E^{(2)}(R)\right\}^2 \;= k_B^2 T_1^2\; q
\end{aligned}
$$

where $n = \ll n_i \gg$ and $q = \ll (n_i)^2 \gg$ are the two coupled long and short-ranged order parameters respectively, one related to the centers of the distribution of h_i and the other to their widths. They are given by :

$$
\begin{aligned}
\widehat{n} &= \frac{1}{\sqrt{2\pi}}\int dz\; e^{-z^2/2}\tanh\left[\left(\frac{T_0}{T}\;\widehat{n}\right) + \left(\frac{T_1^2}{T^2}q\right)^{1/2} z\right] \\
q &= \frac{1}{\sqrt{2\pi}}\int dz\; e^{-z^2/2}\tanh^2\left[\left(\frac{T_0}{T}\widehat{n}\right) + \left(\frac{T_1^2}{T^2}q\right)^{1/2} z\right]
\end{aligned}
\tag{5.14}
$$

5.3 Result and discussion

As discussed in last section the mean-field approach one can get the phase diagram by the two equations (5.12) and (5.14). In our case when there is only one magnetic constituent with concentration x,

$$
\begin{aligned}
k_B T_N &= x\sum_R E^{(2)}(R,x) \\
k_B T_g &= x\left\{\sum_R E^{(2)}(R,x)^2\right\}^{1/2}
\end{aligned}
$$

How do we distinguish between the paramagnetic, anti-ferromagnetic and 'spin-glass' patterns ? What we study is the probability density of the local field h_i related

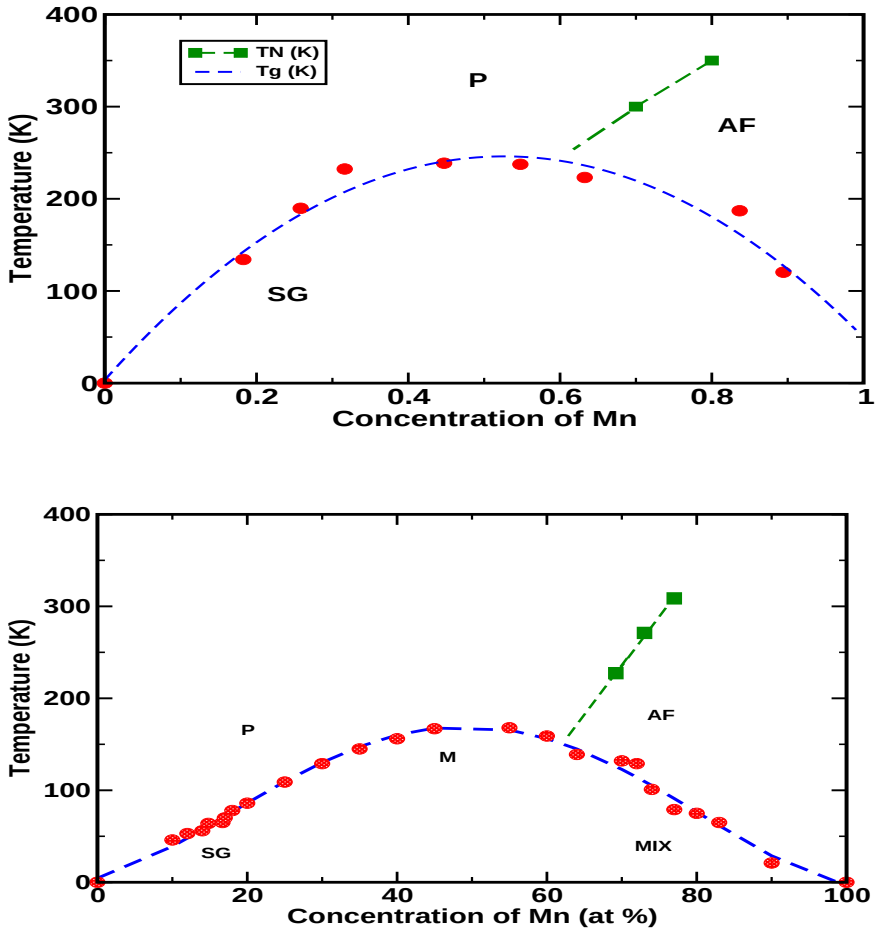

Figure 5.5: (Top) The mean-field phase diagram for CuMn (bottom) Experimental phase diagram after Gibbs *et.al.*[74]

to $\widehat{n}_i$. This is the probability density at $t \to \infty$. Under the approximations stated the probability density is a Gaussian centered at $k_B T_0 \widehat{n}$ and with width $k_B T_1 \sqrt{q}$(i.e. the definition of q). It is not the Edwards-Anderson parameter $q =< \widehat{m}(t)\widehat{m}(0) >$ as $t \to \infty$.

(i) For the paramagnet since h_i is certainly 0, the probability density must be a delta function centered at 0. This happens if $\widehat{n} = q = 0$. This is one of the solutions.

(ii) Another solution is $\widehat{n} = 0$, $q > 0$ and the probability density is a Gaussian with width $k_B T_1 \sqrt{q}$ and centered at 0. This picture is only possible if we have a frozen, random pattern of equi-concentration of A (Mn↑) and B (Mn ↓) atomic spheres. This picture is that of a disordered frozen moment phase with overall zero moment which persists at long times. It is not an unreasonable picture of a spin glass.

(iii) The third solution is $\widehat{n} > 0$ $q > 0$ and the probability density is a Gaussian centered at $k_B T_0 \widehat{n} > 0$ with width $k_B T_1 \sqrt{q} > 0$. This picture is possible if we have a macroscopic cluster of A (Mn ↑) or B (Mn ↓) atomic spheres occupying interpenetrating sub-lattices interspersed with a few B (or A) spheres randomly in the wrong positions, to give the probability density a spread. This is the picture of a random anti-ferromagnetic phase.

(iv) The mixed or randomly canted phase is not one of the solutions. We expect this, because the model of itinerant electrons on which our description was based allowed for only collinear magnetism. In order to study the mixed or randomly canted phase we have to begin with a formulation that allows for non-collinear magnetism. Such a formulation of the LSDA exists [85]-[86] and we shall report this generalization in a future communication.

Mookerjee and Roy [81] have studied the $T = 0$ phases and have shown that there exists a critical concentration x_c beyond which there is a transition from paramagnetic to an antiferromagnetic to a re-entrant spin-glass phase. If we assume the the pair energies $E^{(2)}(R_{ij})$ are independent of composition, which is approximately the case with ferromagnetic Fe in AuFe alloys, then the para-ferro boundary behaves as $\sim x$ and the para-spin-glass boundary as $\sqrt{x}$. However, for CuMn, as we have seen earlier,

the pair energies and hence J_0 and J_1 has additional composition dependence. Fig. 5.5 (upper panel) shows the mean-field magnetic phase diagram for CuMn while the lower panel shows the experimental results taken from Gibbs *et.al.*[74]. Mean-field approaches always overestimates the transition temperatures. With that in mind, the theoretical prediction matches rather well with experimental data. At low Mn content we have transition between paramagnetic to the spin-glass phases, while for high Mn content alloys ($> 70at\%$) we have transition from paramagnetic to collinear antiferromagnetic to the mixed phase at lower temperatures.

5.4 Concluding Remarks

For CuMn the mean-field picture is not complete. There is enough evidence of both atomic and magnetic short-ranged order developing in the alloy. Peil *et.al.*[80, 87] have carried out a detailed study of one specific composition $Cu_{83}Mn_{17}$. They have analyzed the effect of simultaneous atomic and magnetic ordering and have concluded that their work agreed well with recent neutron scattering experiments [88]-[73]. The simple mean-field picture of a homogeneous spin-glass phase has to be modified in the presence of such short-ranged ordering. A similar thorough first-principles study is called for in the entire composition range.

Chapter 6

Conclusion

In this chapter, we conclude the work carried out in this thesis and summarize what we have achieved.

Our aim was to study phonon using first-principle. We systematically formulated a theoretical scheme to study lattice vibrational properties of disordered binary alloy, which is discussed in chapter 2-4. A short work we did on Cu-Mn alloy to study magnetic phase in chapter 5 also. The techniques we used while formulating the methodology to study different phononic properties are *augmented space recursion, special quasi-random structure, feynman diagram method, small displacement method, density functional perturbation theory, and orbital peeling.* In the following, we briefly describe the steps followed along with the achievement:

- In chapter 1, we briefly introduce the disorder handling techniques and how they can be used to study lattice dynamics of configurational disordered system. We mentioned two methodology namely augmented space recursion and quasi-random structure and described why these methods are more feeble to study disorder systems.

- In chapter 2, we investigated the lattice dynamics and the vibrational and con-

figuration entropy of disordered alloy using ASR. We formulated short-range order (SRO) effect on the lattice dynamics. We studied these properties on bcc $Fe_{1-x}Cr_x$ (x=0.75,0.45,0.25) and $Fe_{1-x}Cr_x$ (x=0.29,0.43,0.75) alloy. For $Fe-Cr$ alloy we reported that the effect of SRO did not come out to be significant in terms of the magnitude of phonon entropy of mixing, which we initially thought not to be the case. In *Re-W* alloy we found that for *Re*-rich alloy phonon dispersion to be strongly fuzzy; an outcome of higly asymmetric coherent structure factor with large disorder induced broadening.

- In chapter 3 we used Kubo-Greenwood formula with density functional perturbation theory (Quantum Espresso) based first principle calculation to study the thermal conductivity and diffusivity for binary bcc $Fe_{1-x}Cr_x$ alloy. At low T-regime, thermal conductivity (κ) shows a quadratic T-dependence, While it increase smoothly to T-independent saturated value at high T. We found that both $\kappa(\mu)$ and $J(\mu)$ have dip at very small energy ($\mu \approx 0$) similar to Feldman *et.al.*[48]. We reported dc-thermal conductivity for $x = 47\%$ to be 24.7 W/mK, which is comparable to $\kappa_{expt}(x = 0.25) \approx 22.0 W/mK$.

- In this chapter we proposed a systematic way of calculating the inter-atomic force constants for disordered alloy using first principles method. To get the averaged force constant in random environment at different bond lengths we incorporate special quasi-random structure along with small displacement method, and did symmetry transformation around the nearest neighbor. For two different symmetry bcc (TaW) and fcc (NiPt) we successfully shown the phononic behaviour and verified it with experimental data. In bcc TaW alloy, Ta-Ta force constant are predicted to be stiffer compared to the pure Ta, however

W-W force constants behave oppositely. In case of fcc NiPt, Ni-Ni (Pt-Pt) force constants within the disordered environment behave softer (stiffer) than compared to pure Ni (Pt). We also conclude that the average distribution of bond length between A-A, B-B and A-B in disordered alloy is also related to the nature of the behavior of inter-atomic force constants. We found that large SQS cells results are more accurate and promising. Phonon dispersion using 32-atom SQS cell force constants for bcc $Ta_{50}W_{50}$ agree well with the experiment.

- In chapter 5 we performed electronic structure calculation to study magnetic phase of disorder *Cu-Mn* alloys using orbital peeling technique and ASR. We found a transition between pramagnetic to spin glass transition for *Cu-Mn* alloy at low *Mn* concentration while a transition from paramagnetic to collinear anti-ferromagnetic leading to the mixed phases for high *Mn* ($> 70\%$) concentration at low temperature. Our result agrees well with experimental phase diagram shown by Gibbs *et.al.*[74].

6.1 Future scope

During the investigation of phononic properties using augmented space recursion we concluded that the key factor is dynamical matrix. The implement of dynamical matrix using SQS gives more accuracy in the result and matches well with the experimental neutron scattering results, have shown in chapter 4. Our future aspect will be to perform SQS based calculation for few more systems to check the performance of our new formulated methodology. We will also in-cooperate SRO again in this to see the variation to our old calculation. We will also extend our idea to ternary disordered alloys.

Appendices

Appendix A

List of SQS atomic positions

Table A.1: BCC Spectral Quasi-random Structure (SQS) for concentration $A_{50}B_{50}$ see ref. [57]

No. of atoms	Lattice vectors	Unrelaxed atomic positions
32-atom	L1 = 1.0 -2.0 0.0 L2 = 0.0 -4.0 2.0 L3 = -2.0 0.0 -2.0	A-atom 0.0 -4.0 0.0 0.0 -2.0 0.0 -0.5 -0.5 -0.5 -1.0 -4.0 -1.0 -0.5 -1.5 -0.5 0.0 -1.0 0.0 -1.0 -3.0 -1.0 0.5 -4.5 1.5 0.5 -5.5 1.5 -1.5 -2.5 -0.5 -1.5 -3.5 -0.5 -0.5 -2.5 0.5 -1.0 -6.0 0.0 -0.5 -3.5 0.5 0.0 -3.0 1.0 -1.0 -5.0 0.0 B-atom -0.5 -4.5 0.5 -0.5 -5.5 0.5 0.0 -5.0 1.0 0.5 -2.5 0.5 0.5 -3.5 0.5 -1.5 -0.5 -1.5 -1.5 -1.5 -1.5 -1.0 -1.0 -1.0 -1.0 -2.0 -1.0 -0.5 -2.5 -0.5 -0.5 -3.5 -0.5 0.0 -3.0 0.0 0.0 -6.0 1.0 0.0 -4.0 1.0 -1.0 -3.0 0.0 -1.0 -4.0 0.0

No. of atoms	Lattice vectors	Unrelaxed atomic positions
16-atom	L1 = -0.5 -1.5 -2.5 L2 = -0.5 2.5 1.5 L3 = 1.5 0.5 -0.5	A-atom 0.0 0.0 -2.0 0.5 1.5 -0.5 1.0 0.0 -2.0 0.5 0.5 -0.5 0.5 -0.5 -2.5 -0.5 1.5 -0.5 0.0 2.0 0.0 0.5 2.5 0.5 B-atom 1.0 2.0 0.0 -0.5 0.5 -1.5 1.0 1.0 -1.0 0.0 1.0 0.0 0.5 1.5 -1.5 0.0 1.0 -1.0 0.0 0.0 -1.0 0.5 0.5 -1.5
8-atom	L1 = 0.5 0.5 -1.5 L2 = 1.5 0.5 -0.5 L3 = 0.0 -2.0 0.0	A-atom 2.0 0.0 -2.0 0.5 -1.5 -0.5 1.0 -1.0 -1.0 1.5 -0.5 -1.5 B-atom 2.0 -1.0 -2.0 0.5 -0.5 -0.5 1.0 0.0 -1.0 1.5 0.5 -1.5

Table A.2: FCC Spectral Quasi-random Structure (SQS) for concentration $A_{50}B_{50}$ see ref. [57]

No. of atoms	Lattice vectors	Unrelaxed atomic positions
32-atom	L1 = 2.00 0.00 0.00 L2 = 0.00 2.00 0.00 L3 = 0.00 0.00 2.00	A-atom 1.00 1.00 0.50 1.00 0.25 0.75 0.25 1.00 0.75 1.00 0.25 0.25 1.00 0.50 0.50 1.00 0.75 0.75 0.25 1.00 0.25 0.25 0.25 0.50 0.75 1.00 0.75 1.00 0.50 1.00 0.25 0.50 0.25 0.50 0.25 0.25 0.75 0.25 0.50 0.50 0.50 1.00 0.75 0.25 1.00 0.75 0.75 1.00 B-atom 1.00 1.00 1.00 0.25 0.50 0.75 0.50 1.00 0.50 0.50 0.25 0.75 1.00 0.75 0.25 0.25 0.25 1.00 0.25 0.75 0.50 0.50 1.00 1.00 0.50 0.50 0.50 0.50 0.75 0.75 0.75 1.00 0.25 0.75 0.50 0.75 0.25 0.75 1.00 0.50 0.75 0.25 0.75 0.50 0.25 0.75 0.75 0.50

No. of atoms	Lattice vectors	Unrelaxed atomic positions
16-atom	L1 = 1.0 -0.5 -0.5 L2 = 0.0 1.0 -1.0 L3 = 1.0 1.5 1.5	A-atom 0.250 0.250 0.250 0.250 0.750 0.250 0.750 0.500 0.250 0.250 0.000 0.750 0.000 0.250 0.500 0.500 0.750 0.000 0.000 0.500 0.000 0.000 0.000 0.000 B-atom 0.500 0.500 0.500 0.750 0.000 0.250 0.500 0.000 0.500 0.250 0.500 0.750 0.000 0.750 0.500 0.750 0.250 0.750 0.750 0.750 0.750 0.500 0.250 0.000
8-atom	L1 = 1.00 0.50 -0.50 L2 = 0.50 0.50 -1.00 L3 = -1.00 2.00 1.00	A-atom 0.00 0.00 0.500 0.50 0.50 0.250 0.75 0.75 0.625 0.75 0.75 0.125 B-atom 0.00 0.00 0.000 0.25 0.25 0.875 0.25 0.25 0.375 0.50 0.50 0.750

Bibliography

[1] H. Ehrenreich and L. Schwartz, *Solid State Physics*, F. Seitz and D. Turnbull, Ed.(Acedemic, New York) **31**, 149 (1976).

[2] J. S. Faulkner,*Progress in Materials Science* **27**, 1 (1982).

[3] R. Prasad, in *Methods of Electronic Structure Calculations*,O.K. Andersen, V. Kumar, and A. Mookerjee, Eds (World-Scientific, Singapore) 211 (1995).

[4] P. Soven, *Phys. Rev.***156** 809 (1967).

[5] J. K. Flicker and P. L. Leath, *Phys. Rev.* B **7**, 2296 (1973); W. H. Butler, *Phys. Rev.* B **31**, 3260 (1985).

[6] A. Gonis and J.W. Garland, *Phys. Rev.* **B 18**, 3999 (1978); T. Kaplan, P.L. Leath, L.J. Gray and H.W. Diehl, *Phys. Rev.* **B 21**, 4230 (1980).

[7] D. A. Rowlands, J. B. Staunton, B. L. Gyorffy, E. Bruno and B. Ginatempo, *Phys. Rev.***B 72**, 045101 (2005).

[8] D. A. Biava, S. Ghosh, D. D. Johnson, W. A. Shelton, and A. V. Smirnov, *Phys. Rev.* **B 72**, 113105 (2005).

[9] A. Zunger, S. -H. Wei, L. G. Ferreira and J. Bernard, *Phys. Rev. Lett***65**, 353 (1990).

[10] Abhijit Mookerjee, *J. Phys. C : Solid State Phys.***6**, L205 (1973).

[11] N. R. Burke, Surf. Sc. **58**, 3419 (1976).

[12] R. Haydock, V. Heine, and M.J. Kelly, *J. Phys. C : Solid State Phys.***5**, 2845 (1972).

[13] Aftab Alam and Abhijit Mookerjee *Phys. Rev.* **B 69**, 024205 (2004).

[14] N. Beer and D. Pettifor in *The Electronic Structure of Complex Systems* (Plenum Press, New York) (1984).

[15] S. M. Dubiel, J. Cieslak, W. Sturhahn, M. Sternik, P. Piekarz, S. Stankov, and K. Parlinski, *Phys. Rev. Lett* **104**, 155503 (2010); W. Sturhahn *et al.*, *Phys. Rev. Lett* **74**, 3832 (1995).

[16] M. S. Lucas, M. Kresch, R. Stevens and B. Fultz, *Phys. Rev.* **B 77**, 184303 (2008).

[17] T. L. Swan-wood, O. Delaire, and B. Fultz, *Phys. Rev.* **B 72**, 024305 (2005).

[18] R. J. Elliot, J. A. Krumhansl, and P. L. Leath, Rev. Mod. Phys. **46**, 465 (1974).

[19] J. K. Okamoto *et al.*, Microbeam analysis-1990, edited by J. R. Michael and P. Ingram (San Francisco Press, San Francisco 1990). p. 56.

[20] L. Anthony *et al.*, *Phys. Rev. Lett* **70**, 1128 (1993); G. D. Garbulsky and G. Ceder, *Phys. Rev.* **B 49**, 6327 (1994), **B 53**, 8993 (1996).

[21] J. L. Nagel, B. Fultz and J. L. Robertson, Phil. Mag. **B 75**, 681 (1997).

[22] B. Fultz, L. Anthony, J. L. Robertson, R. M. Nicklow, S. Spooner and M. Mostoller, *Phys. Rev.* **B 52**, 3280 (1995).

[23] B. Fultz, T.A. Stephens, W. Sturhahn, T.S. Toellner and E.E. Alp, *Phys. Rev. Lett* **80**, 3304 (1998).

[24] Masaki Goda, *J. Phys. C : Solid State Phys.***6**, 3047 (1973); J. Phys. F: Metal Phys. **7**, 1421 (1977).

[25] G. Bonny, P. Erhart, A. Caro, R.C. Pasianot, L. Malerba and M. Caro, Model Simul. Mater. Sci. Eng. **17**, 025006 (2009).

[26] Paul Erhart, Alfredo Caro, Magdalena Serrano de Caro and Babak Sadigh, *Phys. Rev.* **B 77**, 134206 (2008).

[27] M. K. Miller, *Surf. Sci.* **246**, 434 (1991); A Cerezo, J. M. Hyde, M.K. Miller, S.C. Petts, R.P. Setna and G. D. W. Smith, Philos. Trans. R. Soc. London A Ser. **341**, 313 (1992).

[28] A. van de Walle and G. Ceder, *Phys. Rev.* **B 61**, 5972 (2000).

[29] G. J. Ackland, *Alloy Modelling and Designs*, edited by G. Stocks and P. Turchi (The minerals, Metals and Materials Society, Pittsburgh, PA), p. 149 (1994).

[30] R. Herschitz and D. N. Seidman, *Acta Metall.* **32**, 1141 (1984).

[31] K. Persson, M. Ekman and G. Grimvall, *Phys. Rev.***B 60**, 9999 (1999).

[32] R. Holzi, F. A. Glaski and J. R. Humphrey, United States patent **75**, 174 (1968), **3**, 3219 (1990).

[33] A. Mookerjee, *Electronic structure of Alloys, Surfaces and Clusters* ed. D. D. Sarma and A. Mookerjee (London: Taylor and Francis) (2003).

[34] Afab Alam and Abhijit Mookerjee, *J. Phys.: Condens. Matter***21**, 195503 (2009); T.Saha, I. Dasgupta, and A. Mookerjee, *Phys. Rev.* **B 50**, 13267 (1994).

[35] Quantum-Espresso is a community project for high-quality quantum-simulation software, based on density functional theory, and Coordinated by P. Gianozzi. See *http://www.Quantum-Espresso.org* and *http://www.pwscf.org* ; P. Giannozzi *et al.*, *J. Phys.: Condens. Matter***21**, 395502 (2009).

[36] S. Baroni, S. De Gironcoli, A. Dal Corso, and P. Giannozzi, Rev. Mod. Phys. **73**, 515 (2001).

[37] D. Vanderbilt, *Phys. Rev.* **B 41**, 7892 (1990); S. G. Louie, S. Froyen and M. L. Cohen, *Phys. Rev.* **B 26**, 1738 (1982).

[38] M. Methfessel and A. T. Paxton, *Phys. Rev.* **B 40**, 3616 (1989).

[39] Parthapratim Biswas, Biplab Sanyal, M. Fakhruddin, Amal Halder, Abhijit Mookerjee, and Mesbahuddin Ahmed *J. Phys.: Condens. Matter***7**, 8569 (1995).

[40] K. K. Saha, T. Saha-Dasgupta, A. Mookerjee, and I. Dasgupta, *J. Phys.: Condens. Matter***16**, 1409 (2004).

[41] J. O. Andersson and B. Sundman, CALPHAD: Comput. Coupling Phase Diagrams Thermochem. **11**, 83 (1987).

[42] M. S. Lucas, A. Papandrew, B. Fultz, and M. Y. Hu, *Phys. Rev.* **B 75**, 054307 (2007).

[43] S. H. Chen and B. N. Brockhouse, Solid State Commun. **2**, 73-77 (1964).

[44] J. P. Perdew and Alex Zunger, *Phys. Rev.***B 23**, 5048 (1981).

[45] A. Alam, Rajiv Kumar Chouhan and A. Mookerjee, *Phys. Rev.* **B 83**, 054201 (2011).

[46] Aftab Alam, Subhradip Ghosh and Abhijit Mookerjee, *Phys. Rev.* **B 75**, 134202 (2007).

[47] Tao Sun and P. B. Allen, *Phys. Rev.* B **82**, 224305 (2010).

[48] Philip. B. Allen and Joseph. L. Feldman, *Phys. Rev.* B **48**, 12581 (1993); Joseph L. Feldman *et.al.*, *Phys. Rev.* B **48**, 12589 (1993).

[49] Y. Tsunoda, N. Kunitomi, N. Wakabayashi, R. M. Nicklow, and H. G. Smith *Phys. Rev.* B **19**, 2876 (1979).

[50] Aftab Alam and Abhijit Mookerjee, *Phys. Rev.* B **72**, 214207 (2005).

[51] P. A. Lee and T. V. Ramakrishnan, Rev. Mod. Phys. **57**, 287 (1985).

[52] R. Biswas, A. M. Bouchand, W. A. Kamikitahara, G. S. Grest, and C. M. Soukoulis,*Phys. Rev. Lett* **60**, 2280 (1988).

[53] G. Renaud *et al.*, *Phys. Rev.***B 38**, 5944 (1988).

[54] S. Ghosh *et al.*, *Phys. Rev.***B 66**, 214206 (2002).

[55] A. van de Walle *et al.*, Rev. Mod. Phys. **74**, 11 (2002).

[56] C. K. Gan *et al.*, *Phys. Rev.***B 73**, 235214 (2006); A. van de Walle and G. Ceder, *Phys. Rev.***B 61**, 5972 (2000).

[57] Chao Jiang *et al.*, *Phys. Rev.***B 69**, 214202 (2004); A. van de Walle and G. Ceder, *Phys. Rev.***B 61**, 5972 (2000); J. von Pezold *et al.*, *Phys. Rev.***B 81**, 094203 (2010); Yao-Ping Xie *et al.*, Comput. Mater. Sci. **50**, 2586 (2011); For other fcc SQS structure, See URL : *http://www.mpie.de/index.php?id=fcc*

[58] G. Kresse and J. Furthmüller, *Phys. Rev.* **B 54**, 11169 (1996); Comput. Mat. Sci. **B 6**, 15 (1996).

[59] G. Kresse and D. Joubert, *Phys. Rev.* **B 59**, 1758 (1999).

[60] D. Alfè, Comp. Phys. Commun. **180**, 2622 (2009).

[61] C. Leroux,M.C. Cadeville, V. Pierron-Bohnes, G. Inden, F. Hinz, Journal of Physics F **18**, 2033-2051 (1988).

[62] Z.I. Tolmacheva, V.I. Kornilova, Izvestiya Akademii Nauk SSSR, Metally **3** 211-214 (1972).

[63] See Supplemental Material at [URL] for details of the transformation matrices for fcc and bcc lattice.

[64] A. D. B. Woods, *Phys. Rev.* **B 136**, A781 (1964).

[65] A. Larose and B. N. Brockhouse, Solid State Commun. **2**, 73 (1964).

[66] B. J. Higuera *et* al., *Phys. Rev.***B 31**, 730 (1985).

[67] Oscar Granas *et* al., *J. Phys.: Condens. Matter***24**, 015402 (2012).

[68] D. H. Dutton *et* al., Can. J. Phys.**50**, 2915 (1972).

[69] R. W. Schmitt and I.S.Jacobs, Can. J. Phys **34** 1285 (1957).

[70] D. Meneghetti and S.S. Sidhu, *Phys. Rev.***105** 130 (1957).

[71] P. Wells and J.H.Smith, *J. Phys. F: Met. Phys.* **1** 763 (1971).

[72] J. R. Davies, S.K. Burke and B.D. Rainford, J. Magn. Magn. Mater. **15-18** 151 (1980).

[73] B. Schönfeld, R. Bucher, G. Kostorz and M. Zolliker, *Phys. Rev.***B69** 224205 (2004).

[74] P. Gibbs, T.M. Harders and J.H. Smith, *J. Phys. F: Met. Phys.* **15** 213 (1985).

[75] Y. Tsunoda and Y. Nakai, J. Phys. Soc. (Japan) **31** 436 (1981).

[76] D. Chowdhury, T.M. Harders, A. Mookerjee and P. Gibbs, Solid State Commun. **57** 603 (1986).

[77] O. Jepsen, O.K. Andersen, and A.R. Mackintosh,*Phys. Rev.***B 12**, 3084 (1975).

[78] F. Ducastelle and F. Gautier, *J. Phys. F: Met. Phys.* **6** 2039 (1976).

[79] T. L. Einstein and J.R. Schrieffer, *Phys. Rev.***B 7**, 3629 (1973).

[80] O. E. Peil, A.V. Ruban and B.Johansson, New J Phys **10** 83026 (2008).

[81] A. Mookerjee and S. B. Roy, Pramana, **21** 171 (1983).

[82] T. Kaneyoshi, *J. Phys. C : Solid State Phys.***9** L 289 (1976).

[83] T. Plefka, *J. Phys. F: Met. Phys.* **6** L 327 (1976).

[84] D. J. Thouless, P. W. Anderson and R. Palmer, Phil. Mag. **35** 593 (1977)

[85] J. Kübler, K. -H. Höck, J. Sticht and A.R. Williams, *J. Phys. F: Met. Phys.* **18** 469 (1988).

[86] A. Sakuma, *J. Phys. Soc. (Japan)* **69** 3072 (2000).

[87] O. E. Peil, A.V. Ruban and B. Johansson, *Phys. Rev.***B79** 024428 (2009).

[88] J. W. Cable, S.A. Werner, G.P. Felcher and N. Wakabayashi, *Phys. Rev. Lett***49** 829 (1982).

[89] Y. Tsunoda, N Kunitomi and J.W. Cable, Appl. Phys. **57** 3753 (1985).

[90] P.G. Klemens, *Landolt-Börnstein Database: Thermal Conductivity of Metals and Alloys*, edited by O. Madelung and G.K. White, Vol. 15c (Springer-Verlag, Berlin 1991).

[91] B. Nickel and W.H. Butler, *Phys. Rev. Lett***30**, 363 (1973).

[92] C. Berne, A. Pasturel, M. Sluiter and B. Vinet, *Phys. Rev. Lett***83**, 1621 (1999).

[93] D. W. Taylor, *Phys. Rev.* **156**, 1017 (1967).

[94] F. Ducastelle, *J. Phys. C* **7**, 1795 (1974).

[95] G.M. Stocks, W.M. Temmerman and B.L. Gyorffy, *Phys. Rev. Lett***41** 339 (1978).

[96] H. G. Smith and N. Wakabayashi, *Bull. Am. Soc.* **21**, 410 (1976).

[97] H. Shiba, *Prog. Theor. Phys.* **40**, 942 (1968).

[98] I. A. Abrikosov, S.I. Simak, B, Johansson, A.V. Ruban and H.L. Skriver, *Phys. Rev.***B76** 014434 (1997)

[99] J. R. Davies and T.J. Hicks, *J. Phys. F: Met. Phys.* **7** 2153 (1977)

[100] J. Sticht, K. -H. Höck and J. Kübler, *J. Phys.: Condens. Matter***1** 8155 (1989)

[101] K. W. Katahara, M.H. Manghnani and N. Devnani, *J. Appl. Phys.* **52**, 3360 (1981).

[102] M. Banerjee, A.Mookerjee, A.K. Majumdar, R. Banerjee, B. Sanyal and A.K. Nigam, *J. Magn. Magn. Mater.***322** 3558 (2010)

[103] M. Jarrell and H. R. Krishnamurthy, *Phys. Rev.***B 63**, 125102 (2001).

[104] M. Mostoller, T. Kaplan, N. Wakabayashi and R. M. Nicklow, *Phys. Rev.***B 10**, 3144 (1974).

[105] N. Ahmed and T.J. Hicks, *J. Phys. F: Met. Phys.* **5** 2168 (1975)

[106] M. Uhl, L.M. Sandratskii and J. Kübler, *Phys. Rev.***B 50** 291 (1994)

[107] N. Kunimoto, Y. Tsunoda and Y. Hirai, *Solid State Commun.* **13**, 495 (1973).

[108] O. Moze and T.J. Hicks, *J. Phys. F: Met. Phys.* **11** 1471 (1981); **12** 1 (1982)

[109] P. Gibbs, O. Moze and T.J. Hicks, *J. Phys. F: Met. Phys.* bf 11 L83 (1981)

[110] R. A. Ayres, G. W. Shanette and D.F. Stein, *J. Appl. Phys.* **46**, 1526 (1975).

[111] R. Haydock in "Solid state physics" vol 35 (Academic Press, New York) (1980).

[112] R. Lorenz and J. Hafner, *J. Magn. Magn. Matter.* **139** 139 (1995)

[113] S. Ghosh, P.L. Leath and M.H. Cohen, *Phys. Rev.* **B 66**, 214206 (2002).

[114] S. J. Campbell, T.J. Hicks and P. Wells, *J. Magn. Magn. Mater.***31-34** 625 (1983)

[115] S. Tournier, B. Vinet, A. Pasturel, I. Ansara and P. J. Desré, *Phys. Rev.***B 57**, 3340 (1998).

[116] T. C. Shulthess, W.H. Butler, G.M. Stocks, S. Maat and G.J. Mankey, *J. Appl. Phys.* **15** 4842 (1999)

[117] T. Kaplan and M. Mostoller, *Phys. Rev.***B 9**, 353 (1974).

[118] T. Kaplan, P. L. Leath, L. J. Gray and H. W. Diehl, *Phys. Rev.***B 21**, 4230 (1980).

[119] T. M. Harders,T.J. Hicksand J.H.Smith, J. Magn. Magn.Mater. **14** 244 (1979)

[120] T.M. Harders,T.J. Hicks and J.H.Smith, *J. Phys. F: Met. Phys.* **13** 1263 (1983)

[121] T.M. Harders and P. Wells, *J. Phys. F: Met. Phys.* **13** 1017 (1983)

[122] T. Saha, I. Dasgupta and A. Mookerjee, *Phys. Rev.***B 50**, 13267 (1994).

[123] W. A. Kamitakahara, *Bull. Am. Phys. Soc.* **19**, 321 (1974).

[124] W. A. Kamitakahara and D. W. Taylor, *Phys. Rev.***B 10**, 1190 (1974).

[125] Y. Kakehashi, S. Akbar and N. Kimura, *Phys. Rev.***B 57** 8354 (1998)

[126] Y. Tsunoda, N Kunitomi and J.W. Cable, Appl. Phys. **57** 3753 (1985).

[127] Y. Wang, G.M. Stocks, W.A. Shelton,D.M.C. Nicholson, Z. Szotek and W.M. Temmerman, *Phys. Rev. Lett.***75** 2867 (1995)